



HAL
open science

Simulation of three-dimensional skyrmions in confined geometries

Swapneel Amit Pathak

► **To cite this version:**

Swapneel Amit Pathak. Simulation of three-dimensional skyrmions in confined geometries. Physics [physics]. Université de Strasbourg, 2021. English. NNT : 2021STRAE012 . tel-03976502

HAL Id: tel-03976502

<https://theses.hal.science/tel-03976502>

Submitted on 7 Feb 2023

HAL is a multi-disciplinary open access archive for the deposit and dissemination of scientific research documents, whether they are published or not. The documents may come from teaching and research institutions in France or abroad, or from public or private research centers.

L'archive ouverte pluridisciplinaire **HAL**, est destinée au dépôt et à la diffusion de documents scientifiques de niveau recherche, publiés ou non, émanant des établissements d'enseignement et de recherche français ou étrangers, des laboratoires publics ou privés.

ÉCOLE DOCTORALE ED 182- Physique et chimie physique

UMR7504- Institut de Physique et Chimie des Matériaux de Strasbourg (IPCMS)

Départements Magnétisme des Objets NanoStructurés (DMONS)

THÈSE

présentée par :

Swapneel Amit PATHAK

23 mars 2021

pour obtenir le grade de : **Docteur de l'université de Strasbourg**

Discipline/ Spécialité : Physique

Simulation of Three-Dimensional Skyrmions in Confined Geometries

THÈSE dirigée par :

Dr. HERTEL Riccardo

Directeur de recherche, IPCMS - CNRS - UMR7504
Université de Strasbourg

RAPPORTEURS :

Dr. KIM Joo-Von

Chargé de recherche, C2N - CNRS - UMR 9001
Université Paris-Saclay

Prof. BUDA-PREJBEANU Liliana

Professeur, SPINTEC Université Grenoble Alpes/CNRS/CEA

AUTRES MEMBRES DU JURY :

Prof. HERVIEUX Paul-Antoine

Professeur, IPCMS - CNRS - UMR7504
Université de Strasbourg

Abstract

Les skyrmions magnétiques sont des configurations tourbillonnantes de l'aimantation, avec une taille nanométrique et une topologie non-triviale. Ces structures ont été observées pour la première fois expérimentalement en 2009 [1]. Les skyrmions sont généralement stabilisés dans les matériaux possédant une interaction Dzyaloshinskii-Moriya (DMI) en raison d'une rupture de symétrie d'inversion spatiale. Cette rupture de symétrie peut soit intervenir à la surface soit être intrinsèque au matériau. Les skyrmions peuvent être considérés comme une solution du type soliton d'un champ vectoriel continu de l'aimantation dans l'approximation micromagnétique (théorie du continu). Par conséquent, ils ont tendance à se comporter comme des quasi-particules rigides. En raison de leur topologie non-triviale, ils ne peuvent pas être transformés de manière continue dans un état homogène. Ceci leur confère une stabilité accrue et une grande résistance aux défauts du matériau. En outre, des propriétés telles que les faibles densités de courant nécessaires pour leur dépiégeage [2], leur taille réduite [3] et leur persistance à température ambiante [4–6] ont donné un élan substantiel à l'étude des skyrmions magnétiques tant du point de vue fondamental que du point de vue de l'application.

La possibilité d'utiliser des skyrmions pour réduire davantage les dimensions dans la technologie CMOS contemporaine, conformément à la loi de Moore, a engendré le domaine de l'électronique des skyrmions ou la skyrmionique. Comme son nom l'indique, ce domaine vise à intégrer des skyrmions dans des microprocesseurs contemporains, des mémoires à accès aléatoire et dans des applications d'hyperfréquence (RF). Les skyrmions ont aussi trouvé une application sous la forme d'unités de stockage d'informations dans une nouvelle version de mémoire à base de registre de décalage du type « race-track » [7], des dispositifs de nano-oscillateurs de spin-torque (STNO) pour des applications hyperfréquences [8, 9], et des dispositifs de type transistor et porte logique [10–12]. Ils sont également prometteurs dans le calcul non conventionnel, comme les dispositifs neuromorphiques, le calcul de réservoir et le calcul stochastique [13]. Il existe encore des défis importants liés à la compréhension des propriétés des matériaux skyrmioniques et les caractéristiques intrinsèques d'un skyrmion pour une

intégration complète dans de nouveaux dispositifs. Cependant, les résultats obtenus à partir de différentes études théoriques et expérimentales sur les skyrmions sont assez encourageants.

La plupart des géométries de matériaux considérées jusqu'à récemment en nanomagnétisme et en spintronique étaient bidimensionnelles (2D), en raison de la facilité de fabrication et de caractérisation dans ce type de géométries. Grâce au progrès atteint dans les techniques d'élaboration et de simulation [14] au cours de la dernière décennie, la possibilité d'obtenir des configurations tridimensionnelle (3D) complexes de l'aimantation [15] dans les nanostructures ferromagnétiques dans des géométries 3D a suscité l'intérêt de la communauté du nanomagnétisme. Dans le cas des skyrmions magnétiques, suivant une tendance générale du nanomagnétisme, la majorité des études scientifiques, ainsi que des applications de dispositifs, sont basées sur des géométries essentiellement planes ou 2D. Cependant, avec les progrès récents, il est possible d'étudier les géométries 3D dans lesquelles les skyrmions 3D peuvent être stabilisés. La thèse présentée ici vise à étudier les skyrmions 3D dans de telles géométries de ferromagnétiques non centrosymétriques à l'aide de simulations micromagnétiques par la méthode des éléments finis (FEM). Les matériaux ferromagnétiques non-centrosymétriques, par exemple FeGe, possèdent une interaction DMI intrinsèque qui peut stabiliser les skyrmions 3D de type Bloch. Dans notre étude, nous trouvons de multiples états d'équilibre chiral et des effets dynamiques de l'aimantation complexes dans les géométries nanoscopiques 3D fondamentales de ces matériaux, comme discuté en détail dans la partie résultats. La thèse est principalement divisée en trois parties, à savoir la théorie, les méthodes et les résultats. La première partie décrit la théorie du micromagnétisme et des skyrmions magnétiques 3D, la deuxième partie contient les méthodes numériques utilisées pour la mise en œuvre des simulations micromagnétiques FEM / BEM, et la troisième partie contient les principaux résultats obtenus grâce à nos études sur les géométries nanoscopiques 3D de FeGe, un ferroaimant non-centro-symétrique.

La théorie du micromagnétisme [16] décrit les structures de l'aimantation sur l'échelle de longueur submicrométrique dans les matériaux magnétiques.

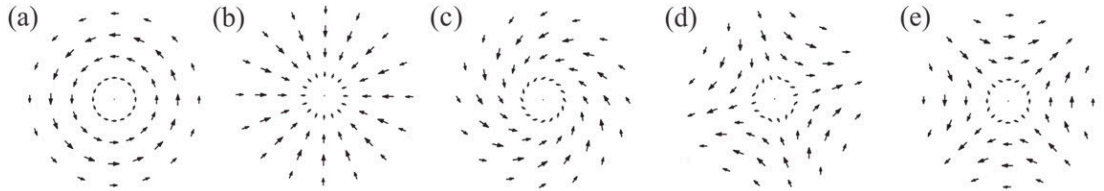
Les échelles de longueur considérées sont suffisamment grandes pour que la structure atomique du matériau soit ignorée (approximation du continu) mais suffisamment petites pour résoudre des structures magnétiques telles qu'une paroi de domaine, un vortex, ou dans notre cas, un skyrmion magnétique. L'hypothèse centrale du modèle est que les forces d'alignement dans le matériau magnétique sont suffisamment fortes pour maintenir l'aimantation parallèle sur une échelle de longueur caractéristique bien au-dessus de la constante du réseau cristallin. Ceci est justifié par l'effet dominant de l'échange ferromagnétique sur les échelles de longueur courte. L'énergie totale d'un système magnétique dépend de la disposition de l'aimantation, et elle est composée de plusieurs contributions en fonction des propriétés respectives des matériaux. Alors que certaines de ces contributions, comme l'énergie de désaimantation et l'énergie Zeeman, peuvent être décrites par la magnétostatique classique, d'autres comme l'énergie d'échange, la DMI et l'énergie d'anisotropie magnétocristalline ont une origine quantique.

Pour simuler les géométries nanoscopiques d'un matériau non-centrosymétrique, nous considérons les interactions suivantes. Premièrement, l'échange ferromagnétique, qui favorise l'alignement homogène de l'aimantation, avec des moments magnétiques parallèles. Deuxièmement, l'interaction DMI intrinsèque du matériau (du type dit « bulk »), qui favorise la disposition hélicoïdale de l'aimantation. Troisièmement, les interactions magnétostatiques, qui favorisent la formation de structures de fermeture de l'aimantation. Enfin, l'interaction Zeeman, qui favorise l'alignement de l'aimantation dans la direction d'un champ magnétique appliqué extérieurement. Pour les études présentées dans la thèse, nous considérons le matériau comme isotrope et ignorons l'apport de l'anisotropie magnétocristalline. Les interactions mentionnées ci-dessus contribuent individuellement à l'énergie totale du système, et une dérivée fonctionnelle de l'énergie totale par rapport à l'aimantation donne le champ effectif total observé dans le matériau.

La dynamique de l'aimantation est décrite par l'équation de Landau-Lifshitz-Gilbert (LLG) [17] en tenant compte du champ effectif total calculé. L'équation comprend deux termes : un terme de précession, qui décrit la rotation de l'aimantation autour du champ effectif, et un terme d'amortis-

sement phénoménologique, qui décrit la relaxation de l'aimantation dans la direction du champ effectif. Ainsi, l'équation LLG décrit l'évolution de l'aimantation dans le temps, y compris les effets dynamiques tels que les ondes de spin, les modes oscillatoires normaux de l'aimantation et les processus de renversement de l'aimantation. En présence d'un courant polarisé en spin, l'équation LLG peut être étendue pour inclure le couple de transfert de spin supplémentaire (spin-transfer torque, STT) suite aux travaux de Zhang et Li [18]. La valeur locale du STT agissant sur l'aimantation dépend de la distribution spatiale de l'aimantation et de la densité de courant.

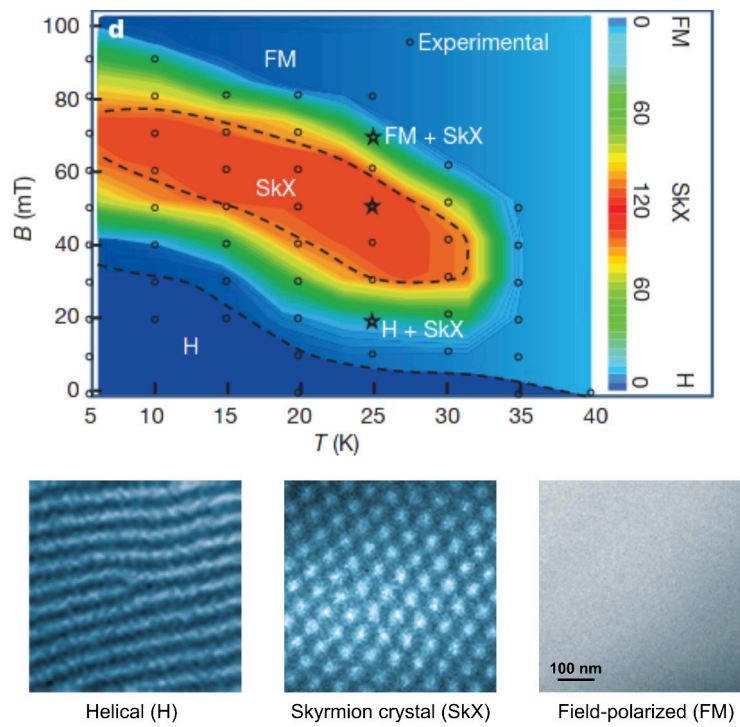
Bogdanov et al. [18–22] ont obtenu une solution analytique pour la configuration d'aimantation d'un skyrmion axisymétrique (par exemple, dans le plan xy), qui est homogène le long de la direction perpendiculaire (dans la direction z). Le terme d'énergie totale, qui comprend les contributions de l'interaction d'échange ferromagnétique, du DMI, de l'anisotropie magnétocristalline, de l'interaction magnétostatique et de l'énergie Zeeman, est minimisé pour ces solutions, où l'expression de la contribution énergétique DMI est exprimée comme une combinaison d'invariants de Lifshitz dont la forme dépend de la symétrie du cristal. En outre, l'interaction magnétostatique est approximativement représentée comme un terme local, sous la forme d'une anisotropie effective, et par conséquent, les solutions sont supposées être axisymétriques [18]. De cette manière, cinq solutions primaires pour les configurations des skyrmions magnétiques sont obtenues et leur composante d'aimantation dans le plan est représentée sur la figure ci-dessous.



Sur les cinq configurations magnétiques prédites pour le skyrmion, seules trois ont été observées expérimentalement jusqu'à présent, correspondant à (a), (b) et (e), qui sont respectivement de type Bloch, de type Néel et anti-skyrmion. Les skyrmions de Bloch sont observés dans des ferromagnétiques

non centrosymétriques de type B20 tels que FeGe, MnSi, etc. [1, 23, 24], et les études présentées dans cette thèse sont basées sur ce type de matériaux ; FeGe pour être exact.

Près de deux décennies après la prédiction théorique de Bogdanov et al., les travaux fondateurs de Mühlbauer et al. [1] en 2009 ont présenté une première observation expérimentale d'un réseau régulier de skyrmion (SkX) dans le MnSi massif, à l'aide d'expériences de diffusion de neutrons aux petits angles (SANS). Ce travail a été suivi d'une étude d'imagerie dans l'espace réel du réseau skyrmion dans un film mince de $\text{Fe}_{1-x}\text{Co}_x\text{Si}$ par Yu et al. en 2010 [23] à l'aide de la microscopie électronique à transmission Lorentz, comme illustré dans la figure ci-dessous.



Les deux études tracent un diagramme de phase de différents états magnétiques stabilisés dans la géométrie en fonction du champ magnétique externe et de la température (l'image ci-dessus montre le diagramme de phase pour des couches minces de $\text{Fe}_{1-x}\text{Co}_x\text{Si}$). Les skyrmions sont observés dans un état cristallin du type skyrmion (SkX) formant un arrangement de triangles (réseau hexagonal).

L'interaction des électrons de conduction avec une configuration d'aimantation topologiquement non triviale d'un skyrmion donne lieu à des phénomènes de transport intéressants. Le spin des électrons de conduction suivent les changements de direction de l'aimantation sous-jacente du skyrmion. Dans ce processus, le spin de l'électron gagne une phase de Berry quantique [25], qui le dévie de la direction du mouvement le long du champ électrique appliqué et induit une contribution supplémentaire d'effet Hall connue sous le nom d'effet Hall topologique (THE). De même, les skyrmions sont traînés le long de la direction du courant électrique à travers le STT et montrent un mouvement transversal, connu sous le nom d'effet Skyrmion Hall (SkHE), comme homologue de l'effet Hall topologique. Sur la base de l'équation LLG, qui tient compte des effets STT, on peut écrire une équation de mouvement pour une configuration de skyrmion rigide selon l'équation de Thiele [26]. Ceci s'est avéré utile pour prédire la dynamique à la fois du cristal de skyrmion et de la configuration isolée d'un skyrmion dans la majorité des cas. Peu de temps après l'observation expérimentale de la phase de cristal skyrmion (SkX) dans MnSi, Yu et al. [2] ont rapporté le mouvement entraîné par le courant de la phase SkX en 2012. On a observé que les skyrmions se déplaçaient à de très faibles densités de courant (de l'ordre de 10^6 A m^{-2}) par rapport aux valeurs requis pour le déplacement de parois de domaine magnétiques précédemment étudiées. Par ailleurs, le mouvement des skyrmions isolés dans la géométrie de nano-pistes confinées s'est montré prometteur car le SkHE a été contrecarré par un effet de répulsion du bord conduisant à un mouvement de skyrmion dans la direction du courant appliqué [7]. Ces observations ont donné une impulsion substantielle à l'étude des skyrmions magnétiques pour les applications de dispositifs de mémoire telles que la géométrie de piste de décalage du type « race track » pour les skyrmions. Cependant, les skyrmions sont expulsés des bords du matériau en raison du SkHE à des densités de courant élevées, ce qui pose toujours un défi pour leur intégration complète dans les dispositifs.

Au cours des dernières décennies, la modélisation numérique est devenue un outil essentiel et bien établi, à égalité avec l'expérimentation et la théorie, pour comprendre les phénomènes de la physique de la matière condensée et

de nombreux autres domaines scientifiques. En magnétisme, les simulations micromagnétiques ont largement contribué à la compréhension des structures magnétiques statiques et de la dynamique de l'aimantation dans des systèmes de plus en plus complexes. Jusqu'à récemment, les chercheurs utilisaient des simulations pour compléter et contribuer à l'interprétation des données expérimentales. Cependant, les simulations micromagnétiques ont évolué pour devenir un outil efficace et fiable pour prédire le comportement des systèmes magnétiques à l'échelle nanométrique.

La théorie du micromagnétisme définit un ensemble d'équations différentielles partielles non linéaires dans l'espace et le temps, qui ne peuvent être résolues analytiquement que pour des cas simplifiés. En général, la solution des équations statiques et dynamiques du micromagnétisme nécessite des méthodes numériques. Puisque nous nous intéressons à l'étude des géométries nanoscopiques 3D, nous utilisons une approche numérique basée sur les éléments finis (FEM). En FEM, on subdivise la région magnétique en une collection d'éléments simplex (tétraèdres pour le cas 3D) qui représentent des cellules de discrétisation pour la simulation, résultant en un maillage tétraédrique irrégulier. Les sommets du maillage sont connus comme les nœuds de discrétisation. À partir des nœuds, il est possible d'interpoler linéairement par morceaux la valeur d'une fonction à l'intérieur des éléments du maillage à l'aide de fonctions de forme. De plus, nous visons à calculer le champ effectif total dans le matériau. Celui peut être obtenue en suivant la formulation faible des équations aux dérivées partielles et l'implémentation numérique ultérieure par la méthode de Galerkin. Une fois le champ effectif calculé, la dynamique de l'aimantation peut être obtenue en intégrant l'équation LLG.

Il est important de choisir la taille de cellule individuelle du maillage suffisamment petite pour résoudre avec précision les structures magnétiques. Pour les matériaux dépourvus d'anisotropie magnétocristalline (comme dans notre cas), la taille caractéristique des cellules de discrétisation ne devrait pas dépasser une longueur correspondant à environ la moitié de la longueur d'échange magnétostatique, donnée par la l'expression $l_s = \sqrt{2A/\mu_0 M_s^2}$ (M_s est l'aimantation de saturation et A est la constante de rigidité d'échange). Dans le cas des matériaux ferromagnétiques non-centrosymétriques, la période

hélicoïdale à longue portée (l_d) est également une échelle de longueur intéressante car elle décrit la longueur correspondant à une rotation complète d'hélices d'aimantation dans le matériau. Cette longueur peut être exprimée par $l_d = 4\pi A/|D|$. Pour les études présentées dans cette thèse, le matériau d'intérêt est le FeGe, et pour ce matériau, on obtient $l_s = 9,7$ nm, $l_d = 70$ nm. Pour la discrétisation, nous choisissons une longueur caractéristique maximale du maillage égale à 4,3 nm (à partir des paramètres du matériau FeGe indiqués dans le tableau ci-dessous).

Paramètres du matériau FeGe		
Saturation magnetization (M_s)		384 kA m^{-1}
Exchange stiffness (A)		$8.87 \times 10^{-12} \text{ J m}^{-1}$
DMI constant (D)		$1.58 \times 10^{-3} \text{ J m}^{-2}$

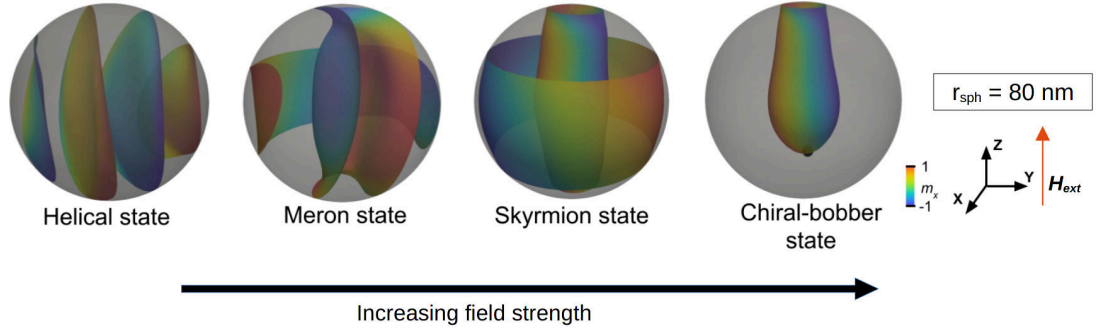
Les études de simulation présentées dans cette thèse ont été réalisées avec notre logiciel micromagnétique à base d'éléments finis (FEM) développé en interne. Notre progiciel micromagnétique, nommé tetmag, a été développé à l'IPCMS de Strasbourg par R. Hertel, dont l'équipe a une longue tradition dans la conception et l'optimisation de logiciels micromagnétiques [27–29]. Le logiciel implémente à la fois la parallélisation basée sur les processeurs CPU et les processeurs graphiques (GPU) pour un calcul accéléré. En outre, les matrices de type $\mathcal{H}2$ sont utilisées pour une gestion efficace de la mémoire dans les calculs magnétostatiques [30]. Pour valider et comparer les résultats obtenus avec notre logiciel de simulation, nous avons collaboré avec d'autres collègues travaillant sur ce domaine. En particulier, nous avons réalisé des études de simulation statique sur la structure d'un skyrmion se formant dans un disque FeGe d'une taille spécifique et comparé en détail les résultats obtenus avec différents codes [31]. Ce test a donné un accord parfait entre les profils skyrmion aussi bien que les énergies obtenus d'une part avec notre code tetmag et, d'autre part, avec ceux calculés en utilisant d'autres logiciels micromagnétiques bien établis tels que MuMax3 [32] ou OOMMF [33]. La réalisation de telles comparaisons est une procédure bien établie dans le micromagnétisme numérique, où divers problèmes dit

« standard » sont couramment utilisés pour comparer les résultats obtenus à partir de différents codes [34]. Une comparaison réussie avec les résultats obtenus par d'autres équipes permet de fournir une confiance scientifique élevée et améliore la crédibilité des résultats numériques obtenus avec un logiciel de simulation.

L'étude de la structure 3D de l'aimantation dans des matériaux non-centrosymétriques a révélé une variété de nouvelles structures comme les tubes skyrmion, les bobbers chiraux et les structures de points de Bloch dans les aimants hélicoïdaux [35, 36]. Dans ces types de matériaux, cependant, l'impact du confinement nanométrique 3D et les effets de taille finie sur les états magnétiques n'avait pas encore été étudié en détail. Pour étudier l'influence du confinement 3D à l'échelle nanométrique sur les états de l'aimantation se formant dans un matériau héliomagnétique, nous réalisons des simulations micromagnétiques par éléments finis sur des nanosphères de FeGe. Malgré la simplicité de la forme géométrique, on trouve des structures magnétiques très complexes dans de telles nanosphères, qui varient en fonction de la taille des particules et du champ appliqué. Cette complexité résulte des propriétés magnétiques intrinsèquement chirales du matériau non-centrosymétrique et des contraintes imposées par la taille finie de l'échantillon. Nous présentons la distribution des états fondamentaux de l'aimantation en fonction du rayon de la nanosphère et du champ magnétique externe. De plus, nous étudions l'impact des interactions magnétostatiques sur ces structures magnétiques, car elles jouent un rôle central dans le cas de nanoparticules ferromagnétiques.

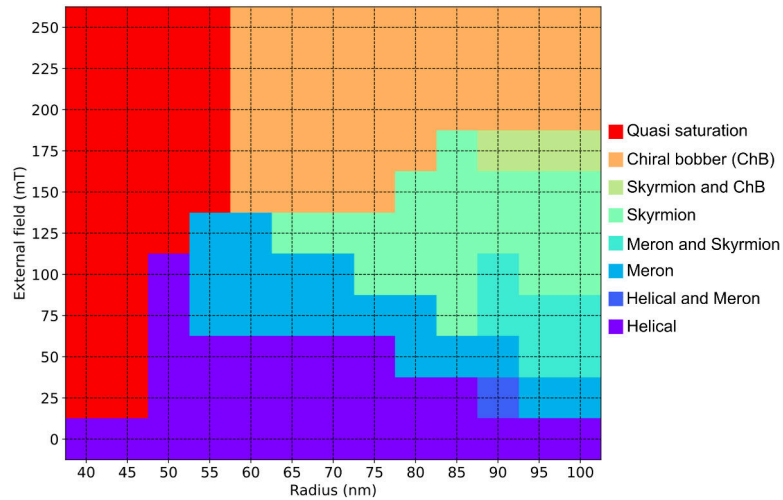
En faisant varier le rayon de la nanosphère et le champ magnétique externe de 40 à 100 nm et de 0 à 250 mT, respectivement, nous obtenons cinq états magnétiques d'équilibre principaux dans le système, à savoir, hélicoïdal, méron, skyrmion, bobber chiral et état de saturation. En tant qu'états fondamentaux (états d'énergie minimale), ils sont obtenus dans l'ordre présenté ci-dessus avec un champ externe croissant à un rayon de nanosphère constant.

L'état hélicoïdal est caractérisé par une rotation continue de l'aimantation selon un axe presque perpendiculaire au champ appliqué. Alterna-



tivement, l'agencement de l'aimantation peut être interprété comme une séquence périodique de domaines étroits alternés, pointant le long et opposé à la direction du champ magnétique externe, et séparés par des parois de Bloch avec le même sens de rotation. Les domaines alternés peuvent être visualisés à l'aide d'iso-surfaces correspondant à $m_z = 0$, et ces iso-surfaces peuvent être considérées comme des parois de domaines hypothétiques séparant les domaines. Nous utilisons cette représentation pour montrer les états d'aimantation d'équilibre dans l'image ci-dessus. Dans l'état hélicoïdal, la distance entre les deux domaines pointant dans la même direction correspond à une rotation complète d'aimantation, c'est-à-dire à la longueur l_d du matériau. L'interprétation de l'état hélicoïdal comme une structure magnétique avec des domaines alternés est utile afin de comprendre l'évolution de la structure à mesure que le champ appliqué est augmenté. Les structures de domaine magnétique réagissent à une augmentation du champ externe de telle sorte que les domaines orientés parallèlement au champ augmentent en taille, au détriment de domaines orientés de manière anti-parallèle à celui-ci. La transition d'un état hélicoïdal à un état méron avec une intensité de champ externe croissante peut être comprise dans ce sens. La structure méron peut être décrite comme une forme hybride de deux structures chirales différentes, spécifiquement, d'une moitié hélicoïdale et de l'autre moitié comme un état skyrmion. En ce sens, l'état méron peut être considéré comme une structure transitoire ou intermédiaire entre ces deux états. L'augmentation supplémentaire du champ externe augmente la tendance à étendre les régions dans lesquelles l'aimantation est orientée le long de la direction du champ. Cette tendance est équilibrée par la nécessité

du système de préserver les spirales magnétiques induites par l'interaction combinée de l'interaction DMI et de l'échange ferromagnétique. Dans la représentation avec les iso-surfaces, l'évolution d'un état méron dans un champ externe croissant peut être interprétée comme une deuxième flexion de ces parois virtuelles vers l'intérieur, les reliant maintenant aussi du côté opposé et résultant ainsi en un noyau central circulaire dans lequel l'aimantation est orientée opposé à la direction du champ appliqué. La configuration symétrique axiale qui en résulte est l'état de skyrmion. Si le champ externe est encore augmenté, le domaine circulaire environnant, dans lequel l'aimantation est orientée le long du champ externe, continue de croître, et le noyau central de l'état de skyrmion pointant dans la direction opposée du champ rétrécit en taille, se terminant maintenant dans un point de Bloch. Une telle structure est connue comme un état de bobber chiral [38]. En analysant plus en détail la structure de l'aimantation en prenant une section transversale horizontale au-dessus et en dessous du point de Bloch, on trouve les structures magnétiques sur ces sections transversales correspondant à celle d'un skyrmion Bloch 2D et à un état de saturation 2D, respectivement. Par conséquent, on peut considérer cette configuration comme un état magnétique de transition entre le skyrmion et l'état de saturation. Enfin, à un champ externe élevé, la contribution d'énergie Zeeman domine et la majeure partie de l'aimantation s'aligne dans la direction du champ appliqué, résultant dans un état de saturation.



Dans le paragraphe précédent, l'évolution de la configuration de l'aimantation des différents états magnétiques a été discutée en fonction d'un champ externe croissant. Cependant, la stabilité de ces structures dépend également de la taille des particules. Pour étudier cette dépendance, nous avons effectué de nombreuses simulations qui nous ont permis de déterminer les plages de stabilité des cinq états, comme résumé dans le diagramme de phase présenté dans la figure ci-dessus. Le diagramme affiche la configuration à plus faible énergie (les états fondamentaux) en fonction du champ magnétique externe et du rayon des nanosphères.

De façon remarquable, la phase skyrmion n'existe pas dans les nanosphères de FeGe en dessous d'un rayon de 65 nm. Cette taille est comparable à la période hélicoïdale à longue portée l_d (70 nm) du matériau, qui à son tour signifie une rotation complète de l'aimantation. Bien qu'il n'y ait pas de connexion directe entre la structure d'une spirale de spin et l'état de skyrmion, il est intuitivement clair qu'une structure de skyrmion ne peut pas se former dans un échantillon qui est trop petit pour permettre deux rotations complètes de l'aimantation sur le diamètre de la sphère. La tendance de la disparition successive de phases d'équilibre se poursuit alors que nous diminuons encore le rayon. En dessous d'un rayon de 50 nm, les phases bobber-chiral et méron cesse également d'exister. À cette taille, le diamètre de la nanosphère se rapproche de l_d , et par conséquent, seules la phase hélicoïdale (aux champs externes inférieurs) et la phase de saturation (aux champs externes supérieurs) sont stables. Pour des rayons inférieurs à 40 nm, seule la phase de saturation reste car la taille des particules tombe en dessous de l_d , ne laissant ainsi pas la place pour une seule rotation complète de l'aimantation. Une distinction claire des cinq configurations principales mentionnées ci-dessus n'est possible que dans des tailles de particules allant jusqu'à un rayon d'environ 90 nm. Dans des nanosphères plus grandes, des structures hybrides apparaissent, qui peuvent contenir, par exemple, à la fois une structure méron et skyrmion, ou un skyrmion ainsi qu'un bobber chiral. À ces plus grandes tailles, l'impact de la forme sphérique de la particule sur la structure magnétique diminue et on observe une transition progressive vers un quasi-continuum d'états d'aimantation chiraux tridimensionnelles,

comme cela se produirait dans le matériau massif.

Après avoir décrit les différentes structures magnétiques et leur formation résultant des interactions concurrentes de l'énergie Zeeman, de l'échange ferromagnétique et du DMI, nous discutons maintenant de l'impact du champ dipolaire (magnétostatique) sur ces configurations et leur distribution. Pour analyser l'impact des interactions magnétostatiques, nous avons recalculé le diagramme de phase en excluant le champ de désaimantation et la densité d'énergie magnétostatique de la simulation. Nous avons constaté que cela ne modifie pas les résultats de manière appréciable, ce qui donne essentiellement le même diagramme de phase. Ainsi, pour illustrer davantage l'impact quantitatif du champ dipolaire (ou son absence), nous représentons l'énergie provenant du champ dipolaire en pourcentage de l'énergie totale pour les états d'équilibre respectifs. On constate que pour tous les états fondamentaux, l'énergie de désaimantation ne dépasse pas 10% de l'énergie totale. Ceci indique que, bien que non strictement négligeables, les interactions magnétostatiques ne jouent pas un rôle dominant dans la formation des configurations magnétiques et leur distribution en tant qu'états d'équilibre. L'énergie de désaimantation ne devient appréciable que pour les petits rayons et les champs élevés, où les particules sont dans un état presque saturé. Dans les autres états d'équilibre, la nature hélicoïdale - induite par l'interaction DMI - des structures de l'aimantation réduit déjà l'énergie magnétostatique en formant des états similaires à des domaines qui alternent périodiquement. Ainsi, au moins pour les ferromagnétiques non-centrosymétriques de géométrie nanosphérique, nous concluons que les interactions magnétostatiques ne jouent pas un rôle dominant dans la stabilisation et la distribution des états fondamentaux de l'aimantation.

Récemment, le skyrmion et le bobber chiral (ChB) ont été proposés comme structures magnétiques pouvant potentiellement représenter des unités fondamentales de stockage d'information qui pourraient être utilisées dans des nouveaux dispositifs de mémoire non-volatiles du type « race-track ». Il a été démontré que ces deux types de structures peuvent coexister et qu'elles possèdent des empreintes digitales de magnéto-transport différentes [37, 38], ce qui renforce leur intérêt pour un dispositif de mémoire. Ici, nous discu-

tons d'un mécanisme pour basculer de manière contrôlable entre les deux états dans une géométrie de disque FeGe en utilisant de courtes impulsions de champ externe. Sur la base de notre étude des nanosphères (décrite dans les paragraphes précédents) nous comprenons que, de manière générale, si le champ externe est augmenté, l'état ChB devient énergétiquement favorable par rapport à l'état skyrmion. Nous utilisons ce fait pour basculer entre les deux états en appliquant une impulsion gaussienne supplémentaire qui permet au système de surmonter la barrière d'énergie séparant les deux états.

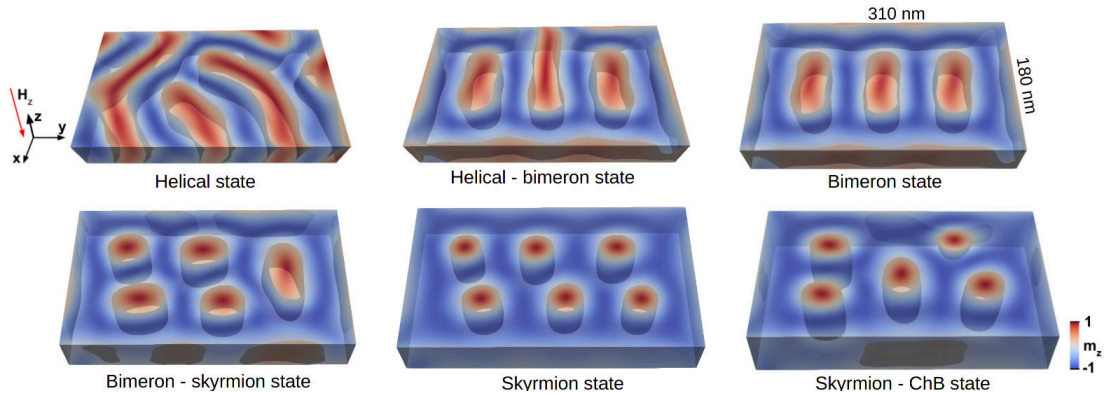
La conversion d'un skyrmion vers un état ChB est étudiée dans un disque FeGe de rayon 80 nm et d'épaisseur 70 nm. Tout d'abord, nous stabilisons l'état de skyrmion en appliquant un champ magnétique externe constant de 190 mT dans la direction z positive. L'état skyrmion est l'état fondamental à cette valeur de champ (et l'état ChB est un état d'équilibre métastable). Nous augmentons le champ externe à 220 mT à partir de 190 mT, modifiant ainsi la différence d'énergie entre les deux états. Avec l'augmentation du champ externe, la différence entre les énergies du skyrmion et de l'état ChB diminue et change de signe. Même si les deux configurations ont changé leur rôle d'état fondamental et d'état métastable, la transition réelle du skyrmion à l'état ChB nécessite de surmonter une barrière d'énergie, car l'état ChB héberge un point Bloch qui doit être injecté. Nous appliquons une impulsion de champ gaussien d'une intensité de 350 mT et d'une durée de 235 ps dans la direction y positive pour y parvenir. L'application d'une impulsion de champ externe nucléé un point de Bloch à la surface supérieure de l'état skyrmion, convergeant finalement vers l'état ChB. De même, l'inversion du processus ramène le système à l'état de skyrmion. Tout d'abord, nous réduisons le champ magnétique externe à 190 mT à partir de 220 mT. Ensuite, nous appliquons une impulsion de champ de forme gaussienne d'une intensité de 350 mT et d'une largeur de 150 ps, dans la direction z négative, pour surmonter la barrière d'énergie. De cette manière, nous pouvons alterner entre le skyrmion et l'état ChB en modifiant d'abord la différence d'énergie des deux états en changeant l'intensité du champ externe statique et enfin en surmontant la barrière menant à la transition avec de courtes

impulsions de champ externe.

Il est bien connu que les skyrmions magnétiques sont proposés comme étant des candidats idéaux pour le stockage de données dans des nouveaux dispositifs de mémoire nanométriques fonctionnant sur le principe d'un registre à décalage (« race-track memory »). Cependant, il est nécessaire d'affronter quelques défis tels que le SkHE qui fait que le skyrmion est dévié perpendiculairement à la direction du courant appliqué [39] de même que la diffusion du skyrmion [40] qui entrave considérablement ce progrès. Pour obtenir le contrôle de la position des skyrmions, différentes méthodes ont été proposées, par exemple, l'introduction d'encoches sur les bords pour éviter la diffusion du skyrmion [41] et le mouvement du skyrmion en utilisant des anti-ferromagnétiques synthétiques (SAF). Les SAF contiennent des couches de skyrmions couplées de manière antiferromagnétique, qui annulent ainsi le SkHE [42]. Cependant, ces méthodes posent leurs défis individuels tels que la possibilité d'expulsion du skyrmion au niveau des encoches ou l'exigence d'une grande précision pour fabriquer des matériaux SAF.

Nous constatons que, dans les ferromagnétiques non-centrosymétriques, il est possible de contraindre les skyrmions à la région souhaitée de la géométrie du matériau avec de simples modulations d'épaisseur dans le matériau. Notre étude sur les nanosphères [43], ainsi que des études similaires sur diverses géométries d'éléments en couches minces de ferromagnets à symétrie d'inversion spatiale brisée [5, 36, 44–47] révèlent la dépendance de la stabilité de l'état de skyrmion tridimensionnel à la fois en fonction de champ appliqué et des dimensions géométriques du matériau. Ainsi, on peut affirmer qu'il est possible de créer des régions préférentielles où, à un champ magnétique externe donné, la formation d'un skyrmion est énergétiquement favorable. Dans un premier temps, nous calculons le diagramme de phase d'une géométrie de film rectangulaire de FeGe en modifiant l'épaisseur du film et le champ magnétique externe pour obtenir la distribution des états d'énergie minimale.

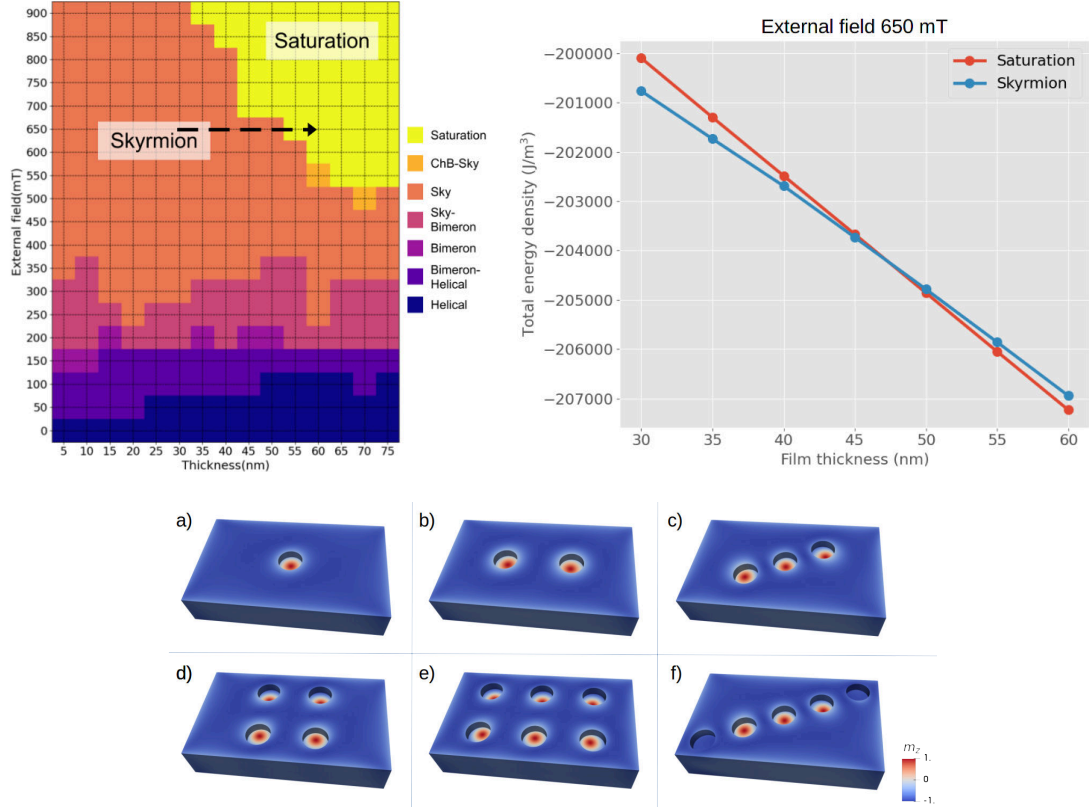
Dans le processus de calcul du diagramme de phase, nous obtenons quatre états principaux d'équilibre magnétique, à savoir, l'état hélicoïdal, bimeron, skyrmion et saturation, comme indiqué ci-dessus. On retrouve



également la coexistence de ces états fondamentaux dans cette géométrie tels que l'état hélicoïdal-bimeron, bimeron-skyrmion et skyrmion-ChB. Les configurations magnétiques des états d'équilibre primaire présentent des similitudes avec celles obtenues dans l'étude des nanosphères. L'état hélicoïdal représente des domaines alternés en raison de la présence d'hélices magnétique dans le système. L'état bimeron peut être interprété comme un skyrmion latéralement étiré, avec la même charge topologique qu'un skyrmion. L'état skyrmion est celui des skyrmions 3D bien connus de type Bloch. Dans l'état de saturation, qui se produit à des champs externes élevés, où la majeure partie de l'aimantation pointe dans la direction du champ externe. Nous nous intéressons principalement au skyrmion et à l'état de saturation car le but est de créer des régions dans la géométrie où l'état de skyrmion est énergétiquement favorable, tandis que l'état de saturation est favorable partout ailleurs.

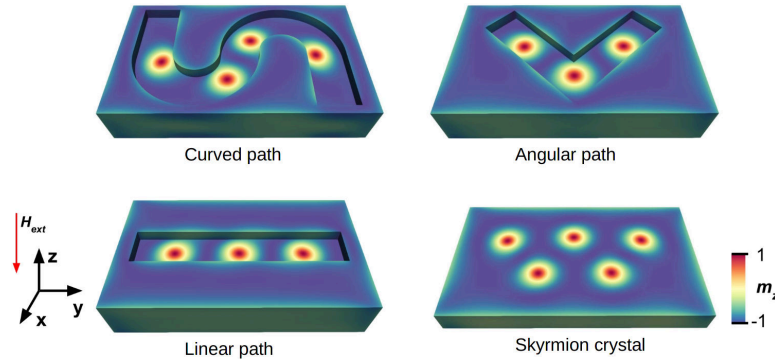
Le diagramme de phase ainsi obtenu est représenté sur l'image ci-dessus. Le diagramme montre une frontière claire entre le skyrmion et l'état de saturation. On peut observer qu'à un champ externe fixe, l'état de saturation devient énergétiquement préférable en augmentant l'épaisseur du film. Nous traçons en outre la densité d'énergie totale des deux états à un champ externe constant de 650 nm en modifiant l'épaisseur du film de 30 à 60 nm. Le graphique confirme que, à champ externe constant, l'état de skyrmion est énergétiquement favorable par rapport à un état de saturation si l'épaisseur de film est faible.

En utilisant cette argumentation, tout d'abord, nous proposons un moyen



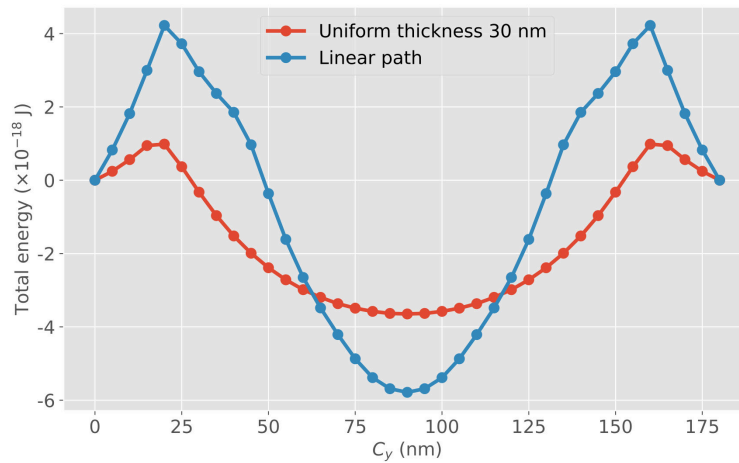
de contraindre les skyrmions dans des cavités cylindriques symétriques dans un film de FeGe, en forme semblable à l'envers d'un nanodot avec un rayon 20 de nm comme le montre l'image ci-dessus. L'épaisseur de la couche dans les cavités est de 30 nm alors qu'elle est de 60 nm partout ailleurs. Selon le diagramme de phase du film présenté précédemment, à une valeur de champ externe de 650 mT, l'état de skyrmion est l'état fondamental à 30 nm tandis que l'état de saturation est l'état fondamental à 60 nm. Par conséquent, les cavités représentent des positions énergétiquement favorables pour les skyrmions. A l'aide de cette modulation d'épaisseur à champ externe constant, nous montrons qu'il est possible de contrôler la position des skyrmions. Comme le montre l'image ci-dessus, il est possible de forcer les skyrmions, dans une certaine mesure, à former des agencements non naturels tels qu'un agencement diagonal ou un agencement en treillis carré. Ces agencements sont bien différents par rapport à la structure hexagonale qui se forme naturellement dans une couche homogène. De plus, les skyrmions conservent

leur nature topologique lorsqu'ils sont piégés dans les cavités. Cette possibilité de générer des endroits préférentiels pour les skyrmions peut avoir des implications sur le développement de dispositifs, par exemple dans les applications magnoniques, où la diffraction de Bragg des magnons dépend de la disposition des skyrmions, ou dans les pistes du type race-track pour déterminer la position des skyrmions et ainsi contraindre leur diffusion. Cela étant dit, les cavités ne représentent que des emplacements énergétiquement préférés pour les skyrmions, qui peuvent également se former dans d'autres parties de la géométrie. De plus, il n'est pas toujours possible de piéger les skyrmions dans les cavités comme, par exemple, dans la géométrie illustrée en bas à gauche dans l'image ci-dessus où nous n'avons pas pu stabiliser les skyrmions dans les deux cavités proches aux limites de l'échantillon à cause de la répulsion des skyrmions aux bords [48]. De plus, l'espacement des cavités dans la géométrie est également important en raison de la répulsion skyrmion-skyrmion [48], et par conséquent, nous avons gardé une distance minimale de 70 nm (correspondant à la valeur l_d de FeGe) entre les cavités.



Deuxièmement, de la même manière, nous constatons qu'il est possible de contraindre les skyrmions à des chemins minces symétriques creusés dans ces éléments de couches de FeGe comme le montre l'image ci-dessus. Ici aussi, l'épaisseur des chemins minces est de 30 nm alors que pour le reste du film elle est de 60 nm. À un champ externe de 650 mT, les skyrmions sont contraints au chemin central. De plus, nous calculons la barrière d'énergie rencontrée par un skyrmion isolé, par exemple, dans une géométrie de chemin linéaire (en bas à gauche dans l'image ci-dessus). La présence d'une telle barrière oblige les skyrmions à former un arrangement linéaire arti-

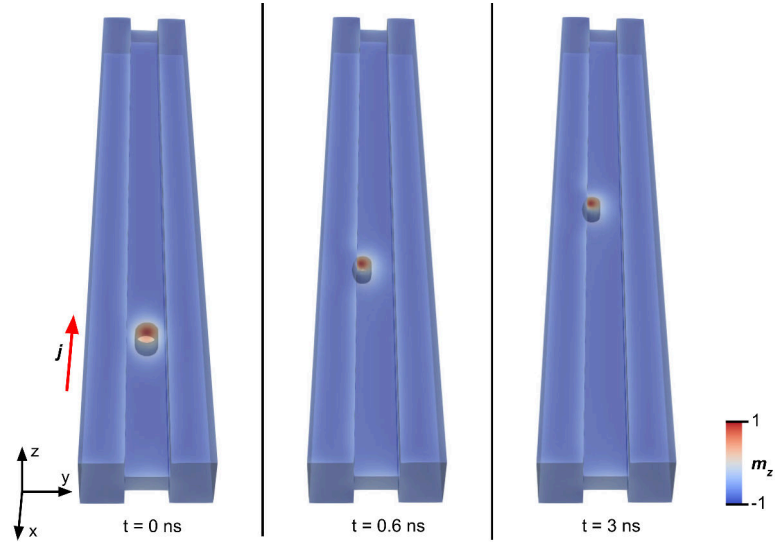
ficiel par rapport à l'arrangement hexagonal naturel (voir en bas à droite dans l'image ci-dessus). Pour calculer la barrière d'énergie, nous calculons l'énergie totale du système lorsque la configuration (artificiellement stabilisée) d'un skyrmion isolé se déplace à travers la barrière d'épaisseur le long de la largeur dans la géométrie du trajet linéaire. Cependant, ce processus n'est pas trivial car il nécessite que la configuration skyrmion soit stabilisée à des positions intermédiaires, pare exemple où une moitié de la configuration skyrmion est sur la barrière épaisse tandis que l'autre moitié est sur le chemin d'épaisseur plus faible. Pour stabiliser une telle configuration, nous fixons le noyau du skyrmion à une position définie en appliquant un champ local dans une petite région dans laquelle le noyau du skyrmion pointe dans la même direction. Ensuite, nous relaxons le système et calculons l'énergie totale du système. Avant d'évaluer la valeur finale de la barrière d'énergie, nous soustrayons la contribution énergétique Zeeman du champ externe local qui est utilisé pour fixer la position du skyrmion.



Nous répétons la même procédure pour calculer la barrière d'énergie rencontrée par un skyrmion isolé dans un film d'épaisseur uniforme, c'est-à-dire en l'absence de barrière d'épaisseur, et la traçons avec le calcul précédent en fonction de la coordonnée y (le long de la largeur) du centre de skyrmion, comme montré dans l'image ci-dessus. On constate qu'en présence de la barrière d'épaisseur, la configuration skyrmion isolée fait face à une barrière d'énergie deux fois plus élevée par rapport à une couche d'épaisseur

uniforme.

La dynamique des skyrmions contraints est étudiée comme une prochaine étape logique. Nous divisons l'étude en principalement deux parties. Premièrement, nous constatons qu'il est possible de contrer le SkHE indésirable avec des barrières d'épaisseur dans une géométrie de piste en forme de « H ». Un skyrmion isolé, stabilisé dans le chemin central d'épaisseur faible, est déplacé à l'aide d'un courant polarisé en spin. Deuxièmement, nous étudions la fréquence des modes d'aimantation des skyrmions géométriquement contraints et constatons que celle-ci dépend de la barrière induite par la géométrie du matériau.



La possibilité de contrer (ou d'annuler) le SkHE indésirable en présence d'un courant polarisé en spin a fait l'objet d'intenses recherches récemment, comme indiqué précédemment. L'expulsion de skyrmion des bords du dispositif en raison de SkHE est un obstacle à des applications par ailleurs prometteuses dans les dispositifs de mémoire. Nous constatons que les modulations d'épaisseur qui ont été utilisées précédemment pour contraindre géométriquement le skyrmion à des cavités minces ou des chemins minces peuvent également être utilisées pour contrer le SkHE en présence d'un courant. Inspirés de la géométrie de la trajectoire linéaire, nous proposons une nouvelle géométrie de rail en forme de H, avec des barrières d'épaisseur sur

les bords latéraux, comme le montre l'image ci-dessus. Tout d'abord, un skyrmion isolé est stabilisé dans le chemin central et plus mince en présence d'un champ externe de 700 mT appliqué le long de la direction z . Ensuite, le skyrmion est déplacé à l'aide d'un courant appliqué dans la direction x . A titre de comparaison, nous répétons la même simulation pour une piste d'épaisseur uniforme et constatons que le skyrmion nécessite une densité de courant quatre fois plus élevée pour être expulsé des bords en présence d'une barrière d'épaisseur. De plus, nous étudions la dépendance de la vitesse du skyrmion dans la piste H en fonction de la densité de courant et le rapport α/β . Dans les deux cas, nous trouvons une relation linéaire pour la vitesse du skyrmion, qui peut être expliquée plus précisément à l'aide de l'équation de Thiele, pointant vers une configuration de skyrmion rigide dans la géométrie de la voie H . Ainsi, en utilisant des simples modulations d'épaisseur dans la géométrie, nous montrons qu'il est possible de créer un puits de potentiel unidimensionnel pour les skyrmions qui peuvent guider leur mouvement le long de la piste et contrer l'effet SkHE.

L'étude des modes dynamiques des configurations magnétiques dans les nanoparticules a été d'un grand intérêt dans le micromagnétisme, à la fois du point de vue de la physique fondamentale et aussi pour l'application. Ces études ne révèlent pas seulement les propriétés magnétiques du matériau, mais aussi l'interaction de la configuration de l'aimantation avec les ondes électromagnétiques peut indiquer des transitions de phase possibles. Ainsi, nous étudions comment le confinement géométrique influence les modes intrinsèques d'un skyrmion. Nous proposons une géométrie d'un disque nanométrique avec une barrière d'épaisseur au bord (« disque avec barrière ») pour obtenir un skyrmion isolé et géométriquement contraint. Dans le cas d'un disque avec barrière, on obtient principalement deux modes latéraux et deux modes respiratoires. Ces types de modes peuvent également être identifiés dans l'analyse des oscillations des skyrmions libres (dans de nanodisques sans barrière d'épaisseur). Cependant, leur fréquence et amplitude dépendent de la géométrie du matériau, c'est-à-dire de la largeur de la barrière d'épaisseur, et s'écartent significativement de la fréquence et de l'amplitude des modes de skyrmions dans des disques sans barrière

d'épaisseur. La dépendance de la fréquence des modes à la largeur de la barrière d'épaisseur ouvre la possibilité de régler la fréquence des modes, en fonction de la géométrie choisie. Par exemple, à l'instar des nano-cavités de rayon uniforme présentées dans l'étude précédente, on peut proposer des nano-cavités de rayons variables avec des skyrmions géométriquement contraints au centre, où les modes collectifs peuvent montrer plusieurs pics de fréquence correspondant à la distribution des rayons.

Pour conclure, nous présentons une étude complète des skyrmions tridimensionnels dans des géométries confinées. Nous identifions divers états magnétique représentant un équilibre énergétique comme l'état hélicoïdal, (bi-)méron et bobber chiral, qui sont stabilisés dans des matériaux hébergeant des structures héliomagnétiques tridimensionnelles. Nous utilisons la dépendance au champ externe de la stabilité du skyrmion pour étudier la possibilité de basculer entre un état de skyrmion et un bobber chiral. Nous utilisons aussi le fait que l'énergie du skyrmion dépendent de la géométrie pour contraindre les skyrmions dans des régions souhaitées. Cette possibilité de manipuler la position des skyrmions peut être très utile pour des applications dans les dispositifs. Par exemple, le concept des skyrmions contraints statiquement dans différents agencements de « poches » ou dans des chemins étroits peut trouver des application dans le stockage magnétique. Il ouvre aussi la voie à un développement de méta-matériaux magnoniques à base de cristaux artificiels de skyrmion. Ces contraintes géométriques influencent aussi la dynamique des skyrmions, comme nous l'avons démontré dans une géométrie de dispositif de registre à décalage en forme de H, où elles peuvent contrer l'effet SkHE. De plus, la possibilité d'influencer la fréquence des modes magnétiques des skyrmions en fonction de la géométrie du matériau peut être intéressante pour des dispositifs hyperfréquences.

Acknowledgements

Performing my Ph.D. was most likely the biggest challenge of my life, at least to date. Successful completion of this project would not have been possible without the help from a lot of people and institutions.

The thesis was carried out at Institut de Physique et Chimie de Matériaux de Strasbourg (CNRS). I want to thank our institute director Pierre Rabu and our head of the DMONS department Yves Henry for warmly hosting me for the duration of the thesis. Also, I want to thank the initiative of excellence of Strasbourg University IDEX (ANR-10-IDEX-0002-02) for financially supporting my thesis. I am grateful to the High-Performance Computing Center of the University of Strasbourg for providing me with the computational resources to carry out the simulations as part of the thesis.

I want to thank the thesis jury members, Joo-Von Kim, Liliana Buda-Prejbeanu, Paul-Antoine Hervieux, and Dietmar Weinmann for a careful review of the thesis and a pertinent discussion at the time of thesis defense which broadened my understanding and outlook of the field. I feel privileged to be able to present my work and defend the thesis in front of you.

My deep gratitude goes to the thesis director, Riccardo Hertel. Riccardo, with your wide experience and deep knowledge of physics, mathematics, and numerics, you guided me through the challenges of the thesis. You always took the time for discussions and group meetings, even for long ones (the Friday meetings); through those discussions, I have learned a lot about the subject of micromagnetism and magnetic skyrmions. You inspired and motivated me to find the best possible solutions. I am extremely thankful for your continuous help and your faith in my work. It was an honor to perform my Ph.D. under your supervision.

I heartily thank Salia Cherifi-Hertel who guided me through the intricacies of French conventions and also regarding the presentation of my scientific work.

I greatly appreciate the help of our department secretary, Véronique Wernher, with institute formalities and for being such a kind person in general.

To all the colleagues and friends I met in Strasbourg I want to thank you for a great time; in particular, Matías Grassi, Sambit Mohapatra, Suvidya-

kumar Homkar, Rajgowrav Cheenikundil Rajendran, Saeel Ismail Momin, Lalit Mohan Kandpal, Shyam, Ritu, and Kajal.

I am indebted to all my friends and family back in India who always backed me up and welcomed me with warmth whenever I visited them.

Finally, I want to thank the most important people, my wife Bhavya, my mother Mamta, and my father Amit. I am so grateful for your unconditional love and support throughout the ups and downs of the journey, and without you, it would have been impossible. To you, I dedicate this thesis.

Déclaration sur l'honneur *Declaration of Honour*

J'affirme être informé que le plagiat est une faute grave susceptible de mener à des sanctions administratives et disciplinaires pouvant aller jusqu'au renvoi de l'Université de Strasbourg et passible de poursuites devant les tribunaux de la République Française.

Je suis conscient(e) que l'absence de citation claire et transparente d'une source empruntée à un tiers (texte, idée, raisonnement ou autre création) est constitutive de plagiat.

Au vu de ce qui précède, **j'atteste sur l'honneur que le travail décrit dans mon manuscrit de thèse est un travail original et que je n'ai pas eu recours au plagiat ou à toute autre forme de fraude.**

I affirm that I am aware that plagiarism is a serious misconduct that may lead to administrative and disciplinary sanctions up to dismissal from the University of Strasbourg and liable to prosecution in the courts of the French Republic.

I am aware that the absence of a clear and transparent citation of a source borrowed from a third party (text, idea, reasoning or other creation) is constitutive of plagiarism.

In view of the foregoing, I hereby certify that the work described in my thesis manuscript is original work and that I have not resorted to plagiarism or any other form of fraud.

Nom : **PATHAK**

Prénom : **Swapneel Amit**

Ecole doctorale : **ED 182 Physique et chimie physique**

Laboratoire : **IPCMS - DMONS**

Date : **14/05/2021**

Signature :

TABLE DES MATIÈRES

1	Introduction	1
I	Theory	11
2	Micromagnetism	12
2.1	Energy terms	14
2.1.1	Exchange energy	14
2.1.2	Dzyaloshinskii-Moriya interaction	16
2.1.3	Demagnetization energy	17
2.1.4	Zeeman energy	19
2.1.5	Effective field	19
2.2	Dynamics of magnetization	20
2.2.1	Landau-Lifshitz-Gilbert equation	20
2.2.2	Current induced dynamics	22
2.3	Magnetic structures	23
2.3.1	Characteristic lengths	23
2.3.2	Magnetic domains and walls	25
3	Magnetic skyrmions	28
3.1	Analytic treatment of magnetic skyrmions	31
3.1.1	Static skyrmion solution	31
3.1.2	Skyrmion in presence of conduction electrons	33
3.2	Studies involving statics and dynamics of 3D skyrmions	35
3.2.1	Skyrmion observation and stability	35

3.2.2	Skyrmion motion under electric current	39
3.2.3	Dynamical modes of magnetic skyrmions	41
3.3	Chiral magnetization structures in 3D	44
3.3.1	Magnetic vortex	45
3.3.2	Bloch point	46
3.3.3	Helical state	47
3.3.4	Chiral-bobber state	48
3.3.5	Other chiral magnetization structures	51
 II Methods		 52
 4 Numerical implementation		 53
4.1	Spatial discretization - Finite element method	55
4.1.1	Simplex Elements	55
4.1.2	Mesh Generation	56
4.1.3	Shape functions, their differentiation and integration	56
4.1.4	Exchange field	60
4.1.5	Magnetostatic field	63
4.2	Temporal discretization - Integration of LLG equation	66
4.3	Simulation software	66
4.3.1	General framework	67
4.3.2	Code architecture and basic features	67
4.3.3	Numerical Implementation of the DMI term	68
4.3.4	Improved magnetostatic field calculation	69
4.3.5	Integration in time	69
 III Results		 71
 5 Three-Dimensional Chiral Magnetization Structures in FeGe Nanospheres		 72
5.1	Magnetic equilibrium states	74
5.1.1	Helical state	75
5.1.2	Meron state	77

5.1.3	Skyrmion state	78
5.1.4	Chiral-Bobber state	82
5.1.5	Saturation state	85
5.2	Phase diagram	85
5.3	Phase diagram cross-sections : energy densities of stable and meta-stable states	87
5.4	Impact of magnetostatic interactions	91
6	Skyrmion-chiral bobber state switching	94
7	Geometric Skyrmion Confinement	100
7.1	Statically constrained skyrmions	102
7.1.1	Equilibrium magnetization states	103
7.1.2	Phase diagram	106
7.1.3	Percentage energy contribution of DMI	108
7.1.4	Geometrically constrained skyrmions in circular pockets	109
7.1.5	Geometrically constrained skyrmions on thin paths	112
7.2	Modeling skyrmion magnetization configuration	114
7.3	Skyrmion potential well	117
7.4	Dynamic skyrmion confinement	120
7.4.1	Dynamic skyrmion confinement in H-track geometry	120
7.4.2	Magnetization modes of confined skyrmion	124
8	Conclusion	135

CHAPITRE 1

Introduction

The study of magnetic skyrmions belongs to the broad subject of magnetism and magnetic materials, possibly one of the oldest physics branches. Not only has the study of magnetism and magnetic materials struck the curiosity of philosophers and scientists over the centuries, but it has also found practical application as early as the late 11th century in making magnetic compasses for navigation, which practically shaped the history of the world [49]. Until the last century, the study's focus was to explore and understand the properties of bulk magnetic materials due to the limitations of fabrication, characterization, and simulation techniques; however, the last century has seen a shift of interest towards the study of nanomagnetism and spintronics [50, 51].

The study of nanomagnetism deals with geometries of magnetic materials with at least one nanoscopic scale dimension. For example, the magnetism of isolated nanoparticles, nanodots, nanowires, thin films, and multilayers falls under this umbrella. Nanomagnetism presents essential differences compared to the magnetism of macroscopic samples. One can ascribe these differences to the changes from bulk geometry that nanoscopic or mesoscopic scales present, i.e., dimensions comparable to characteristic lengths, such as domain wall width, as well as broken translation symmetry at the surface [52], as the surface to volume ratio increases. Another factor that modifies the nanoparticles' magnetic properties is that they are generally in close contact with other physical systems [52], such as a substrate or a capping layer, in the case of most thin films and multilayers. For the nanoparticles, they can be embedded in a solid matrix. In both cases, the magnetic material atoms may feel a strong interaction with its immediate neighborhood. Also, the presence of imperfections and defects becomes more relevant due to reduced dimensions [53, 54]. The spin-wave spectra of samples of nanoscopic dimensions are also modified [55], considering that the excitation wavelengths are comparable to the dimensions of the nanoparticles. Moreover, the dynamic behavior of nanometric size magnetic objects may also differ from macroscopic samples due to thermal fluctuations under the usual experimental conditions. The phenomenon of superparamagnetism [56, 57] is observed in magnetic nanoparticles if the thermal energy becomes comparable to the particles' anisotropy energy, leading to an effectively zero measured magnetic moment.

Nanoscopic magnetic particles have found widespread applications in fields like geology, ferrofluids, and medicine; however, without a doubt, the most successful application has been in magnetic recording devices [58] brought about by spin electronics or

spintronics [59]. The use of spin-valves in hard disk read heads was the first commercial utilization. The spin-valves operate based on the giant magnetoresistive (GMR) effect, for which Albert Fert and Peter Grünberg received the Nobel Prize in 2007. In a device based on the GMR effect, two ferromagnetic layers sandwich a few nanometer thick nonferromagnetic metal spacer. When the magnetization in the two ferromagnetic layers is mutually parallel, the device is in a low resistance state and vice-versa. The spin valve acts as a sensor in the magnetic hard disk's (HDD) read-head, sensing transitions between bits as their magnetization reverses. The spin valves based on GMR and advanced magnetic materials led to a tremendous increase in hard disk drives' areal storage density. Even so, spin-dependent tunneling devices have now replaced the GMR based spin-valve devices. An insulating barrier has replaced the metal spacer in spin-valves, and hence, the room temperature magnetoresistance of the device has increased by a factor of ten. These new devices are known as magnetic tunnel junctions (MTJs) or tunneling magnetoresistance (TMR) devices. Moodera et al. and Miyazaki & Tezuka [60, 61] introduced the MTJs utilizing amorphous AlO_x as the barrier material. Further, Butler et al. and Mathon & Umerski [62, 63] calculated that using crystalline $\text{MgO}(001)$ as insulating spacer leads to higher TMR. This has led to recent room-temperature TMR values as high as 600-1000% [64, 65].

Next critical breakthrough of spintronics is the use of spin moments of the conduction electrons to influence ferromagnetic conductors' magnetization orientation, known as spin-transfer torque (STT). A spin-polarized current, where there is an unequal population of spin-up and spin-down electrons giving it a polarization, exerts a torque on the ferromagnetic material's magnetization moments at high current densities. Berger [66] and Slonczewski [67] laid down the foundations of the STT effects used to switch MTJs and generate oscillations of the magnetization in nano-oscillators. Further, it was recognized that one could use STT to manipulate magnetic domain walls, leading to the proposition of racetrack memory [68] by Parkin in 2008. The racetrack consists of a ferromagnetic nanowire where the bits are encoded with alternating magnetic domains. The domains move past the read and write units with the help of spin-polarized current pulses. The lack of mechanical parts improves the longevity of the device and makes it energy efficient. Hence, the concept of racetrack memory has the potential to replace the current magnetic storage devices in the future. However, significant challenges like Walker breakdown of domain walls and high depinning currents due to material de-

facts limit its comprehensive commercialization. Magnetic skyrmions may solve these challenges and prove a promising alternative to the magnetic domains as fundamental information storage units in a racetrack memory.

Magnetic skyrmions are swirling magnetization configurations with non-trivial topology. They are stabilized in the materials with Dzyaloshinskii-Moriya interaction (DMI) due to the breaking of spatial inversion symmetry either at the material surface or within the bulk. DMI is an anti-symmetric exchange interaction that competes primarily with the symmetric exchange interaction to give chiral magnetization structures. One can consider skyrmions as a static soliton solution of a continuous magnetization vector field in the micromagnetic (continuum) approximation. Hence, they tend to behave as rigid quasi-particles. Due to their non-trivial topology, they possess topological protection, meaning that they cannot be continuously unwound into a saturated state. Topological protection increases skyrmion stability and is a crucial property for their utilization as units of information storage. It provides a robust counter to the material defects as well [69, 70]. Further, to displace the skyrmions, much lower current densities (by order of two) are required compared to the domain walls [2]. Typically, the diameter of a skyrmion ranges from a few hundred nanometers to a few nanometers. Recently, an atomistic size skyrmion configuration has also been reported [71]. Hence, the properties mentioned above and the possibility of stabilizing them at room-temperatures [4–6, 72, 73] have provided a great impetus to the study of magnetic skyrmions from both fundamental physics and device application points of view.

The possibility of utilizing skyrmion to further downscale the contemporary CMOS technology to keep up with Moore’s law has spawned the field of Skyrmion-Electronics or Skyrmionics. As the name suggests, the field aims to integrate skyrmions into contemporary microprocessors, random access memories, and RF applications. Fert et al. [7] proposed in 2013 the use of skyrmions as a unit of information in a novel racetrack memory. As mentioned in the previous paragraph, the most significant improvements were the reduced size of the skyrmions, their topological stability and relatively small current densities required to displace them. Skyrmions have also found application in spin-torque nano-oscillator (STNO) devices [8, 9]. In a nano-disc geometry, the skyrmions gyrate with the help of a spin-polarized current through the STT effect. As the skyrmions behave as rigid quasi-particles, their arrangement in the disc can enable one to tailor a complex periodic signal. Zang et al. [10–12], in 2015, with two separate

publications, proposed the use of skyrmions in both logic gate devices and transistor type devices. The logic gate device is based on the conversion of skyrmions into domain walls and vice-versa by modulating the width of skyrmion propagation channel, while the skyrmion based transistor uses a voltage-controlled perpendicular magnetic anisotropy to create a potential barrier for the skyrmion propagation, and hence, a gate ON and a gate OFF state. Finally, skyrmions have shown promise in unconventional computing, such as neuromorphic devices, reservoir computing, and stochastic computing [13]. There are still significant challenges related to understanding the properties of the materials hosting the skyrmions and skyrmion's intrinsic characteristics for a comprehensive integration into new devices; however, the results obtained from different theoretical and experimental studies of skyrmions remain quite encouraging.

Due to ease of fabrication and characterization, most of the material geometries considered until recently in the study of nanomagnetism and spintronics have been 2D. However, with the advances in experimentation and simulation techniques, it has become possible to explore complex 3D geometries at nanoscopic scales, which has piqued the magnetism community's interest. We refer to a recent review [14] on the subject, which thoroughly describes these advances. On the fabrication side, this change is primarily driven by the development of techniques like focused electron beam induced deposition (FEBID) [74], physical vapor deposition (PVD) on 3D scaffolds [75], and chemical methods [76, 77]. Characterization techniques such as nano-SQUID and magneto-optical Kerr effect (MOKE) with micromanipulation have proved useful [78, 79]. The highly ordered magnetization configuration of multiple nano-objects can also be characterized through neutron small-angle scattering experiments by utilizing the reciprocal space. This technique was utilized for the first observation of an ordered skyrmion crystal phase in MnSi [1]. In the field of microscopy, the use of nano-tomography [80] has shown promise. The 3D magnetization configuration can be constructed through multiple 2D projections of the geometry by rotating it with respect to an axis. Concerning the X-ray microscopy, where one can also study the magnetization dynamics, transmission-X-ray photoemission electron microscopy (XPEEM) [81, 82] and magnetic X-ray tomography [83] have been used to study 3D nanoscopic geometries.

Given the progress in characterization and microscopy techniques to study 3D nanomagnetism, micromagnetic simulations remain a powerful tool for an in-depth understanding of static and dynamic properties of magnetization configuration in the

geometry. Most often, the strategy to study the 3D magnetization configuration is to compare its 2D projections, obtained from the characterization or the microscopy techniques, with the corresponding micromagnetic simulations. The progress in computer hardware and code development has boosted the field of simulations immensely. It has become possible to simulate micron-sized geometries with a personal computer, which used to require dedicated computational facilities up to a few years ago. The use of graphical processing units (GPUs) for massively parallel computations has further improved the time required for the calculations. The generation of large amount of data in a short time due to improved computational speed has lead to new challenges, such as, visualization, post-processing, and storage of the data. Further, the development of hybrid micromagnetic and atomistic simulation techniques [84] for studying strongly inhomogeneous magnetization configurations such as a Bloch point has made possible a more general and universal treatment of different magnetic materials. The simulations require the geometry to be spatially discretized. The finite element method (FEM) has proved significant for the discretization of 3D shapes. As FEM uses an irregular mesh, it is advantageous in modeling complex 3D geometries containing curvatures, compared to the finite difference method (FDM), which uses a regular mesh. Considering the progress in the field of micromagnetic simulations, as mentioned above, it has moved past the point where researchers would only use it as an interpretation tool for different magnetization related phenomena. It has now emerged as an effective and robust tool for predicting different static and dynamic magnetization phenomena.

Following the general trend in nanomagnetism, most reported studies on magnetic skyrmions are based on essentially 2D material geometries, where interfacial DMI stabilizes the skyrmions. The research on 2D geometries and interfacial DMI has been motivated by the possibility of utilizing already mature fabrication, characterization, microscopy, and simulation techniques. However, keeping in mind the recent progress of the respective fields, as mentioned in the preceding paragraphs, it is possible to explore the properties of 3D magnetic skyrmions in 3D nanoscopic geometries. In the studies presented in this thesis, we explore the static and dynamic properties of skyrmions stabilized by bulk DMI in nanoscopic 3D material geometries with the help of FEM/BEM micromagnetic simulations. We use the material parameters corresponding to the well studied FeGe, a non-centrosymmetric ferromagnetic material lacking inherent spatial inversion symmetry, and hence, exhibiting bulk DMI, which in turn stabilizes 3D Bloch

type skyrmions. For a fundamental 3D material geometry like a nanosphere, we find a variety of equilibrium magnetization states, in addition to the skyrmion state, such as a helical, meron, and chiral bobber state. Moreover, we find that the geometry of the material plays a crucial role in the stabilization of the skyrmions, based on which we propose a method to confine them to a desired region of the geometry by introducing thickness modulations. We present a full study on statics and dynamics of the confined skyrmions showing the method to confine them and their dynamic response when confined. Finally, we motivate the possible use of these properties in device applications, such as a novel racetrack memory and RF applications.

The thesis is broadly divided into three parts. The first part describes the theory of micromagnetism and 3D magnetic skyrmions in two separate chapters. The theory of micromagnetism, which constitutes **chapter 2**, forms the underlying theory of different interactions and energy terms required to simulate a ferromagnetic material lacking inherent spatial inversion symmetry (FeGe in our case). As the micromagnetic theory considers magnetization a continuous vector field, the description of the interactions differs from the atomistic picture (Heisenberg model). In particular, we present the micromagnetic description of exchange, bulk Dzyaloshinskii-Moriya (DMI), Zeeman, and dipolar interactions. Further, we describe the utilization of the Landau-Lifshitz-Gilbert (LLG) equation for studying the magnetization dynamics and its modification to accommodate spin-transfer torque (STT) effects. Finally, we present the description of relevant magnetic length scales, and briefly discuss other significant magnetization structures such as magnetic domains and domain walls.

Chapter 3 outlines the analytical treatment of 3D magnetic skyrmions, their crucial theoretical and experimental studies, and a collection of similar chiral magnetization structures. The analytical treatment of skyrmions is further subdivided into two parts : first, the static skyrmion solution stabilized by DMI, and second, the interaction of conduction electrons with the skyrmions, which contains topological Hall effect, skyrmion Hall effect, Thiele equation, and emergent magnetic and electric field in the presence of skyrmions. As they have gathered considerable attention from the spintronics community in the last few years, a vast pool of studies is present in the literature. Considering the scope of this thesis, we present a short list of seminal works on 3D skyrmions. It includes studies on their observation, motion under spin-polarized current, and dynamical magnetization modes. Finally, we recount chiral magnetization struc-

tures, such as magnetic vortex, Bloch point, helical magnetization state, chiral bobber state, dipole strings, and magnetic hopfions, which have attracted attention from the community due to their unique topology and magnetic properties.

The second part contains the numerical methods used for the implementation of micromagnetic simulations. **Chapter 4** outlines the theory of numerical implementation, i.e., spatial discretization in the form of the finite element method (FEM) and temporal discretization for integrating the LLG equation on FEM mesh nodes at discrete time steps. Spatial discretization with the FEM method is vital for our study as the use of irregular mesh helps us model three-dimensional geometries better. However, it is not trivial to evaluate the total effective field generated due to material interactions on an irregular mesh, which is used further for LLG integration. The section on FEM starts with a summary of simplex elements that form the basis of an irregular mesh. Then, we discuss the use of shape functions for piecewise linear interpolation of any arbitrary function, their differentiation, and integration. Finally, we discuss the solution of partial differential equations to evaluate the local effective exchange field and long-range magnetostatic field. These subsections introduce the essential concept of weak formulation of partial differential equations such as Laplace's equations and Poisson's equation. The proceeding section, related to temporal discretization, outlines the numerical integration of the LLG equation utilizing the total effective field calculated in the previous section. Finally, we present a short description of `tetmag` code, which is used as a numerical instrument for the FEM/BEM micromagnetic simulations.

Part three contains the main results obtained through our studies on 3D skyrmions, divided into chapters 5-7. **Chapter 5** describes the three-dimensional chiral magnetization structures obtained in FeGe nanospheres focusing on five principal equilibrium magnetization states : helical, meron, skyrmion, chiral bobber, and quasi-saturation. We describe the magnetization configuration of each equilibrium state in detail and schematically show the change in state with increasing external magnetic field. Thus, we obtain a phase diagram of the ground states by changing the external magnetic field strength and radius. The phase diagram depicts the dependence of equilibrium state stability on the dimensions of the material geometry. Further, we obtain a cross-section of the phase diagram in the form of two line-scans, one along the direction of constant radius and another along the constant external field, to show the total energy density of the ground states and metastable equilibrium states. We find that the total energy

of ground state and metastable equilibrium states is close for specific phase diagram regions. However, due to complex magnetization topology, a transition from one state to another are often separated by a significant energy barrier. This finding could be of interest to magnetic recording device applications. Finally, we explore the role of magnetostatic interactions by plotting the demagnetization energy as a percentage of total energy for the ground states. We find that it stays below 10% for all the ground states, and the phase diagram does not alter if one neglects the magnetostatic interactions.

Chapter 6 outlines the skyrmion-chiral bobber transition obtained in a nanodisc geometry. Recently, the two states have been proposed as the units of information storage with distinct magneto-transport fingerprints. Hence, the possibility to dynamically switch between the two states could be relevant from a memory device application point of view. In chapter 5, we describe how a state becomes energetically preferable depends on the strength of the external magnetic field. Utilizing this concept, we propose a method to switch between the magnetization states with the help of an external field pulse.

Chapter 7 describes the geometric confinement of 3D skyrmions through material thickness modulations. While chapter 6 outlines the concept of energetically preferable skyrmion state on the external magnetic field, this chapter explores the dependence of skyrmion state stability on the material's dimensions. The first section of the chapter focuses on static skyrmion confinement in a rectangular geometry. We acknowledge that if all three dimensions of the geometry are on a nanoscopic scale, the phase diagram representing the magnetization ground states depends heavily on those dimensions. Hence, we plot a phase diagram to obtain the ground states for the rectangular geometry by keeping lateral dimensions constant and changing the thickness and external field. Typically, we find that the skyrmion state is more stable in thinner rectangular films at a given external field, confirmed by a percentage DMI energy plot of ground states. Finally, based on the phase diagram, we present static skyrmion confinement in the regions of reduced film thickness of circular pocket and thin path shape. The next two sections focus on calculating the energy barrier profile (skyrmion potential well) faced by an isolated skyrmion in the linear path geometry (one of the example geometry). First, we mathematically model the magnetization profile of an isolated Bloch type skyrmion. Then, we use the modeled magnetization configuration to calculate the system's total energy as the skyrmion moves across the thickness barrier. We repeat the

process for a rectangular film without the thickness barrier and compare both energy profiles. As expected, we find a much higher energy barrier in the presence of thickness modulation. Finally, the last section outlines the dynamics of confined skyrmion. In the first subsection, we propose a novel *H-shaped* skyrmion racetrack geometry, with thickness barriers at the edges to counter the unwanted skyrmion Hall effect (SHE). We find that the maximum current density that can drive the skyrmions in the racetrack increases by eight folds with the thickness barriers' introduction. In the final subsection, we study the dynamical modes obtained in a disc geometry with a thickness barrier at the edge. The skyrmion is stabilized in the thin central part of the disk. First, we identify all the magnetization modes and then calculate the dependence of these modes' frequency and amplitude on the thickness barrier's changing width. We find a collection of breathing, gyrotropic, and azimuthal modes within the 50 GHz range. Moreover, we find that one can tune the frequencies and amplitude of these modes by adjusting the thickness barrier's width. Hence, in summary, we propose a way to confine the 3D skyrmions, studied their dynamic properties, and motivated device applications.

Première partie

Theory

CHAPITRE 2

Micromagnetism

W.F. Brown Jr. introduced micromagnetic theory [16] in 1963 to describe magnetization structures of the sub-micrometer length scale in magnetic materials. The length scales considered are large enough for the atomic structure of the material to be ignored (the continuum approximation) and yet small enough to resolve magnetic structures such as a domain wall, a vortex, or in our case, a magnetic skyrmion. It allows not only to calculate these magnetization structures but also predicts their existence. In contrast to purely quantum mechanical theories, such as density functional theory, micromagnetics does not account for the electronic structure of the material and the origin of the magnetic moment. Instead, it uses the magnetization as a material parameter, which is defined as the density of magnetic moments. The purpose of micromagnetic theory is to determine the spatial structure of the magnetization on a mesoscopic scale, as well as its evolution in time. The model's central assumption is that the aligning forces in the magnetic material are strong enough to keep the magnetization parallel on a characteristic length scale well above the lattice constant. In practice, this assumption is justified by the overwhelmingly dominant effect of the ferromagnetic exchange on short length scales. Exceptions in which this assumption does not hold, in a bulk ferromagnet, are rare (for *e.g.*, Bloch points). The total energy of a ferromagnetic system depends on the arrangement of the magnetization, and it is composed of several contributions depending on the respective material's properties. While some of these contributions, like the demagnetization energy and the Zeeman energy, can be described by classical magnetostatics, others like the exchange energy, DMI, and the magnetocrystalline anisotropy energy have a quantum mechanical origin.

The dynamics of the magnetization was described by Landau and Lifshitz [85]. Later, Gilbert [17] derived an equivalent description using a different damping formulation. The resulting Landau-Lifshitz-Gilbert equation describes the evolution of the magnetization in time, including dynamic effects such as spin waves, normal oscillatory modes of the magnetization, and magnetization reversal processes. Thus, micromagnetic theory is a fundamental tool for the investigation of the structure and dynamic behavior of nanoscale systems.

In this chapter, we present the fundamental aspects of the micromagnetic theory. We start by describing the terms involved in calculating the total energy, which are used for our study, and the effective field resulting from the respective energy terms. Also, we present the Landau-Lifshitz-Gilbert (LLG) equation which takes into account the total

effective field, due to the energy contributions, which acts on the local magnetization by exerting a torque. Further, we discuss the extension of LLG equation for the spin-polarized currents.

2.1 Energy terms

In micromagnetism, the magnetization is represented by a continuous directional vector field $\mathbf{M}(\mathbf{x})$, meaning that it has a constant length M_s , where M_s is the saturation magnetization of the material. Often, the reduced magnetization is used, defined as $\mathbf{m}(\mathbf{x}) = \mathbf{M}(\mathbf{x})/M_s$ as representing the vector field. The micromagnetic problem thus consists in determining the direction of $\mathbf{m}(\mathbf{x})$ at each position \mathbf{x} . For static configurations, one can achieve this by minimizing the free energy of the system. We describe all the contributions to the free energy in this section which are used in our study. As is commonly done in micromagnetic theory, we neglect the entropy contribution in our study, which is a good approximation of temperatures far below the Curie point.

2.1.1 Exchange energy

The characteristic property of ferromagnetic materials is, typically, a non-vanishing macroscopic magnetization, even for a vanishing external field. From an atomistic point of view, if the magnetic moments are coupled exclusively by their dipole-dipole interaction, the resulting magnetization always vanishes for a vanishing external field. However, in ferromagnetic materials, the magnetic moments are subjected to symmetric exchange interaction arising from a quantum mechanical interaction of electrons. This effect energetically favors either their parallel or antiparallel alignment. One can attribute the origin of the energy contribution to the respective two-particle system's Coulomb energy.

The Heisenberg model gives the classical description of the exchange interaction which holds on an atomistic level. A detailed derivation of the same can be found in reference [86]. In Heisenberg formulation, the exchange energy of two neighboring magnetic moments \mathbf{s}_i and \mathbf{s}_j is defined as

$$E_{ij}^{ex} = -J_{ij} \mathbf{s}_i \cdot \mathbf{s}_j \quad (2.1)$$

Where, J_{ij} denotes the exchange integral for the respective magnetic moments. The exchange integral J_{ij} depends on the distance of magnetic moment sites. Hence, nearby moments provide significant contributions to the exchange energy, usually next neighbors. Performing a transition to the continuum representation, $\Delta\mathbf{x}$ is introduced as a small parameter describing the inter-atomic distance. Considering a continuous normalized magnetization field $\mathbf{m}(\mathbf{x}) = \mathbf{M}(\mathbf{x})/M_s$, where M_s is the saturation magnetization of the material, the exchange energy associated with coupling of magnetization at position \mathbf{x} is given by [87]

$$E_x^{ex} = -\frac{J}{2}\mathbf{m}(\mathbf{x}) \cdot \mathbf{m}(\mathbf{x} + \Delta\mathbf{x}) \quad (2.2)$$

$$= -\frac{J}{2}\left[1 - \frac{1}{2}\left(\nabla\mathbf{m}^T \cdot \Delta\mathbf{x}\right)^2\right] + \mathcal{O}(\Delta\mathbf{x}_i^3) \quad (2.3)$$

One can obtain the expression 2.2 by applying the unit-vector identity $(\mathbf{n1} - \mathbf{n2})^2 = 2 - 2\mathbf{n1} \cdot \mathbf{n2}$ and performing a Taylor expansion of the vector field. We neglect the higher-order terms of the Taylor expansion represented by \mathcal{O} . Finally, one may integrate equation 2.2 to obtain a continuous expression for the total exchange energy while considering a regular spin-lattice, i.e., regular spacing of the spin sites $\Delta\mathbf{x}$ as well as identical J for each site. In the most general form, the procedure results in the following equation [87]

$$E^{ex} = C + \int_{\Omega_m} \sum_{i,j=1}^3 A_{ij} \frac{\partial m}{\partial x_i} \frac{\partial m}{\partial x_j} d\mathbf{x} \quad (2.4)$$

The coefficients of the matrix A_{ij} depend on the crystal structure and the resulting exchange couplings of the magnetic body's moments. C is a constant of the integration, and it is usually neglected since it is independent of \mathbf{m} and a constant offset to the total energy. For cubic and isotropic lattice structures, the exchange coupling constants A_{ij} simplify to the scalar ferromagnetic exchange constant A .

$$E^{ex} = \int_{\Omega_m} A \sum_{i=1}^3 \left(\frac{\partial \mathbf{m}}{\partial x_i}\right)^2 d\mathbf{x} \quad (2.5)$$

Even though the energy expression is derived with specific lattice structure assumptions, it accurately describes many magnetic materials [88]. One can argue that

equation 2.5 exactly represents the lowest order phenomenological energy expression that penalizes inhomogeneous magnetization configurations.

2.1.2 Dzyaloshinskii-Moriya interaction

Dzyaloshinskii [89] and Moriya [90] discovered that neighboring spins could interact through an antisymmetric exchange interaction in addition to the regular symmetric exchange interaction discussed in Section 2.1.1. Hence, it is referred to as the Dzyaloshinskii-Moriya interaction (DMI). It is a superexchange interaction caused by strong spin-orbit coupling in material systems lacking spatial inversion symmetry. In Heisenberg formalism, one can write the general antisymmetric exchange energy of neighboring atomistic magnetic moments \mathbf{s}_i and \mathbf{s}_j as

$$E_{ij}^{DMI} = \mathbf{d}_{ij} \cdot (\mathbf{s}_i \times \mathbf{s}_j) \quad (2.6)$$

Here, the vector \mathbf{d}_{ij} depends on the symmetry of the system. For this study, we are interested in materials that inherently lack spatial inversion symmetry, known as non-centrosymmetric ferromagnets [23, 91]. For these materials, one can represent the vector \mathbf{d}_{ij} as

$$\mathbf{d}_{ij} = -d\Delta\hat{\mathbf{x}} \quad (2.7)$$

Where, d is a scalar DMI coupling constant, and $\Delta\hat{\mathbf{x}} = \Delta\mathbf{x}/|\Delta\mathbf{x}|$ is a unit vector pointing from the atomic site i to atomic site j . With the help of equation 2.7, for a continuous normalized magnetization vector field $\mathbf{m}(\mathbf{x})$, one can write the energy term $E_{\mathbf{x}}^{DMI}$ at position \mathbf{x} as [87]

$$E_{\mathbf{x}}^{DMI} = -\frac{d}{2}\Delta\hat{\mathbf{x}} [\mathbf{m}(\mathbf{x}) \times \mathbf{m}(\mathbf{x} + \Delta\mathbf{x})] \quad (2.8)$$

$$= -\frac{d}{2}\Delta\hat{\mathbf{x}} [\mathbf{m}(\mathbf{x}) \times (\nabla\mathbf{m}^T \Delta\mathbf{x})]. \quad (2.9)$$

Similar to section 2.1.1, assuming isotropic DMI coupling d and lattice spacing $\Delta\mathbf{x}$ results in the energy's continuous formulation as follows.

$$E^{DMI} = \int_{\Omega_m} D\mathbf{m} \cdot (\nabla \times \mathbf{m})d\mathbf{x} \quad (2.10)$$

The coupling constant D depends on the atomistic coupling constants d and the lattice spacing $\Delta\mathbf{x}$.

Generally, in micromagnetism, the total energy contribution of DMI can be elegantly expressed through a phenomenological approach based on Lifshitz invariants (LIs). The LIs are derived from general considerations of the properties of the thermodynamic potential in second-order phase transitions. Their detailed form depends on the symmetry properties of the crystal [92, 93].

$$\mathcal{L}_{ij}^k = m_i \frac{\partial m_j}{\partial k} - m_j \frac{\partial m_i}{\partial k} \quad (2.11)$$

where $i, j, k \in \{x, y, z\}$. Further, one may express E^{DMI} for the bulk in terms of Lifshitz invariants as :

$$E^{DMI} = \int_{\Omega_m} D(\mathcal{L}_{zy}^x + \mathcal{L}_{xz}^y + \mathcal{L}_{yx}^z) d\mathbf{x} = \int_{\Omega_m} D\mathbf{m} \cdot (\nabla \times \mathbf{m}) d\mathbf{x} \quad (2.12)$$

The antisymmetric exchange interaction competes with the symmetric (ferromagnetic) exchange interaction in ferromagnets to give chiral magnetization configuration, such as spin helical states or magnetic skyrmion states, which we will discuss in section 5.1.

2.1.3 Demagnetization energy

The demagnetization energy, also known as magnetostatic energy or stray-field energy, considers the dipole-dipole interaction of a magnetic system. This energy contribution owes its name to the property of magnetic systems, which energetically favors macroscopically demagnetized states if subject to dipole-dipole interaction alone. For a continuous magnetization, the demagnetization energy can be obtained from Maxwell's equations. In the absence of an electric current, Maxwell's macroscopic equations give

$$\nabla \cdot \mathbf{B} = 0 \quad (2.13)$$

$$\nabla \times \mathbf{H}^{dem} = 0 \quad (2.14)$$

Further, one can express the magnetic flux \mathbf{B} in the form of \mathbf{H}^{dem} and \mathbf{M} as follows.

$$\mathbf{B} = \mu_0(\mathbf{H}^{dem} + \mathbf{M}) \quad (2.15)$$

It can be followed from the equation 2.13 that the magnetic field \mathbf{H}^{dem} is conservative, and hence one can express it in terms of a scalar potential $\mathbf{H}^{dem} = -\nabla u$. Inserting the scalar potential and equation 2.15 in equation 2.13, we obtain the Poisson equation.

$$\Delta u = \nabla \cdot \mathbf{M} \quad (2.16)$$

The solution of the Poisson equation has the following form.

$$u(\mathbf{x}) = -\frac{1}{4\pi} \left[\int_{\Omega_m} \frac{\nabla' \cdot \mathbf{M}(\mathbf{x}')}{|\mathbf{x} - \mathbf{x}'|} d\mathbf{x}' - \int_{\partial\Omega_m} \frac{\mathbf{M}(\mathbf{x}') \cdot \mathbf{n}}{|\mathbf{x} - \mathbf{x}'|} ds' \right] \quad (2.17)$$

Here, ds' measures the surface area of the boundary of \mathbf{x}' and \mathbf{n} is a outward-normal vector to the surface. In analogy to the electric field, the terms $\rho = -\nabla \cdot \mathbf{M}$ and $\sigma = \mathbf{M} \cdot \mathbf{n}$ are often referred to as magnetic volume charges and magnetic surface charges, respectively. Once we obtain the scalar potential, we can solve for the demagnetization field. Thus, one may write the demagnetization energy as follows.

$$E^{dem} = -\frac{\mu_0}{2} \int_{\Omega_t} \mathbf{M} \cdot \mathbf{H}^{dem} d\mathbf{x} \quad (2.18)$$

The factor of 1/2 in the above equation is typical for self-energy terms. It is required in order to account for the *double-counting* problem that arises from the fact that magnetic moments within the sample are both the source of magnetostatic fields and subjected to them. On an atomistic scale, the dipolar interaction between a magnetic moment at a site i and another moment at a site j should only be counted once. In the integration of the volume in the continuum model, this is accounted for by the factor 1/2. The equation 2.17 highlights two essential properties of magnetostatic energy. First, the total magnetostatic energy of a ferromagnetic body is always positive [94]. Second, it is essential to look at the magnetic volume and surface charges as magnetic potential sources. Hence, a stable magnetization configuration tends to minimize these charges' formation to minimize the magnetostatic energy. The magnetization will align

with the boundaries such that $\mathbf{M} \cdot \mathbf{n}$ tends to zero; minimizing $\nabla \cdot \mathbf{M}$ to an extent possible. This is known as the *pole avoidance principle* [94]. The consequence of this principle is the formation of closure domain configurations in magnetic systems above a critical size [95].

2.1.4 Zeeman energy

The energy of a ferromagnetic body depends on the external field. The corresponding energy contribution is referred to as Zeeman energy. It is dependent on the relative orientation of the magnetization to the external magnetic field. According to classical electromagnetics, one can write the expression of Zeeman energy as follows.

$$E^{Zee} = -\mu_0 \int_{\Omega_m} M_s \mathbf{m} \cdot \mathbf{H}^{ext} d\mathbf{x} \quad (2.19)$$

Here, μ_0 is the vacuum permeability and \mathbf{H}^{ext} is the external magnetic field.

2.1.5 Effective field

We have introduced different energy terms involved in the micromagnetic formalism of an isotropic non-centrosymmetric ferromagnet, summarized as follows.

$$E^{total} = E^{exc} + E^{DMI} + E^{dmg} + E^{Zee} \quad (2.20)$$

To obtain a magnetization configuration corresponding to a local minimum of total energy, one must address the variational problem of total energy concerning magnetization, mathematically represented by $\delta E^{total} = 0$. Moreover, one also needs to account for the non-linear constraint $|\mathbf{m}| = constant$ imposed by a fundamental assumption of micromagnetism, which conserves the absolute value of magnetization in space and time.

In a non-equilibrium magnetic configuration, the magnetization undergoes a precessional motion around an effective field before relaxing along its direction. One can calculate the contribution of the external magnetic field and demagnetization field to this effective field from Maxwell's equations. However, exchange interaction and DMI contributions need to be constructed from thermodynamic principles. W. F. Brown Jr. introduced the effective field as a variation of energy functional with the magnetization.

$$\mathbf{H}_{eff} = -\frac{1}{\mu_0 M_s} \frac{\delta E[\mathbf{m}]}{\delta \mathbf{m}} \quad (2.21)$$

Here E is the total energy functional from equation 2.20. Hence, we can write different contributions to the effective field from all the different energy terms discussed in section 2.1 as

$$\mathbf{H}_{eff} = \underbrace{\frac{2A}{\mu_0 M_s} \nabla^2 \mathbf{m}}_{Exchange} - \underbrace{\frac{2D}{\mu_0 M_s} (\nabla \times \mathbf{m})}_{DMI} + \mathbf{H}_{dmg} + \mathbf{H}_{ext} \quad (2.22)$$

Where A is exchange stiffness constant and D is DMI constant.

2.2 Dynamics of magnetization

In micromagnetics, the magnetization dynamics is described by the Landau-Lifshitz-Gilbert (LLG) equation. This equation describes the spatially resolved motion of the vector field of the magnetization in an effective field. One obtains the equilibrium magnetization configuration by determining when the torque exerted by the effective field vanishes.

2.2.1 Landau-Lifshitz-Gilbert equation

We consider a homogenous effective field \mathbf{H}_{eff} exerting a torque $\boldsymbol{\tau}$ on the magnetization \mathbf{M} .

$$\boldsymbol{\tau} = \frac{d\mathbf{L}}{dt} = \mathbf{M} \times \mathbf{H}_{eff} \quad (2.23)$$

Where \mathbf{L} is the angular momentum of the magnetization expressed as

$$\mathbf{L} = -\frac{\mathbf{M}}{\gamma_0} \quad (2.24)$$

Here, γ_0 is the gyromagnetic ratio, given by $\gamma_0 = \frac{g|e|\mu_0}{2m}$, where e is the electron charge and m is the electron mass. The Landé g -factor [96] is 2 when the moment is

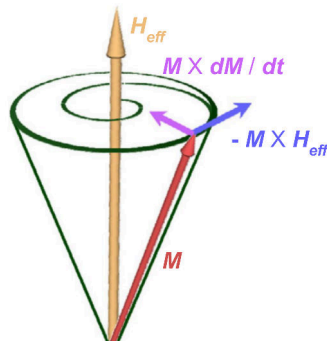


FIGURE 2.1 – Schematic representation of the magnetization precession around the effective field according to the LLG equation (equation 2.26) with the precession term shown in red and relaxation term shown in blue.

purely due to the electron spin. In most ferromagnetic materials, g is 2, indicating that the orbital contribution to the magnetic moment is negligible [88]. The change of the magnetization in time is then related to the torque by

$$\frac{d\mathbf{M}}{dt} = -\gamma_0 \boldsymbol{\tau} = -\gamma_0 [\mathbf{M} \times \mathbf{H}_{eff}] \quad (2.25)$$

In addition to the precession, dissipative processes damp the motion of the magnetization. On the atomic scale, these are attributable to spin diffusion, spin-orbit coupling, interactions with magnons or phonons, or misaligned atomic spins. Such dissipative processes can be accounted for within micromagnetic theory by introducing a phenomenological damping term. In the case of the Gilbert [17] equation (2.26), the damping is proportional to the rate of change of the magnetization $\frac{d\mathbf{M}}{dt}$.

$$\frac{d\mathbf{M}}{dt} = -\gamma_0 (\mathbf{M} \times \mathbf{H}_{eff}) + \frac{\alpha}{M_s} \left(\mathbf{M} \times \frac{d\mathbf{M}}{dt} \right) \quad (2.26)$$

Typically, α is considered constant. Its theoretical determination is a rather complex problem [97] since it encompasses effects from many different sources. In the equation 2.26, the time derivative of the magnetization is present on both sides of the equation. One can transform it by replacing $\frac{d\mathbf{M}}{dt}$ on the right-hand-side. Thus, we obtain the following representation after rearrangement.

$$\frac{d\mathbf{M}}{dt} = -\gamma' [\mathbf{M} \times \mathbf{H}_{eff}] - \frac{\alpha'}{M_s} \mathbf{M} \times [\mathbf{M} \times \mathbf{H}_{eff}] \quad (2.27)$$

where γ' and α' are defined as

$$\gamma' = \frac{\gamma_0}{1 + \alpha^2} \quad (2.28)$$

$$\alpha' = \frac{\alpha\gamma_0}{1 + \alpha^2} \quad (2.29)$$

One can visualize the evolution of magnetization according to Fig. 2.1. There are two terms involved : the precession term is perpendicular to the magnetization and the effective field, while the damping term is perpendicular to the magnetization and the precession term, which aligns the magnetization toward the effective field. Both terms preserve the norm of the magnetization. In a numerical context, the Landau-Lifshitz form of the equation of motion (equation 2.27) has the advantage because it is explicit, while the mathematically equivalent Gilbert form (equation 2.26) is implicit. The explicit form allows for the ease of computation of the right-hand-side of the equation.

2.2.2 Current induced dynamics

Moving charges in a ferromagnet can induce a magnetic field (Oersted field), which can, in turn, influence the state of the magnetization. Besides this traditional interaction between electrical currents and the magnetization, given by the induced magnetic field (which enters in the LLG equation in the form of an effective Zeeman field), Slonczewski and Berger [66, 67] have predicted that a spin-polarized electric current can also directly influence the magnetization. As the current flows through a ferromagnet, the local magnetization exerts a torque on the spins of the conduction electrons, consequently aligning them with the magnetization direction. In turn, the spins exert a reaction torque on the magnetization, which is proportional to the current density known as spin-transfer torque (STT). This torque causes the displacement of the magnetic structure. Because the electron dynamics is much faster than that of the magnetization, the spins of conduction electrons generally align with the local magnetization, leading to an adiabatic spin torque. Deviations from this process are also possible, mainly when

the electron spins cannot adapt to the local magnetization, for example, in narrow inhomogeneous magnetic structures.

In this study, we use the effects of spin-polarized currents flowing in the sample to displace magnetic skyrmions. Experiments show that skyrmions move under the influence of relatively small spin-polarized current densities compared to domain walls [2]. This is one of the characteristics that led to the proposition of using skyrmion as a fundamental unit of information in nonvolatile memory devices, like race-track memory [7].

One can account for the STT effect with the addition of two additional terms to the Gilbert's equation. According to Zhang and Li [98], the LLG equation takes the form :

$$\begin{aligned} \frac{d\mathbf{M}}{dt} = & -\gamma_0 [\mathbf{M} \times \mathbf{H}_{eff}] + \frac{\alpha}{M_s} \mathbf{M} \times \left[\mathbf{M} \times \frac{d\mathbf{M}}{dt} \right] \\ & - \frac{1}{M_s^2} \mathbf{M} \times [\mathbf{M} \times (\mathbf{u} \cdot \nabla) \mathbf{M}] \\ & - \frac{\beta}{M_s} \mathbf{M} \times (\mathbf{u} \cdot \nabla) \mathbf{M} \end{aligned} \quad (2.30)$$

Here, \mathbf{u} stands for :

$$\mathbf{u} = \frac{JPg\mu_B}{2eM_s} \cdot \mathbf{j}_e \quad (2.31)$$

Further, J is the current density, \mathbf{j}_e is its direction of the electron flow, P is the degree of polarization, μ_B the Bohr magneton, g is the Landé g-factor, and e the electron charge. The expression for \mathbf{u} has the units of m/s, which one can interpret as the electron spins' velocity. The first additional term to Gilbert's equation describes the adiabatic spin torque. The second term accounts for the non-adiabatic processes, and one can quantify it by the dimensionless parameter β , also called the degree of non-adiabaticity. Its specific form differs in Gilbert and the LLG equation. If written in the explicit LLG equation, the factor β is present in both additional terms [99].

2.3 Magnetic structures

2.3.1 Characteristic lengths

The fundamental assumption of micromagnetism is a continuous and smooth change of magnetization in the magnetic material. The assumption is well-founded as the ferromagnetic exchange interactions forbid any abrupt change in magnetization over a length

comparable to the interatomic distance. While the ferromagnetic exchange preserves a nearly parallel alignment of magnetic moments on an atomistic length scale, other micromagnetic terms can lead to inhomogeneities of the magnetization on larger length scales. The exchange length describes the outcome of such competing interactions and it can be interpreted as the typical length scale on which magnetic inhomogeneities can unfold. The exchange lengths are derived from analytic calculations of one-dimensional, ideal domain wall profiles. Nevertheless, they also serve as useful estimate for the typical size of other types of inhomogeneities, such as, e.g., magnetic vortices. An exception are Bloch points, which represent topological defects in the magnetization field. At the center of a Bloch point structure, the magnetization direction changes abruptly, on an atomic length scale, by 180° . In bulk materials or extended films, magnetocrystalline anisotropy and ferromagnetic exchange interaction play a dominant role as compared to magnetostatic interactions. Considering a first-order uniaxial anisotropy, one obtains the magnetocrystalline exchange length, also called the Bloch wall parameter.

$$l_K = \sqrt{\frac{A}{K_u}} \quad (2.32)$$

Here, A is exchange stiffness, and K_u is anisotropy constant. In soft-magnetic materials, the ferromagnetic exchange interaction competes primarily with the magnetostatic term, which tends to form flux-closure patterns. The competition between the exchange and demagnetizing energy terms yields the magnetostatic exchange length.

$$l_{exc} = \sqrt{\frac{2A}{\mu_0 M_s^2}} \quad (2.33)$$

Here, again, A is exchange stiffness, and M_s is saturation magnetization. In the present work, we investigate materials (non-centrosymmetric ferromagnets) hosting chiral magnetization structures stabilized by DMI. The competition between symmetric ferromagnetic exchange and anti-symmetric DMI leads to magnetization helix structures in these materials. One full rotation of the magnetization in such helix structures represent a characteristic length scale known as the long-range helical period l_d . In such systems, l_d plays a role that is comparable to the exchange length in ferromagnets. It describes the typical extension or periodicity of spin spirals, skyrmions, and other helical structures. One can write an expression for l_d as follows [100].

$$l_d = 4\pi \frac{A}{|D|} \quad (2.34)$$

Here, A is the exchange stiffness and D is the DMI constant of the material. We present a further discussion of common chiral magnetization structures hosted by these materials in section 3.3.

2.3.2 Magnetic domains and walls

A fundamental property of ferromagnetic materials tend to form differently oriented and homogeneously magnetized regions known as magnetic domains [88]. In the framework of domain theory, the regions separating these domains are planar defects at which the magnetization direction changes abruptly. The concept of magnetic domains was first introduced by Weiss based on the so-called molecular field [101]. Later it has been extended by micromagnetic theory, according to which domain walls possess an internal structure and a finite extension resulting from the interplay of different energy contributions.

In this section, we discuss the two basic types of domain walls in ferromagnetism, namely, the Bloch wall and the Néel wall. The Bloch [102] and the Néel wall [103] can be described analytically with one-dimensional models. The head-to-head or the tail-to-tail domain walls have been the focus of experimental and numerical studies for the past few years, especially in long and thin soft-magnetic strips and elongated samples [104].

Bloch wall

In a bulk ferromagnetic sample with uniaxial anisotropy, the typical domain walls are Bloch walls [88, 102, 105]. One may characterize it by a rotation of the magnetization parallel to the domain wall plane, where the magnetization orientation inside the domains is also parallel to the domain wall plane (Fig. 2.2(b)). This type of rotation is divergence-free, and hence, zero volume magnetic charge. In the limit of an infinitely extended geometry, surface charges are negligible too. In such a situation, an idealized one-dimensional model can be used to describe two magnetic domains in an infinitely extended volume, in which only the interplay between exchange interaction and magnetocrystalline anisotropy defines the domain wall shape.

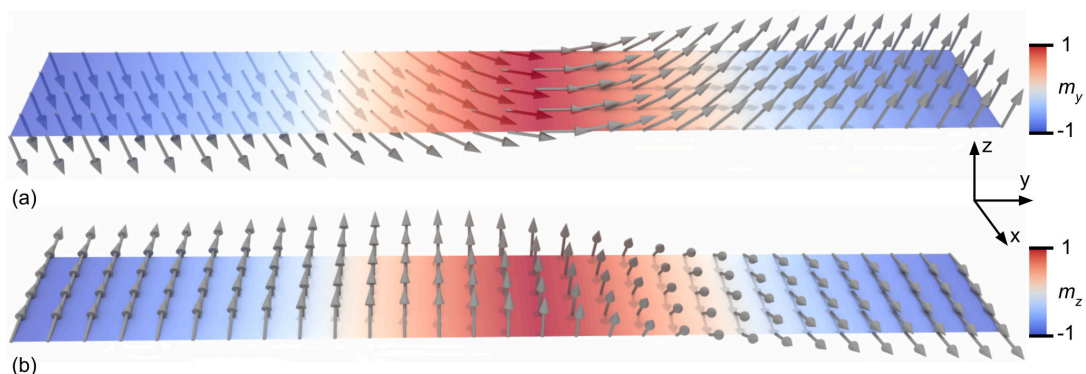


FIGURE 2.2 – (a) Néel domain wall depicting in-plane rotation of magnetization going from one domain to the other, and (b) Bloch wall showing the out of plane rotation of magnetization (parallel to the domain wall plane) going from one domain to the other.

In the case of a first-order uniaxial anisotropy with positive anisotropy constant, one may write an expression for the angle θ between the magnetization and the easy-axis (z -axis in this case) as :

$$\tan\theta = \exp\left(\frac{y}{\sqrt{A/K_u}}\right) \quad (2.35)$$

According to Lilley's definition [106], the Bloch domain wall width is

$$\Delta_{DW} = \pi\sqrt{\frac{A}{K_u}} \quad (2.36)$$

Note that this width is π times the corresponding exchange length.

Néel wall

In section 2.3.2, we neglected the magnetostatic interaction in discussing the magnetization configuration of the domain wall. However, in realistic samples, especially those relevant for device applications, magnetic charges play a significant role. In a one dimensional approximation, where the magnetization direction only depends on the distance from the domain wall center, L . Néel derived in 1953 a domain wall transition in thin films [103]. In the Néel wall, the magnetic structure is determined by the competing exchange and magnetostatic interactions. Néel demonstrated [103] that in thin

films, a domain wall type with an in-plane rotation of the magnetization (Fig. 2.2(a)) has lower energy than the Bloch wall. Thus the expression for theta for the domain wall, in one-dimension (along the y -axis), is given as :

$$\cos\theta = \tanh\left(\frac{y}{\sqrt{2A/\mu_0 M_s^2}}\right) \quad (2.37)$$

Here, θ is defined as the angle that the magnetization subtends with respect to the z -axis. Further, the rotation of magnetization is confined to yz -plane. Like in the case of the Bloch wall, the denominator of tanh on the right side of the equation 2.37 gives the exchange length.

CHAPITRE 3

Magnetic skyrmions

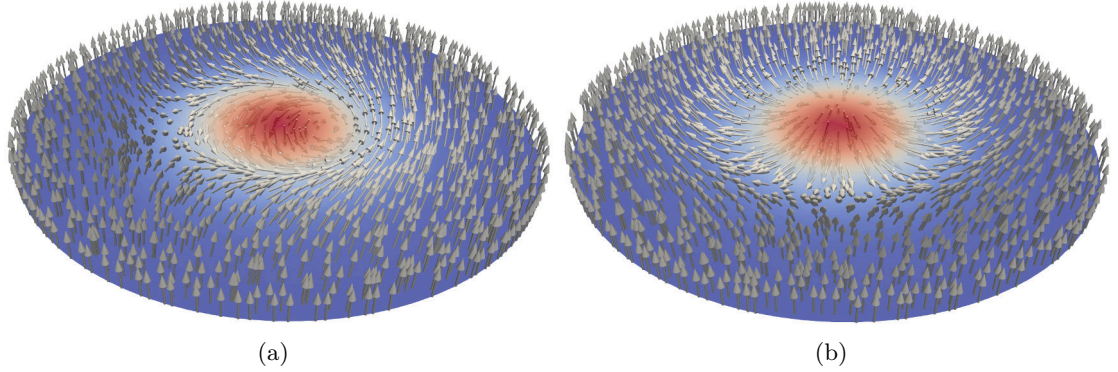


FIGURE 3.1 – Magnetization vector fields of two-dimensional (a) Bloch skyrmion and (b) Néel skyrmion.

Magnetic skyrmions (Fig. 3.1) are topological soliton solutions of the magnetization vector field. The term skyrmion has its origin in the theory of nucleons proposed by Tony Skyrme in 1962 [107, 108]. Since then, many condensed matter branches have adopted the concept of a skyrmion [109–112] to explain different physical phenomena, where ferromagnetic materials are a recent one.

Traditionally, researchers have obtained soliton solutions in nonlinear wave equations [113]. In these wave equations, for a particular case, the nonlinear term essentially cancels out the dispersion term, and hence, yields a wave that retains its shape as it propagates through the medium, almost like a single particle. Unlike a magnetic skyrmion, most of the soliton solutions are obtained in a dynamic case. Hobart-Derrick theorem [114] states that it is impossible to obtain stable localized soliton structures in most condensed matter systems. However, in the case of magnetic skyrmions, the Dzyaloshinskii-Moriya interaction (DMI), an anti-symmetric exchange interaction, prevents its collapse to a magnetic singularity.

DMI is present in magnetic materials that lack spatial inversion symmetry in the lattice structure or interface. It is a three-site exchange interaction mediated between two atoms through a neighboring atom having strong spin-orbit coupling on an atomic scale. Based on chiral symmetry breaking and magnetization configuration obtained in magnetic materials hosting DMI, one can provide a micromagnetic description of DMI in terms of Lifshitz invariants [18, 115].

$$\mathcal{L}_{ij}^k = m_i \frac{\partial m_j}{\partial k} - m_j \frac{\partial m_i}{\partial k} \quad (3.1)$$

Where, $i, j, k \in \{x, y, z\}$ and \mathbf{m} is the unit vector in the direction of magnetization. When included in DMI energy contribution, the above term favors rotational modulation of magnetization in (i, j) -plane and propagation vector along the k -direction. In the case of a non-centrosymmetric ferromagnet (as in the case of studies presented here), the expression for bulk DMI energy density is given as $e_{3D}^{\text{DMI}} = D(\mathcal{L}_{zy}^x + \mathcal{L}_{xz}^y + \mathcal{L}_{yx}^z) = D(\mathbf{m} \cdot (\nabla \times \mathbf{m}))$, where D is the DMI constant. The bulk DMI can form magnetization helices with a propagation direction along all three axes and the rotation plane perpendicular to it (like a Bloch domain wall). Hence, the magnetization configuration of the skyrmion obtained in these materials is known as a Bloch skyrmion. Similarly, in the case of an interface induced DMI, one can write the expression for energy density as $e_{2D}^{\text{DMI}} = D(\mathcal{L}_{xz}^x - \mathcal{L}_{yz}^y)$. Here the magnetization helices propagate in two dimensions, i.e., in xy -plane, with the plane of rotation along the propagation direction (like a Neel domain wall). Hence, the skyrmion configuration obtained in this case is known as a Néel skyrmion.

The magnetization configuration of the skyrmion has a non-trivial topology. It is impossible to continuously unwind a skyrmion to a ferromagnetic configuration without introducing a magnetic singularity (such as a Bloch point) or a discontinuity (material boundary). This unique property of the skyrmions gives them topological stability, which is interesting from both the scientific and application point of view. It is possible to mathematically classify the magnetization configuration based on topology with a skyrmion number. One can express it as :

$$Q = \frac{1}{4\pi} \int \mathbf{m} \cdot \left(\frac{\partial \mathbf{m}}{\partial x} \times \frac{\partial \mathbf{m}}{\partial y} \right) dx dy \quad (3.2)$$

Here, \mathbf{m} is a unit vector field in the magnetization direction of the material. One can understand equation 3.2 as a stereographic projection of the magnetization configuration from a plane to a unit sphere. The skyrmion number of a skyrmion is $|Q| = 1$, which implies that the directions of the magnetization of a skyrmion can wrap the whole sphere once when projected stereographically. Similarly, one can calculate the skyrmion number of other magnetization configurations with non-trivial topologies, such as a magnetic vortex which skyrmion number $|Q| = 1/2$ or a hedgehog Bloch

point with skyrmion number $|Q| = 1$. Recently, Rybakov et al. [116] showed through numerical calculations that it is possible to stabilize magnetization configuration with skyrmion number $|Q| \geq 2$ in materials with non-zero DMI. However, there has been no experimental observation of these magnetization structures.

3.1 Analytic treatment of magnetic skyrmions

3.1.1 Static skyrmion solution

Bogdanov et al. [18–22] obtained an analytical solution for the magnetization configuration of an axisymmetric skyrmion (for example, in xy -plane), which is homogeneous along the perpendicular direction (in the z -direction). The total energy term, which includes contributions from ferromagnetic exchange interaction, DMI, magneto-crystalline anisotropy, magnetostatic interaction, and Zeeman energy, is minimized for the solutions, where the expression for the DMI energy contribution is expressed as a combination of Lifshitz invariants, whose specific form depends on the crystal symmetry. Further, the magnetostatic term is represented as a local term, in the form of an effective anisotropy term, and hence, the solutions are assumed to be axisymmetric [18]. This local magnetostatic field model, which is used to approximate the effect of the long-range dipolar interaction, is helpful for analytic calculations, but it is not always an accurate estimate, especially in flat confined geometries where the geometry’s shape affects the skyrmion configuration. However, the analytical solutions capture the essence of skyrmion configuration to a great extent.

For the analytical description of the magnetization configuration of the skyrmion, the orientation of the magnetization is expressed in polar co-ordinates while the spatial variable is expressed in cylindrical co-ordinates.

$$\mathbf{m}(\mathbf{r}) = m(\sin \theta \cos \psi, \sin \theta \sin \psi, \cos \theta) \quad (3.3)$$

$$\mathbf{r} = r(\rho \cos \phi, \rho \sin \phi, z) \quad (3.4)$$

Thus the axisymmetric solutions obtained by minimizing the total energy of the system is given by $\theta(\rho), \psi(\phi)$. As mentioned above, the expression of DMI energy contribution depends on crystal symmetry, which reflects in the dependence $\psi(\phi)$ of the solutions. The in-plane projection of the five magnetization configurations correspon-

3.1 Analytic treatment of magnetic skyrmions

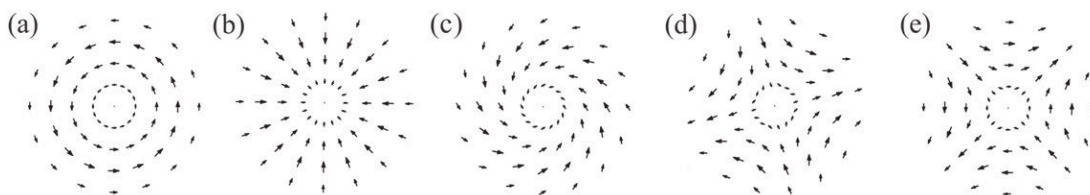


FIGURE 3.2 – The image shows in-plane projections of magnetization in five possible solutions to skyrmion configuration depending on crystal symmetry. The value of $\psi(\phi)$ is mentioned below respective configuration as well as the type of crystal symmetry. Note that in (c) and (d), value of constant ψ_1 depends on the competing DMI, along orthogonal directions, predicted for the respective crystal symmetries. The image is adapted from reference [22].

ding to the different values of $\psi(\phi)$ is shown in Fig. 3.2. After integrating over ϕ in the expression of total energy, one obtains the relationship $\theta(\rho)$ as follows :

$$A \left(\frac{d^2\theta}{d\rho^2} + \frac{1}{\rho} \frac{d\theta}{d\rho} - \frac{1}{\rho^2} \sin\theta \cos\theta \right) - \frac{D}{\rho} \sin^2\theta + f(\theta) = 0 \quad (3.5)$$

The function $f(\theta)$ has no dependence on ρ and represents contribution from magnetocrystalline anisotropy, stray field and external magnetic field. Equation 3.5 can be solved from the boundary conditions $\theta(0) = \pi$ and $\theta(\infty) = 0$ to obtain the full solutions for the magnetization configuration of the skyrmion. It is important to note that equation 3.5 give no stable solution for the skyrmion configuration for $D = 0$.

Out of all the five predicted magnetization configuration for the skyrmion (Fig. 3.2), only three have been observed experimentally up till now, corresponding to Fig 3.2(a), (b) and (e). The first one is the Bloch type skyrmion, corresponding to Fig 3.2(a). These skyrmions are observed in B20-type non-centrosymmetric ferromagnets such as FeGe, MnSi and Cu₂OSeO₃ [1, 23, 24]. The studies presented in this thesis is based on these type of materials ; FeGe to be exact. The second type is the Néel type skyrmions, corresponding to Fig 3.2(b). This type of skyrmion is typically stabilized at the interface of a ferromagnets and a material having strong spin-orbit coupling (such as a heavy metal) for example Fe/Ir interface. The induced DMI due to spatial inversion symmetry breaking at the interface stabilizes the skyrmion. Further, a bulk material known to host Néel skyrmions is GaV₄S₈ [117]. The third configuration is known as an anti-skyrmion,

3.1 Analytic treatment of magnetic skyrmions

corresponding to Fig 3.2(e). This type of skyrmion is observed in Heusler compound with D_{2d} crystal symmetry [118].

3.1.2 Skyrmion in presence of conduction electrons

The interaction of conduction electrons with topologically non-trivial skyrmion magnetization configuration gives rise to interesting transport phenomena. The spin of a conduction electron follows the skyrmion's underlying smoothly varying magnetization. In the process, the electron's spin gains a quantum-mechanical Berry phase [25], which deflects it from the direction of motion along the applied electric field and induces an additional Hall effect contribution known as the topological Hall effect (THE). Similarly, the skyrmions are dragged along the electric current direction through the spin-transfer torque and show a transverse motion, known as the skyrmion Hall effect (SkHE), as the topological Hall effect's counterpart.

One can detect the skyrmion formation in a material by monitoring the change in the Hall resistivity. In conventional metallic ferromagnets, the Hall resistivity consists of two different terms, namely the normal Hall effect (NHE), which is proportional to the magnetic field, and the anomalous Hall effect (AHE), which is proportional to the magnetization of the material. However, in the presence of topologically non-trivial magnetization configurations, there appears an additional contribution to Hall resistivity, whose magnitude depends on the configuration, termed as topological Hall effect. This physical phenomenon can be understood elegantly by using the concept of an emergent magnetic field associated with the non-trivial topology [119]. For a smoothly varying magnetization, the emergent magnetic field can be calculated as :

$$\mathbf{B}_i^e = \frac{h}{8\pi e} \epsilon_{ijk} \mathbf{m} \cdot (\partial_j \mathbf{m} \times \partial_k \mathbf{m}) \quad (3.6)$$

Here, \mathbf{m} represents the unit vector field in the magnetization direction, and ϵ_{ijk} is the totally antisymmetric tensor. Comparing equation 3.6 and equation 3.2, one can obtain the emergent magnetic field's value induced by an individual skyrmion as $\phi_{\text{sky}} = \frac{h}{e} Q$. The emergent magnetic field acts like a classical magnetic field, and hence, the expression of THE resistivity is given by :

$$\rho^T = PR_0 B_i^e \quad (3.7)$$

3.1 Analytic treatment of magnetic skyrmions

Here P is the spin polarization, and R_0 is the normal Hall coefficient.

In addition to THE, the flow of conduction electrons leads to the dynamics of skyrmions. The flow of conduction electrons provides spin-transfer torque to the underlying spin texture through the adiabatic exchange of spin-angular momentum, which causes the longitudinal motion of skyrmions along the electric current direction. Furthermore, as a counterpart to THE, skyrmions move in the opposite direction of the deflected electrons. One can draw a similarity of this motion with the Magnus force felt by a spinning object traveling through a medium. This transverse motion of skyrmions with respect to the current direction is termed as the skyrmion Hall effect (SkHE).

Based on the LLG equation, which accounts for spin-transfer torque effects (equation 2.30), one can write an equation of motion for the skyrmions according to the Thiele equation [26] :

$$\mathbf{G} \times (\mathbf{v}^e - \mathbf{v}^d) + \mathcal{D}(\beta\mathbf{v}^e - \alpha\mathbf{v}^d) + \mathbf{F} = 0 \quad (3.8)$$

\mathbf{G} is gyromagnetic coupling vector, \mathcal{D} is the dissipation force tensor, and \mathbf{F} is the force experienced by the magnetization configuration from the surroundings. The constants α and β represent the Gilbert damping and non-adiabaticity of the material, respectively. Further, \mathbf{v}^e represents the velocity of the electrons, and \mathbf{v}^d is the skyrmion's total drift velocity. The first term of the equation captures the skyrmion's transverse motion with respect to the current direction, and it is typically zero for topologically trivial magnetization configurations. Iwasaki et al. [120] derived an expression for \mathbf{v}^d in terms of \mathbf{v}^e , for a skyrmion crystal state, given as follows :

$$\mathbf{v}^d = \mathbf{v}_{\parallel}^d + \mathbf{v}_{\perp}^d \quad (3.9)$$

$$\mathbf{v}_{\parallel}^d = \left(\frac{\beta}{\alpha} + \frac{\alpha - \beta}{\alpha^3(\mathcal{D}/G)^2 + \alpha} \right) \mathbf{v}^e \quad (3.10)$$

$$\mathbf{v}_{\perp}^d = \frac{(\alpha - \beta)(\mathcal{D}/G)}{\alpha^2(\mathcal{D}/G)^2 + 1} (\hat{z} \times \mathbf{v}^e) \quad (3.11)$$

\mathbf{v}_{\parallel}^d and \mathbf{v}_{\perp}^d represent the parallel and perpendicular components of skyrmion drift velocity with respect to the current direction.

Since individual skyrmions carry emergent magnetic flux, their motion also induces an emergent electric field in analogy to Faraday's law [119].

3.2 Studies involving statics and dynamics of 3D skyrmions

$$E_i^e = \frac{\hbar}{4\pi e} \mathbf{m} \cdot (\partial_i \mathbf{m} \times \partial_t \mathbf{m}) \quad (3.12)$$

The emergent electric field of the moving skyrmions can act as a current dependent suppression of THE. According to Faraday's law, one can also express the emergent electric field as $E_i^e = -\mathbf{v}^d \times B_i^e$, where \mathbf{v}^d is the skyrmions' drift velocity. Hence, the total force on the conduction electrons can be expressed as $F = qE_i^e + q\mathbf{v}^e \times B_i^e = q(\mathbf{v}^e - \mathbf{v}^d) \times B_i^e$, where \mathbf{v}^e is the electron velocity. Hence, one may infer that the topological Hall resistivity is decreased by a fraction of the ratio between charge carrier and skyrmion velocities $\mathbf{v}^e/(\mathbf{v}^e - \mathbf{v}^d)$.

3.2 Studies involving statics and dynamics of 3D skyrmions

The study of skyrmions presented in this thesis concerns three-dimensional skyrmions (Bloch skyrmions) stabilized in bulk materials lacking spatial inversion symmetry. Hence, this section's focus will be to present an overview of essential studies on static and dynamic properties of three-dimensional skyrmions. Apart from bulk materials, skyrmions have been stabilized and studied extensively in metallic films and multilayers [70], where they are stabilized primarily by DMI induced at the material interface. The study of different topologically non-trivial magnetization configurations, including skyrmions, in achiral materials stabilized due to competing interactions, has also gathered traction in recent years [121–123].

3.2.1 Skyrmion observation and stability

The seminal work of Mühlbauer *et al.* [1] in 2009 presented a first experimental observation of skyrmion crystal (SkX) in bulk MnSi, with the help of small angle neutron scattering experiments (SANS). Following the study was a real space imaging of SkX in $\text{Fe}_{1-x}\text{Co}_x\text{Si}$ thin film in 2010 using Lorentz transmission electron microscopy by Yu *et al.* [23]. Both the studies plot a phase diagram of different magnetization states stabilized in the geometry with changing external magnetic field and temperature (Fig. 3.3). In the bulk MnSi sample, the SkX was observed in a small pocket just below the material's ordering temperature ($T_c = 29.5\text{ K}$), also traditionally known as

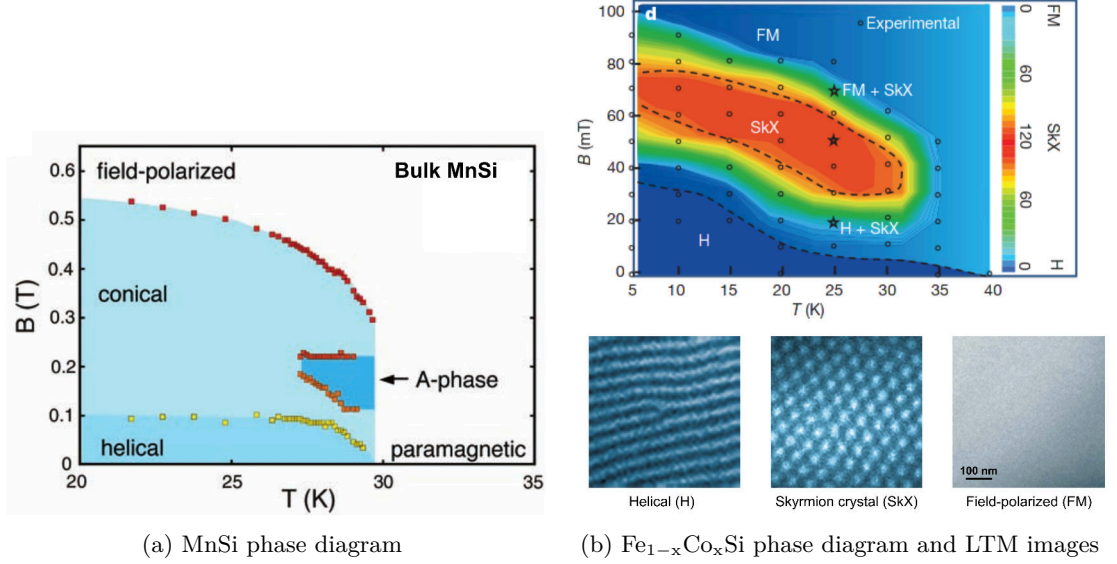


FIGURE 3.3 – The image shows phase diagram between external magnetic field and temperature for (a) bulk sample of MnSi, where we see that the SkX state is stabilized in a small pocket know as the A-phase, and (b) thin film of $\text{Fe}_{1-x}\text{Co}_x\text{Si}$ with thickness less than long range helical period. The inset show LTEM images of the helical, skyrmion crystal and field-polarized phase. (a) has been adapted from reference [1] and (b) has been adapted from reference [23]

the *A-phase*. In the *A-phase*, skyrmions are observed in a two-dimensional triangular (hexagonal) lattice arrangement. Except for the SkX, the phase diagram shows a helical phase, a conical phase, and a field polarized phase. The helical phase is observed at low external fields (below T_c), where the magnetization helix formation is due to the competing symmetric exchange interaction and anti-symmetric DMI. With increasing external field, the propagation direction of magnetization helices aligns with the field direction giving the conical phase. Finally, by further increasing the external field, one obtains the field-polarized phase, where the magnetization mostly points in the field direction. In the study of thin films of $\text{Fe}_{1-x}\text{Co}_x\text{Si}$ as well, three primary magnetization phases are reported, namely, the SkX phase, the helical phase, and the ferromagnetic (field-polarized) phase. However, there is a stark difference in the stability of the SkX phase. In the case of a bulk sample, the SkX phase is observed only in a small pocket below T_c , while in the thin film geometry, it ranges throughout the phase diagram.

There have been a series of theoretical studies on isotropic chiral magnets carrying

3.2 Studies involving statics and dynamics of 3D skyrmions

bulk DMI to explore different magnetization ground states with changing film thickness [35, 36, 46]. The phase diagram between the external magnetic field and the film thickness where the lateral dimensions are infinite and the thickness is quantized shows increasing skyrmion stability with decreasing film thickness (Fig. 3.4). Further, the studies on confined geometries of isotropic chiral magnets [43, 45], where all the dimensions are finite, show that skyrmions have even higher stability in confined geometries. Based on the fact that the skyrmion stability depends on film thickness, in part III, we present a way to confine three-dimensional skyrmions to a desired region of the geometry. The skyrmions' enhanced stability in confined geometries and control over its position can prove beneficial for nanotechnology device applications [124]. It is also interesting to note that the thickness dependence of a magnetic ground state in the chiral magnets give rise to magnetization configuration such as a chiral bobber state (ChB) [35, 125] and a stacked spin spiral state (StSS) [36]. The magnetization configuration of a ChB state resembles a three-dimensional skyrmion state, which terminates in a Bloch point, whereas the StSS state represents a conical state in bulk with a helical modulation at the surface.

Over time, researchers have identified the possibility of obtaining metastable skyrmion configuration far from thermodynamic equilibrium. In materials with bulk DMI such as $\text{Fe}_{1-x}\text{Co}_x\text{Si}$ [126], $\text{Co}_8\text{Zn}_8\text{Mn}_4$ [127], MnSi [128], and Cu_2OSeO_3 [129], studies have shown that it is possible to stabilize a skyrmion phase, with the help of rapid field cooling, even though it is not the thermodynamic ground state. The obtained skyrmion phases were found deep within the field polarized state or at a zero external field or even a reversed external field.

Seki *et al.* [24] reported the first experimental observation of SkX state in a chiral multiferroic material (Cu_2OSeO_3) with Lorentz transmission electron microscopy. Cu_2OSeO_3 is a non-centrosymmetric ferrimagnet hosting bulk DMI. It was observed that the change from a helical to a field-polarized or a skyrmion phase leads to a corresponding change in material polarization along the field direction. Hence, changing electric polarization in the material corresponding to the magnetization phase can be used to manipulate the magnetization with an electric field. For example, one can use a spatial electric field gradient to displace isolated skyrmions in such systems, which can, in turn, be a very promising avenue for low energy device applications.

3.2 Studies involving statics and dynamics of 3D skyrmions

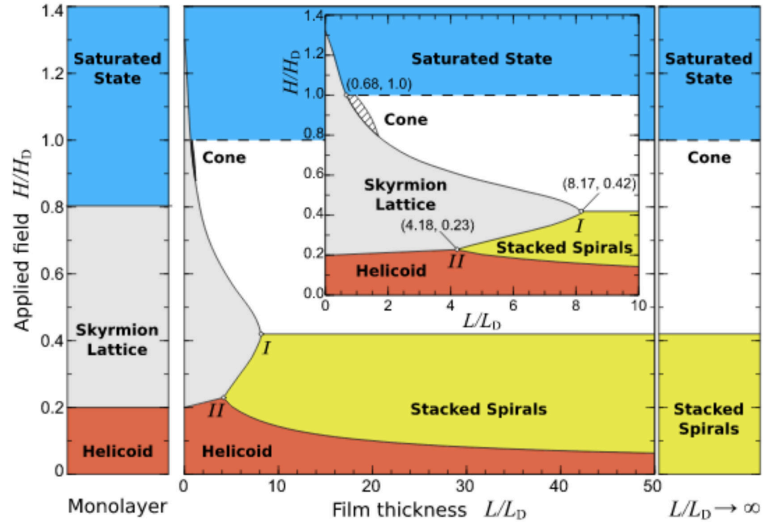


FIGURE 3.4 – The image shows a phase diagram, calculated through numerical simulations, of a chiral magnet plotted between an external magnetic field and the film thickness. It is interesting to note that the SkX phase becomes more prominent with decreasing film thickness. Hence, one can conclude that the stability of a skyrmion depends on the dimensions of the host material. The image is adapted from ref. [36]

3.2.2 Skyrmion motion under electric current

Soon after the experimental observation of the skyrmion crystal (SkX) phase in MnSi, Yu *et al.* [2] reported the current-driven motion of the SkX phase in 2012. The skyrmions were observed to move at very low current densities (of the order of 10^6 A m^{-2}) compared to the previously studied magnetic domain walls. This observation gave a substantial impetus to the study of magnetic skyrmions for memory device applications such as skyrmion based racetrack geometry [7]. Another important observation regarding the skyrmion motion was its lateral deflection, perpendicular to the current direction, *i.e.*, skyrmion Hall effect (SkHE). Due to its non-trivial topology, the skyrmions feel a Magnus force in addition to the force along the direction of the spin-polarized current. This phenomenon was explained theoretically based on the conduction electrons acquiring a Berry phase while adiabatically aligning their magnetic moments with the smooth skyrmion magnetic texture [119] and arguments derived from the Thiele equation [26] as discussed in section 3.1.2.

The first numerical study to understand the motion of SkX in chiral magnets was reported by Iwasaki *et al.* [120] in 2013. Including the in-plane STT term, the LLG equation (Section 2.2.2) gave the evolution of magnetization in the material. Further, based on the Thiele equation, the authors derived the total drift velocity of the SkX in the direction of the current ($\mathbf{v}_{\parallel}^{\text{d}}$) and perpendicular ($\mathbf{v}_{\perp}^{\text{d}}$) to it, as described in the previous section (Section 3.1.2). Both $\mathbf{v}_{\parallel}^{\text{d}}$ and $\mathbf{v}_{\perp}^{\text{d}}$ depend on α and β , the Gilbert damping constant, and the non-adiabaticity constant. It was observed that for small values of α , $\mathbf{v}_{\parallel}^{\text{d}}$ becomes independent of β/α and proportional to the current density. Moreover, when $\beta = \alpha$, $\mathbf{v}_{\perp}^{\text{d}}$ becomes zero.

As an extension of the motion of SkX under an inplane spin-polarized current, Iwasaki *et al.* [130] numerically evaluated the motion of an isolated skyrmion in a confined racetrack-like geometry. The authors reported a repulsive interaction of the skyrmions with the edges using a one-dimensional model, which is essential to understand the stability and shape of skyrmions in confined geometries, as well as their utilization in race-track memory [69]. Qualitatively, the repulsion originates due to the opposite magnetization orientations at the skyrmion and the material boundary. Hence, in the presence of a current along the track's length, the skyrmion's motion can be assumed to be one dimensional due to the repulsive force from the lateral boundaries canceling SkHE. In such a condition, the value of $\mathbf{v}_{\parallel}^{\text{d}}$ becomes directly proportional to β/α ,

3.2 Studies involving statics and dynamics of 3D skyrmions

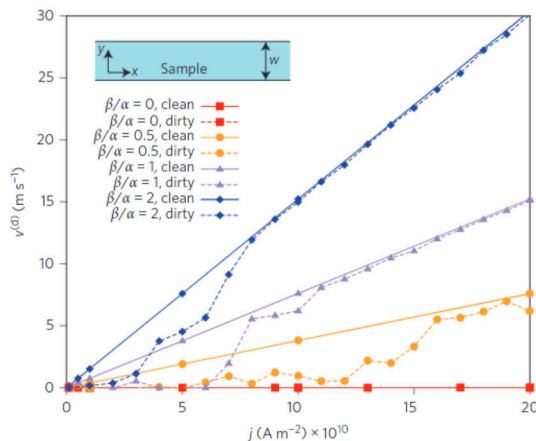


FIGURE 3.5 – Current density vs drift velocity of an isolated skyrmion, with and without impurities, moving along the length of a racetrack-like geometry under the influence of an in-plane current. The current is applied in x -direction and the skyrmion moves along the same direction. Due to the repulsive forces from the material boundary, the skyrmion hall effect is suppressed and the drift velocity becomes proportional to the current density as well as the ratio β/α . The image is adapted from reference [130]

and the current density (Section 7.4.1). However, above a critical current density, the isolated skyrmions get expelled at the material boundary due to SkHE.

The skyrmions have to be driven at high velocities (current densities) in skyrmion based memory devices to keep up with contemporary technological requirements. Hence, the expulsion of skyrmions due to SkHE has become an obstacle in realizing memory devices, often in confined geometries, based on isolated skyrmion motion with an in-plane applied current. Various approaches have been put forward in recent years to tackle this problem, all related to the motion of two-dimensional skyrmions (Néel skyrmions) stabilized through interfacial DMI. One proposed solution is to use synthetic anti-ferromagnets (SAF), which utilize an anti-ferromagnetically exchange-coupled ferromagnetic bilayer as the skyrmion transmission channel instead of a monolayer track [42]. The topological charge carried by the coupled skyrmions is opposite, and hence, experience opposite deflections perpendicular to the current direction, essentially canceling the SkHE.

Another way to counter the SkHE can be by enhancing the energy barriers at the track lateral edges. In part III Section 7.4.1, we propose a way to confine three-

3.2 Studies involving statics and dynamics of 3D skyrmions

dimensional skyrmions (Bloch skyrmions) in an *H-shaped* racetrack geometry. The skyrmions stay confined to the desired central thin track as the enhanced energy barriers at the edges due to thickness modulations counters SkHE (Fig. 7.12).

The Berry phase picked up by the electrons while traversing the smooth magnetization configuration of a skyrmion shows up as an additional term in the measurement of Hall resistivity of the material, except for normal Hall effect and anomalous Hall effect, known as topological Hall effect. Neubauer *et al.* [131] reported the topological Hall effect in the A-phase of MnSi in 2009. It was shown that the device's Hall resistivity increased with the onset of the SkX phase (A-phase). Subsequently, in 2012, Schulz *et al.* [119] reported that the motion of SkX in MnSi, in the presence of an in-plane current, leads to a decrease in the Hall resistivity. These observations form the basis for experimental detection of SkX (also the isolated skyrmions in confined geometries) stabilization and motion by transport measurements.

3.2.3 Dynamical modes of magnetic skyrmions

The first numerical study of magnetization modes in a two-dimensional skyrmion crystal state (SkX) was presented by Mochizuki [132] in 2012. While ignoring the demagnetization field contribution, the author obtained three primary modes, two lateral and one breathing mode, for SkX. The two lateral modes represented a gyrotropic motion of all the skyrmions in counter-clockwise (CCW) and clockwise (CW) direction around the center. These modes were excited with an in-plane external magnetic field pulse. The breathing mode (B) was excited with an out-of-plane field pulse, which leads to a contraction and expansion of the skyrmion core. A detailed numerical study focusing on the breathing modes of an isolated skyrmion in a confined nanodot geometry was presented by Kim *et al.* [133] in 2014. The authors reported that the frequency of the modes depends on the DMI of the material and external magnetic field, which presents a way to detect the skyrmion states experimentally. Following the numerical studies, microwave absorption experiments using a coplanar waveguide on bulk samples of $\text{Fe}_{1-x}\text{Co}_x\text{Si}$, FeGe, MnSi, and Cu_2OSeO_3 [134–137] confirmed the presence of the three magnetization modes.

In contradiction, it has been derived analytically by Guslienko *et al.* [139] in a nanodot that out of the two lateral modes of an isolated skyrmion, only one is a gyrotropic mode. The other is an azimuthal spin-wave mode. The authors also derived that the

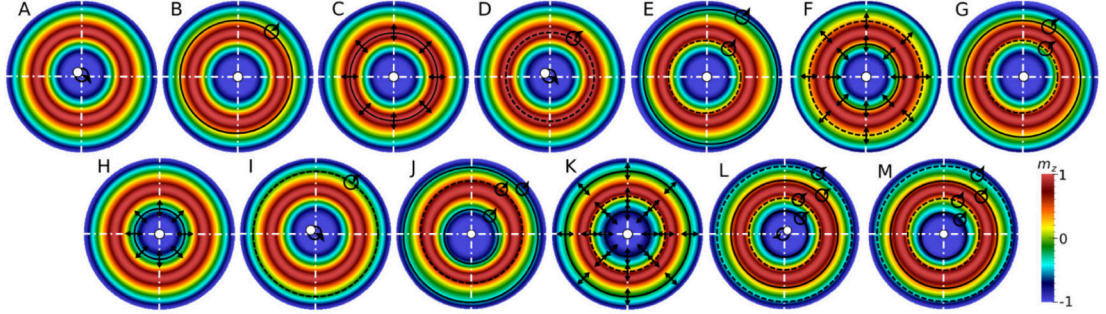


FIGURE 3.6 – Simulation of different dynamical magnetization modes of an isolated skyrmion, obtained in a thin disc geometry of chiral magnets having bulk DMI. Mode A and mode B are the two primary lateral modes excited with an in-plane magnetic field pulse. Mode A is a gyrotropic mode, while mode B is an azimuthal mode. An out of plane field pulse excites mode C which is a radial (breathing) mode. For high values of Gilbert damping (α), the higher order modes (D-M) are suppressed. The image is adapted from reference [138].

gyrotropic mode frequency depends on the nanodot radius, and the gyration direction depends only on the polarity of the skyrmion core [139]. In a numerical study by Xuan *et al.* [140], the skyrmion's gyrotropic motion, as it relaxes towards the equilibrium, has been further investigated in a thin disc geometry (Fig. 3.7(a)-(b)). In addition to the findings reported earlier, it was observed that the frequency of skyrmion gyration depends on the distance of the skyrmion center from the disc center. Hence, the skyrmion follows a non-uniform gyration motion in a spiral orbit as it relaxes towards the center of the disc. Further, it corroborates that the skyrmion's non-uniform motion can be explained with the help of the Thiele equation [26], and the skyrmion mass is zero. Beg *et al.* [138] reported an extensive collection of dynamical modes of an isolated skyrmion in a thin disc geometry below 50 GHz regime (Fig. 3.6). The collection of modes includes, as previously discussed, two lateral and one breathing mode. The authors found one of the lateral modes to be gyrotropic, and the other an azimuthal mode. Further, it was observed that the frequencies of the modes depend on the disc diameter and the strength of the external magnetic field used to stabilize the skyrmion.

The observations mentioned above diverges from the motion of a bubble skyrmion in confined geometries [142–144]. The bubble skyrmion shows a *hypocycloid* trajectory when perturbed from the equilibrium position (Fig. 3.7(c)). The hypocycloid trajectory

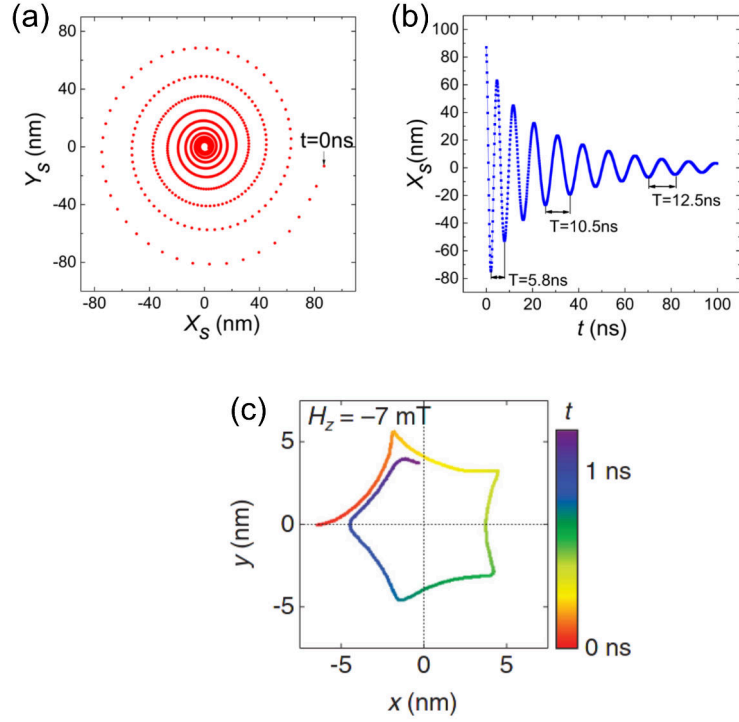


FIGURE 3.7 – The graphs compare gyrotropic motion of a perturbed (a)-(b) skyrmion, stabilized by DMI, and (c) a bubble skyrmion, as it relaxes towards the center in the nanodot geometry. (a) shows the x and y co-ordinate of the skyrmion center and (b) shows corresponding evolution of x co-ordinate with time. One can observe that the motion is a non-uniform gyrotropic motion. (c) shows the hypocycloid gyrotropic motion of the skyrmion bubble. Image (a) and (b) are adapted from reference [140]. Image (c) has been adapted from reference. [141].

3.3 Chiral magnetization structures in 3D

can be interpreted as a superposition of two gyrotropic modes, with different frequencies, in opposite directions (CW and CCW). To explain this motion with the Thiele equation, one must consider the skyrmion's effective mass. It can be argued that the difference in gyrotropic modes of skyrmion stabilized by DMI and a bubble skyrmion comes from the magnetization configuration's rigidity. The DMI stabilized skyrmions are typically smaller in size and more rigid in comparison to the bubble skyrmions. This may lead to suppression of internal degree of freedom, and hence, fewer excitation modes.

Although not in this study's scope, a full magnonic spectrum of SkX is fascinating from both theoretical and application point of view. A comprehensive discussion of the topic can be found in the reviews [145] and [137]. Another interesting development is the recent studies suggesting that individual skyrmion strings (three-dimensional skyrmions) can function as magnonic waveguides [146–148]. It has been found, both theoretically and experimentally, that the skyrmion strings show a non-reciprocal propagation of spin excitations along their length, suggesting that they can also be used as robust information transmission lines.

3.3 Chiral magnetization structures in 3D

As discussed in the previous sections of this chapter, in ferromagnets with broken spatial inversion symmetry (non-centrosymmetric ferromagnets), competition between bulk DMI [149] and ferromagnetic exchange interacts give rise to chiral three-dimensional magnetization structures. In this section, we list some of the chiral magnetization configurations, except for the 3D magnetic skyrmion, which are relevant to the studies presented in part III. Typically, one may characterize two-dimensional chiral structures with skyrmion number Q , which considers their non-trivial topology. However, since we are primarily interested in three-dimensional chiral structures, it is not intuitive to use only Q in each case. Instead, we utilize iso-surfaces, which separates magnetization regions, pointing in and opposite direction of the external magnetic field, to classify the magnetization structures.

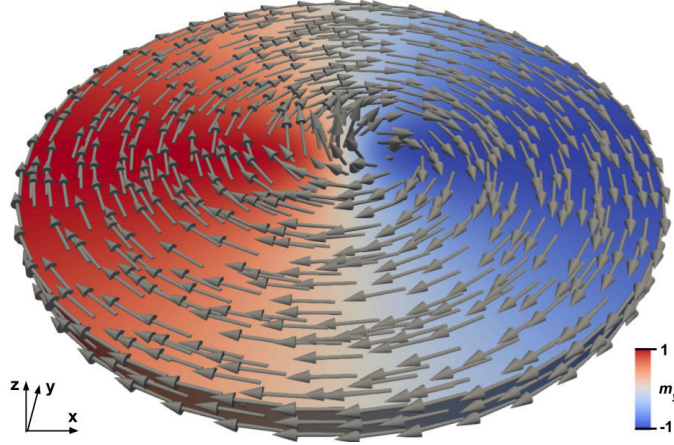


FIGURE 3.8 – The image shows a magnetic vortex in a permalloy disc of radius 50 nm and thickness 5 nm.

3.3.1 Magnetic vortex

Magnetic vortices are regions where the magnetization circulates in a plane around a central point known as the vortex core. They usually develop in extended thin films or sufficiently large thin-film elements (Fig. 3.8). The structure closes the magnetic flux and is divergence-free, making it a favorable magnetization configuration to minimize the magnetostatic energy. In the center of the vortex, the magnetization turns out of the plane. It allows for a smooth change of the magnetization and prevents a singularity of the center's micromagnetic exchange energy. According to the pole avoidance principle [105], the nanometer-sized core amounts to only a small surface charge.

Analogous to the domain wall width [106], one can define the radius of a vortex core as :

$$r_{\text{core}} = \left(\frac{d \sin(\phi)}{dr} \right)^{-1} \quad (3.13)$$

Here ϕ is the polar angle of the in-plane magnetization at $r = 0$. In their variational approach for a film of thickness h , Usov and Peschany [150] derived vortex radius as follows :

$$r_{\text{core}} = 0.68 l_{\text{exc}} \left(\frac{h}{l_{\text{exc}}} \right)^{1/3} \quad (3.14)$$

Magnetic vortex has a topologically non-trivial magnetization structure. Like a magnetic skyrmion that possesses skyrmion number $Q = \pm 1$, a magnetic vortex carries a skyrmion number $Q = \pm \frac{1}{2}$.

3.3.2 Bloch point

Bloch points were first found or predicted by Feldtkeller and by Döring [151, 152]. Later, Arrott, Heinrich and Aharoni predicted that Bloch points would form and propagate during the magnetization reversal in soft-magnetic nanowires [153]. It was then confirmed in simulation studies by Hertel in 2002 [154, 155]. Recent experiments [156] have evidenced the formation of Bloch points in magnetic nanowires. A. Hubert [88] described the Bloch point as a micromagnetic point singularity, around which one finds all the possible magnetization orientation on an arbitrary shell containing the Bloch point. This definition leads to an abrupt change in magnetization at the atomic scale as the shell's radius approaches the dimensions of the lattice constant. Bloch point is considered a micromagnetic singularity as it violates the fundamental assumption of micromagnetism, where the magnetization varies smoothly at the atomic scale. In the micromagnetic framework, Bloch points are studied by keeping the value of saturation magnetization (M_s) constant [151, 152, 157] or allowing a local modulation in its value [158]. Due to the abrupt change in the magnetization, the symmetric exchange interaction that tends to align the magnetization in a single direction gets strongly frustrated. In the micromagnetic picture, this leads to an infinite value of the local exchange energy density. However, integrating the energy density over a volume gives a finite value of exchange energy [159]. Hence, for our study, we assume the value of saturation magnetization constant when studying chiral magnetization configurations such as a chiral bobber (section 5.1.4), which contains a Bloch point.

Analytically, Döring and Feldtkeller [151, 152] derived the magnetization configuration equations for a Bloch point.

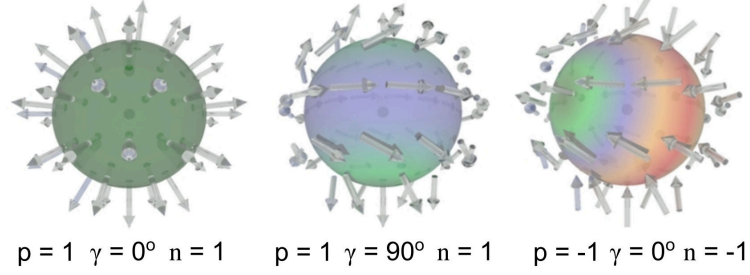


FIGURE 3.9 – Sketch of three types of (anti)Bloch points generated by varying the values of magnetization at poles p , influx angle γ , and vorticity n , with the help of equation 3.15.

$$\begin{aligned}
 m_x &= \cos(\Phi)\sin(\Theta) \\
 m_y &= \sin(\Phi)\sin(\Theta) \\
 m_z &= \cos(\Theta) \\
 \Theta &= p \theta + \pi (1 - p)/2 \\
 \Phi &= n \phi + \gamma
 \end{aligned} \tag{3.15}$$

Here θ is the azimuthal angle, ϕ is the polar angle, p is the magnetization pointing in and out of the Bloch point at the poles, n is the magnetization's vorticity around the Bloch point, and γ is the influx angle of the magnetization. For $n = +1$, we obtain a Bloch point magnetization (Fig. 3.9), while for $n = -1$, we obtain a anti-Bloch point structure.

One finds Bloch points commonly in materials hosting DMI. Magnetization configuration, such as a chiral bobber [35] or a dipole string [160], contains Bloch points, stabilized by the anti-symmetric exchange interaction DMI. Moreover, they play an essential role in creation and annihilation of magnetic skyrmions, as the skyrmions cannot be uniformly unwound into a ferromagnetic configuration [161].

3.3.3 Helical state

In the absence of or at low values of the external magnetic field, materials with bulk DMI stabilize helical state. At these external field values, DMI and ferromagnetic exchange interaction dominate, giving rise to magnetization spiral. One full rotation of

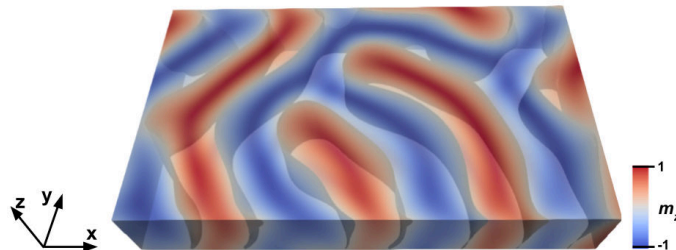


FIGURE 3.10 – Helical state obtained in a thin film of FeGe at a small external field in the $-z$ -direction of strength $H_z = -10$ mT. The color-scheme represents value of the z -component of the magnetization. Further, we show the iso-surfaces corresponding to $m_z = 0$ separating magnetization pointing in and opposite direction of the external magnetic field. The axis of the magnetization helices in the helical state is oriented perpendicular to these iso-surfaces.

such a magnetization helix corresponds to the long-range helical period of the material l_d (equation 2.34). As shown in Fig. 3.10, one can describe the helical state as forming alternating domains pointing in and opposite to the external field direction, separated by iso-surfaces. For a non-centrosymmetric ferromagnet, the helical state is always stable if the material geometry is larger than l_d , as discussed in section 5.2.

3.3.4 Chiral-bobber state

The chiral bobber (ChB) state shares a great deal of similarity with a three-dimensional skyrmion state. It resembles the magnetization configuration of a skyrmion the terminates in a Bloch point. Fig 3.11 shows the iso-surface representation of the ChB state in material with spherical geometry. The region above the Bloch point resembles a skyrmion state, while the region below it resembles a quasi-saturation state along the direction of the external field. Typically, ChB state requires a material thickness of the order of l_d to stabilize [35]. The skyrmion state and the ChB state can co-exist in confined geometries of non-centrosymmetric ferromagnets[37]. The magnetization structure and the impact of the external field on it are described in detail in section 5.2.

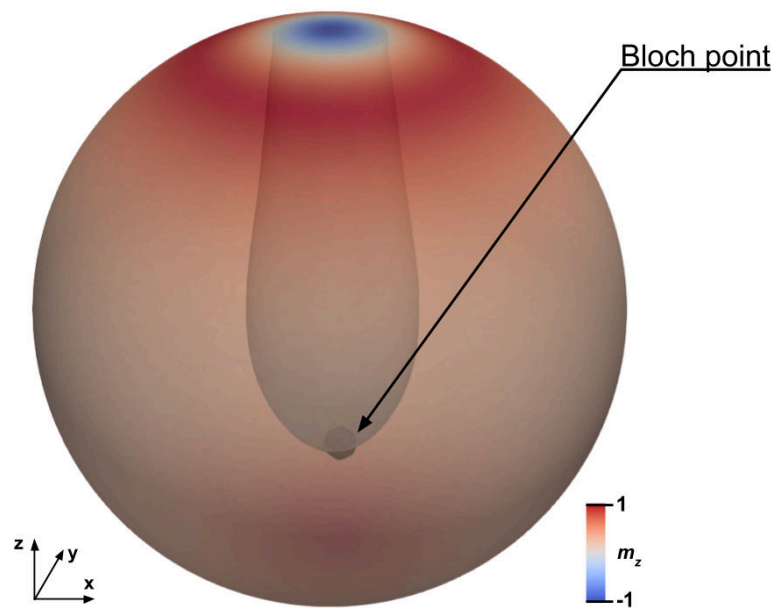


FIGURE 3.11 – The image shows a chiral bobber state obtained in a nanosphere of FeGe of radius 70 nm at an external field in the z -direction of strength $H_z = 200$ mT. The color-scheme represents the magnetization at the surface in z -direction and the iso-surfaces corresponding to $m_z = 0$. Here, one can see that ChB state resembles a skyrmion tube that terminates in a Bloch point.

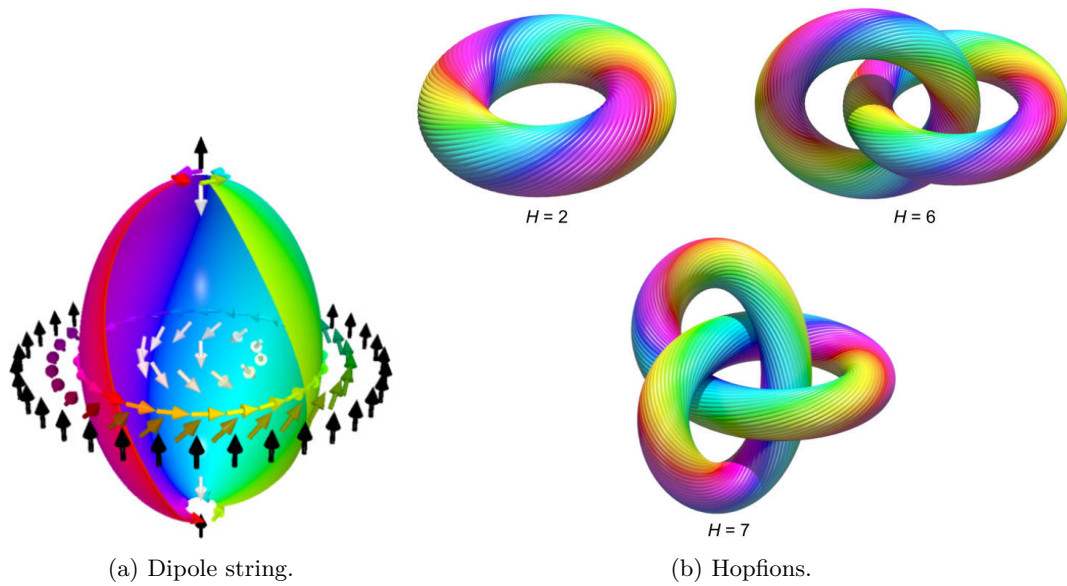


FIGURE 3.12 – The magnetization configuration of (a) dipole string, where two Bloch points of opposite topological charge are connected with a skyrmion tube configuration. (b) hopfions of different Hopf index H , where the iso-surfaces corresponds to the polar angle component of magnetization while the color-scheme corresponds to the azimuthal angle. The image (a) is adapted from reference [160] and the image (b) is adapted from reference [125].

3.3.5 Other chiral magnetization structures

The list of different chiral magnetization configurations goes beyond the ones discussed here. To mention a few, for example, a meron state, where the magnetization configuration resembles a half skyrmion and half helical state (with skyrmion number $Q = \pm\frac{1}{2}$). Merons are typically unstable (unless geometrically confined) and often observed in a coupled state known as Bi-merons [162] (with skyrmion number $Q = \pm 1$). Complex magnetization configuration, such as a dipole string [160] (Fig. 3.12(a)), where a skyrmion tube terminates in two Bloch points (with opposite topological charge) as opposed to a single one as in ChB state, has been proposed to be stable in non-centrosymmetric ferromagnets. Further, it has been shown that higher-order symmetric exchange interaction can stabilize another group of chiral magnetization configurations known as hopfions [125] (Fig. 3.12(b)) through theoretical calculations.

Deuxième partie

Methods

CHAPITRE 4

Numerical implementation

Over the past few decades, computer modeling has become an essential and well-established tool, on equal footing with experiments and theory, to understand phenomena in condensed matter physics and many other scientific domains. In magnetism, micromagnetic simulations have significantly contributed to the understanding of static magnetic structures and the magnetization dynamics in increasingly complex systems. Until recently, researchers used simulations to complement and contribute to the interpretation of experimental data. However, micromagnetic simulations have evolved into an efficient and reliable tool for predicting the behavior of magnetic systems on the nanoscale.

As introduced in the preceding part, the micromagnetic model defines a set of nonlinear partial differential equations in space and time, which can only be solved analytically for simplified cases. In general, the solution of both static and dynamic micromagnetics requires numerical methods. However, memory and time efficient numerical implementation is challenging due to a few properties of the micromagnetic equations. Firstly, the demagnetization field is difficult to calculate rapidly and efficiently because it is a long-range dipolar interaction. A simple numerical implementation of such an interaction has a computational complexity of problem scaling as $\mathcal{O}(n^2)$, where n is the number of simulation cells. Various methods have been proposed to reduce this complexity to $\mathcal{O}(n \log(n))$ [163] or even $\mathcal{O}(n)$ [164]; however, they remain non-trivial. Secondly, the exchange interaction adds a local coupling with high stiffness due to its second order in space. The competition of the long-range demagnetization field with the local exchange field is crucial for simulating realistic magnetization structures; however, it will have high computational demand on the numerical time-integration solvers. Finally, most of the energy contributions' nonlinear nature leads to a complex energy landscape, making it challenging to seek energy minima, especially when simulating quasi-static processes efficiently.

The magnetism community has developed a fair amount of numerical solutions for tackling the micromagnetic equations. Typically, these methods require different discretizations for space and time. Among the spatial discretizations, the most popular methods applied to micromagnetics are the Finite Difference Method (FDM) and the Finite Element Method (FEM). For both methods, one subdivides the magnetic region into a collection of simulation cells resulting in a cell mesh. However, the requirements for the mesh differ significantly for both methods. While the FDM uses a regular cu-

4.1 Spatial discretization - Finite element method

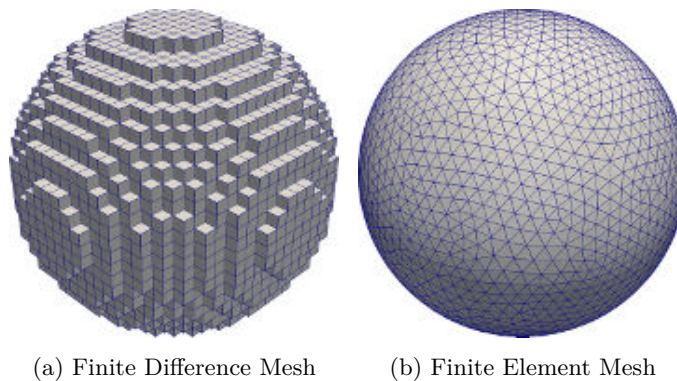


FIGURE 4.1 – The figure compares (a) finite difference mesh with (b) finite element mesh of a sphere. The finite element mesh is able to discretize the geometry better with a fewer number of cells compared to the finite difference mesh.

booid mesh, the FEM utilizes an irregular tetrahedral mesh, see Fig. 4.1. Independent from the discretization method, one has to choose the cell size sufficiently small to accurately resolve magnetization structures. For materials lacking magnetocrystalline anisotropy, this characteristic length (corresponding to individual cell size) should be at least half of the magnetostatic exchange length given by length $l_s = \sqrt{2A/\mu_0 M_s^2}$ (M_s is the saturation magnetization and A is the exchange stiffness constant). The material under investigation in the present study is FeGe, and for this material, we obtain the characteristic length of the mesh to be 4.85 nm. Also, for our study, we use the FEM method for spatial discretization. While it is possible to use either FDM or FEM for the spatial discretization to compute the effective field through the respective energy contributions, another class of algorithms are required to compute the time evolution of \mathbf{M} , according to the LLG.

4.1 Spatial discretization - Finite element method

4.1.1 Simplex Elements

For finite element method calculations, the given sample's volume is entirely divided into non-overlapping basic elements. Further, a set of basis functions are defined to interpolate between a function's values at the vertex points, also referred to as nodes. For example, in a one-dimensional sample, a simplex element is a line segment.

4.1 Spatial discretization - Finite element method

For the line segment, the two endpoints serve as nodes between which the discretized function values are linearly interpolated. It is possible to introduce higher-order interpolations [165] using additional nodes. In two and three dimensions, the simplex element for linear interpolation is the triangle and tetrahedron, respectively. Here, the nodes for interpolations are its corner vertices. By definition, a simplex element has $d+1$ vertices if d is the spatial dimension.

4.1.2 Mesh Generation

It is essential to have a high-quality finite element mesh to reduce numerical errors in the calculations. In contrast to the finite difference method, the mesh generation for a finite element simulation is remarkably involved. Hence, we did not develop and implement a proprietary mesh generator but use the freely available program GMSH [166], which is licensed under the terms of the GNU General Public License [119], to generate meshes containing tetrahedra as simplex elements for our three-dimensional geometries.

In GMSH, an ASCII file describes the sample's geometry employing 1D, 2D, or 3D geometric entities. Points define 1D elements, such as lines or curves. Similarly, several $(n-1)$ dimensional entities define n -dimensional elements that eventually provide a 3D object shape. The meshing algorithm of GMSH starts with 1D elements and subdivides them into line segments with a user defined characteristic length. This characteristic length should be small enough to resolve all the magnetization structures forming in the system to be studied. The 1D mesh serves as a seed for the subsequent Delaunay triangulation [167], which provides a triangular mesh on the sample's surface. This surface mesh then represents the starting point for generating a 3D mesh assembled by a generalized 3D Delaunay algorithm. The manual of the GMSH project [166] describes the details of the underlying techniques.

4.1.3 Shape functions, their differentiation and integration

Shape function

The finite-element method's essence consists of approximating an unknown function $\mathbf{u}(\mathbf{x})$ through a piecewise linear approximation $\tilde{\mathbf{u}}(\mathbf{x})$. Each tetrahedral element within the mesh defines a unique non-overlapping finite element. The unknown function's discretized values are calculated at the vertices (or discretization nodes) i of each element e . Within an element, the unknown function's value is represented as follows.

4.1 Spatial discretization - Finite element method

$$\begin{aligned}
 \mathbf{u}(\mathbf{x}) &\simeq \tilde{\mathbf{u}}(\mathbf{x}) = \sum_{i=1}^4 N_i^e(\mathbf{x}) \tilde{\mathbf{u}}_i^e & (4.1) \\
 &= (N_1^e(\mathbf{x}) N_2^e(\mathbf{x}) N_3^e(\mathbf{x}) N_4^e(\mathbf{x})) \begin{pmatrix} \tilde{\mathbf{u}}_1^e \\ \tilde{\mathbf{u}}_2^e \\ \tilde{\mathbf{u}}_3^e \\ \tilde{\mathbf{u}}_4^e \end{pmatrix} \\
 &= N^e(\mathbf{x}) \tilde{\mathbf{u}}^e
 \end{aligned}$$

Here, $\tilde{\mathbf{u}}_i^e$ represents the discretized value of $\mathbf{u}(\mathbf{x})$, and $N_i^e(\mathbf{x})$ represents the shape function for node i . The row matrix $N^e(\mathbf{x})$ is the element's shape function matrix. The shape functions N_i^e interpolate the computed function between the nodes of the element. The shape functions of the following form is written for a linear interpolation.

$$N_i^e(\mathbf{x}) = \frac{1}{6V_e} (a_i + b_i x + c_i y + d_i z) \quad (4.2)$$

Here, \mathbf{x} is the node position vector, and V_e the volume of the tetrahedral element. For each node i , the coefficients depend on the shape of the finite element and are normalized such that :

$$N_i^e(\mathbf{x}_j) = \delta_{ij} \quad (i, j = 1, \dots, 4) \quad (4.3)$$

We show the examples of shape functions in one and two dimensions schematically in Fig. 4.2. Above written equations (equation 4.3) are a set of linear equations that yield the coefficients for defining the shape functions. Hence, one may compute the value of the shape functions at a given point \mathbf{x} from the coordinates of each vertex of the tetrahedron within an element e as follows.

$$N_i^e(\mathbf{x}) = \frac{1}{6V_e} \det \begin{pmatrix} 1 & x & y & z \\ 1 & x_{i+1} & y_{i+1} & z_{i+1} \\ 1 & x_{i+2} & y_{i+2} & z_{i+2} \\ 1 & x_{i+3} & y_{i+3} & z_{i+3} \end{pmatrix} \quad (4.4)$$

For example, coefficient b_i will be :

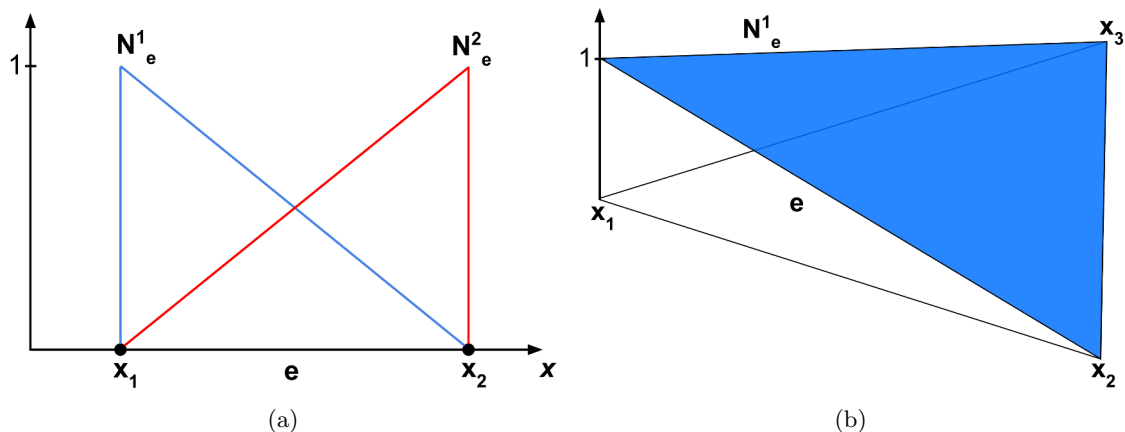


FIGURE 4.2 – Schematic representation of linear element shape functions in (a) one dimension and (b) in two dimensions in an element e , according to the equation 4.2 and 4.3. Notice that, at each point within the element, the sum of all the shape functions is equal to 1.

$$b_i = -\frac{1}{6V_e} \det \begin{pmatrix} 1 & y_{i+1} & z_{i+1} \\ 1 & y_{i+2} & z_{i+2} \\ 1 & y_{i+3} & z_{i+3} \end{pmatrix} \quad (4.5)$$

The three other coefficients are obtained similarly through cyclical permutation. The above equation represents a transformation from Cartesian coordinates to a local coordinate system (barycentric coordinates) in which a weight is assigned to each discretization point based on its surrounding volume.

Higher-order interpolation functions can be used as well, for example, quadratic functions. While these result in higher numeric accuracy, higher interpolation functions are not necessary to accurately calculate the magnetization dynamics. One may increase the density of discretization points to improve the accuracy of a simulation.

The linear shape functions provide a basis for the piecewise linear representation of functions within each discretization element. Hence, the shape functions are the only space-dependent terms. Thus the operations such as differentiation and integration are performed only on the shape functions. Further, one may convert these operations utilizing the coefficient comparison into linear algebra problems.

Differentiation

Using the shape functions, one may write a partial differentiation with respect to, e.g., y -direction of the function $\tilde{\mathbf{u}}(\mathbf{x})$ at a point \mathbf{x} within an element e as follows.

$$\begin{aligned} \frac{\partial \tilde{\mathbf{u}}^e}{\partial y} &= \sum_{i=1}^4 \tilde{\mathbf{u}}_i^e(\mathbf{x}) \frac{\partial N_i^e}{\partial y} \\ &= \sum_{i=1}^4 \tilde{\mathbf{u}}_i^e(\mathbf{x}) c_i^e \end{aligned} \quad (4.6)$$

The value of c_i is in accordance with the equation 4.2.

Generally, one needs to compute the gradient of a function. In that case, the equation 4.6 becomes a matrix multiplication. For individual elements, one may write the gradient as follows.

$$\nabla \tilde{\mathbf{u}}^e(\mathbf{x}) = \begin{pmatrix} b_1^e & c_1^e & d_1^e \\ b_2^e & c_2^e & d_2^e \\ b_3^e & c_3^e & d_3^e \\ b_4^e & c_4^e & d_4^e \end{pmatrix} \begin{pmatrix} u_x^e \\ u_y^e \\ u_z^e \end{pmatrix} = \underline{\underline{\mathbf{B}}}^e \tilde{\mathbf{u}}^e(\mathbf{x}) \quad (4.7)$$

During a preprocessing step in the micromagnetic code, we calculate and store these matrices in order to use them in the main program every time we perform a gradient operation.

Integration

Like the differentiation, one performs the integration on the shape functions. For a finite element of volume V_e , one can integrate a function $\tilde{u}(\mathbf{x})$ as follows.

$$\int_{V_e} \tilde{u}^e(\mathbf{x}) dV = \int_{V_e} \sum_{i=1}^4 \tilde{u}_i^e(\mathbf{x}) N_i^e(\mathbf{x}) dV = \sum_{i=1}^4 \tilde{u}_i^e(\mathbf{x}) V_e \int_{V_e} \frac{N_i^e(\mathbf{x})}{V_e} dV \quad (4.8)$$

The normalized integral $\int (N_n/V_e) dV = 1/4$ within the tetrahedral element is independent of its shape and represents each node's volume fraction. Hence, one can rewrite equation 4.8 as :

4.1 Spatial discretization - Finite element method

$$\int_{V_e} \tilde{u}^e(\mathbf{x}) dV = \frac{1}{4} V_e \sum_{i=1}^4 u_i(\mathbf{x}) \quad (4.9)$$

Below, we also discuss a set of integrals that are important for calculating effective fields corresponding to long-range and local interactions in magnetic materials. Firstly, A characteristic integral resulting from the computation of second-order derivatives, giving a 4×4 stiffness matrix $\underline{\underline{\mathbf{K}}}^e$. One can express the components of the matrix as :

$$K_{ij}^e = \int_{V_e} \nabla N_i^e \nabla N_j^e dV = \sum_{\alpha}^{x,y,z} c_{i\alpha}^e c_{j\alpha}^e V_e \quad (4.10)$$

where $i = 1, \dots, 4$ and $j = 1, \dots, 4$. The terms $c_{i\alpha}^e$ correspond to the components of the matrix $\underline{\underline{\mathbf{B}}}^e$ in equation 4.7, with $\alpha = x, y, z$. Secondly, another often-encountered integral is the mass matrix $\underline{\underline{\mathbf{M}}}^e$. One can express the components of the matrix as [168] :

$$M_{ij}^e = \int_{V_e} N_i N_j dV = \frac{1}{5} (a + \delta_{ij}) V_e \quad (4.11)$$

We calculate these matrices as well during the preprocessing step.

4.1.4 Exchange field

As we mentioned previously in equation 2.22, one can write an effective exchange field expression as follows.

$$\mathbf{H}_{exc} = \frac{2A}{\mu_0 M_s} \nabla^2 \mathbf{m} \quad (4.12)$$

Besides, at the surface ∂S of the material hosting exchange interaction, the boundary condition on the effective exchange field given by Rado and Wertmann [169] dictates :

$$\left. \frac{\partial \mathbf{m}}{\partial \mathbf{n}} \right|_{\partial S} = 0 \quad (4.13)$$

First, we convert the partial differential equation 4.12 into an equivalent *weak form* by multiplying each side by an arbitrary test function \mathbf{u} and integrating over the magnetic volume V .

4.1 Spatial discretization - Finite element method

$$\int_V \mathbf{u}^T \mathbf{H}_{exc} dV = \int_V \frac{2A}{\mu_0 M_s} \mathbf{u}^T (\nabla^2 \mathbf{m}) dV \quad (4.14)$$

The components of vector \mathbf{u} are three arbitrary test functions $u(x)$, $u(y)$, and $u(z)$. Considering the above equation holds for an arbitrary test function, the equation 4.12 and equation 4.14 are the same.

Applying the integration by parts identity to the equation 4.14, we obtain :

$$\int_V \mathbf{u}^T \mathbf{H}_{exc} dV = -\frac{2A}{\mu_0 M_s} \int_V (\nabla \mathbf{u})^T \nabla \mathbf{m} dV + \frac{2A}{\mu_0 M_s} \int_{\partial S} \mathbf{u}^T \nabla m dS \quad (4.15)$$

However, the boundary condition dictates that the surface integral at the material's boundary be zero (equation 4.13). Hence, one can rewrite the above equation as :

$$\int_V \mathbf{u}^T \mathbf{H}_{exc} dV = -\frac{2A}{\mu_0 M_s} \int_V (\nabla \mathbf{u})^T \nabla \mathbf{m} dV \quad (4.16)$$

Thus, the solution is *weak* in the sense that it has lower requirements of differentiability than in the original form. Instead of requiring two-fold differentiability (equation 4.12), the function only needs a square-integrable first derivative.

To solve the equation 4.16 numerically, we divide the region V into N finite elements. For simplicity, we represent \mathbf{H}_{exc} to varying only in x -direction in the equation 4.16.

$$\sum_{e=1}^N \int_{V_e} u_x H_{exc,x} dV = -\frac{2A}{\mu_0 M_s} \sum_{e=1}^N \int_{V_e} \nabla u_x \nabla m_x dV \quad (4.17)$$

Here, we integrate the equation for the volume of individual elements and sum it over all the total volume elements. With the help of equation 4.2, one can represent the quantities u_x , m_x , and $H_{exc,x}$ within the basis of the shape functions in each element e :

4.1 Spatial discretization - Finite element method

$$\begin{aligned}
 u_x^e(\mathbf{x}) &\simeq \sum_{i=1}^4 u_x^i N_i^e(\mathbf{x}) \\
 m_x^e(\mathbf{x}) &\simeq \sum_{j=1}^4 m_x^j N_j^e(\mathbf{x})
 \end{aligned} \tag{4.18}$$

$$H_{exc,x}^e(\mathbf{x}) \simeq \sum_{l=1}^4 h_x^l N_l^e(\mathbf{x}) \tag{4.19}$$

This method of converting a continuous operator problem to a discrete one is known as the Galerkin method. Hence, one can rewrite equation 4.17 as :

$$\sum_{e=1}^N \sum_{i=1}^4 \sum_{l=1}^4 u_x^i h_x^l \int_{V_e} N_i^e N_l^e dV = -\frac{2A}{\mu_0 M_s} \sum_{e=1}^N \sum_{i=1}^4 \sum_{j=1}^4 x^i m_x^j \int_{V_e} \nabla N_i^e \nabla N_j^e dV \tag{4.20}$$

This equation must hold for any value set u^i given the arbitrary test functions. Hence, one can solve the equation by comparing the coefficients of u_x^i on both sides. This comparison converts equation 4.20 into four linear equations within each element. However, the stiffness matrix (equation 4.10), also known as the Galerkin matrix, which appears on the right-hand side, is not diagonal and requires solving the full system of linear equations. We use a mass-lumping technique to increase the calculation speed, allowing diagonalization of the matrix [165, 170]. This approximation assigns a homogeneous exchange field within each element and yields $\underline{\underline{K}}_{ij}^e = V_e/4$ for the stiffness matrix. For sufficiently small cell sizes, the approximation holds well [170].

Thus we can write the expression for the exchange field h^l at each node l in equation 4.20 as :

$$h_x^l = -\frac{2A}{\mu_0 M_s} \frac{4}{\sum_{e=1}^k V_e} \sum_{e=1}^k \left(\sum_{\alpha}^{x,y,z} c_{i\alpha}^n c_{j\alpha}^n \right) m_x^j V_e \tag{4.21}$$

In the above equation, V_e is the volume of the element e containing the node i , while $\sum_{e=1}^k V_e/4$ is the volume associated with the node i , computed over all k elements containing this node (the support of node i). One can rewrite the equation 4.21 in short as :

$$h_\alpha^i = \underline{\underline{\mathbf{A}}}_{ij} \cdot m_\alpha^j \quad (4.22)$$

for each component $\alpha = x, y, z$ with :

$$\underline{\underline{\mathbf{A}}}_{ij} = -\frac{2A}{\mu_0 M_s} \frac{4}{\sum_{e=1}^k V_e} \sum_{e=1}^k \left(\sum_{\alpha}^{x,y,z} c_{i\alpha}^n c_{j\alpha}^n \right) V_e \quad (4.23)$$

The matrix $\underline{\underline{\mathbf{A}}}$ is sparse and can thus be stored compactly. Similarly, we calculate the effective field for another local interaction used in our study, i.e., DMI [171]. The implementation of the effective field of the DMI in our code has been tested and compared with other codes in a dedicated standard problem with results [31].

4.1.5 Magnetostatic field

Some effects in micromagnetism prohibit a treatment by simple matrix-vector multiplications. The most prominent example is the calculation of the demagnetizing field, according to equation 2.17. Instead of performing a two-fold volume integral to calculate the field resulting from the magnetostatic long-range interaction, it is numerically more convenient to calculate the magnetostatic scalar potential by solving the partial differential equation using the Galerkin Method. As introduced in Section 2.1.3, U is the solution of the Poisson equation :

$$\Delta U = -\nabla \cdot \mathbf{M} \quad (4.24)$$

However, outside the volume of the magnetic material, the above equation will be :

$$\Delta U = 0 \quad (4.25)$$

Furthermore, one needs to satisfy the following condition at the boundary of the magnetic material.

$$U^{\text{in}} = U^{\text{out}} \quad (4.26)$$

$$\left(\nabla U^{\text{in}} - \nabla U^{\text{out}} \right) \cdot \mathbf{n} = \mathbf{M} \cdot \mathbf{n} \quad (4.27)$$

4.1 Spatial discretization - Finite element method

In addition to these conditions, the scalar potential should decay to zero at the infinity (open boundary condition).

$$\lim_{x \rightarrow \infty} U(\mathbf{x}) = 0 \quad (4.28)$$

Hence, Poisson equation is solved in the complete space \mathbb{R}^3 , which is not trivially possible with the FEM as it applies only to finite regions. Fredkin and Koehler [172, 173] developed a hybrid finite element/boundary element method to tackle this problem, which does not require considering any nodes outside the magnetic volume.

In this method, we split the potential U into two parts :

$$U = U_1 + U_2 \quad (4.29)$$

Further, one can solve for U_1 as :

$$\Delta U_1 = -\nabla \cdot \mathbf{M} \quad (4.30)$$

$$\nabla U_1^{\text{in}} \cdot \mathbf{n} = \mathbf{M} \cdot \mathbf{n} \text{ (at the boundary)} \quad (4.31)$$

Here, the equations of U_1 are defined only in the magnetic region and the boundary of the magnetic region. The part U_1 is zero outside the magnetic region. Due to the constraints imposed on U by equation 4.26, one can write the equations for U_2 as :

$$U_2^{\text{out}} - U_2^{\text{in}} = U_1^{\text{in}} \quad (4.32)$$

$$\nabla U_2^{\text{in}} \cdot \mathbf{n} = \nabla U_2^{\text{out}} \cdot \mathbf{n} \quad (4.33)$$

$$\Delta U_2 = 0 \quad (4.34)$$

Here, U_2 is generally non-zero all over the space, except as one approaches infinity.

Poisson equation for U_1 can be written in the weak form using a test function v , to solve for the demagnetizing potential U_1 inside the magnetic volume V .

$$\int_V v \Delta U_1 dV = - \int_V \nabla \cdot \mathbf{M} \quad (4.35)$$

Integrating by parts,

$$\int_V \nabla v \cdot \nabla U_1 \, dV - \int_{\partial S} v(\nabla U_1 - \mathbf{M}) \, dS = \int_V \nabla v \cdot \mathbf{M} \, dV \quad (4.36)$$

Using the Neumann boundary condition equation 4.30, we obtain

$$\int_V \nabla v \cdot \nabla U_1 \, dV = \int_V \nabla v \cdot \mathbf{M} \, dV \quad (4.37)$$

One can solve the above equation by expanding its terms in terms of a local basis defined by the shape functions, as described in section 4.1.4. The calculation involves the stiffness matrix on the left-hand side, while the matrix $\frac{V_n}{r} \underline{\underline{\mathbf{B}}}^e$ on the right-hand side.

According to potential theory, one can evaluate U_2 in terms of U_1 , as follows.

$$U_2(\mathbf{x}) = \frac{1}{4\pi} \int_{\partial S} U_1(\mathbf{x}') \frac{\partial G(\mathbf{x}, \mathbf{x}')}{\partial \mathbf{n}(\mathbf{x}')} \, dS \quad (4.38)$$

Here, $G(\mathbf{x}, \mathbf{x}') = 1/|\mathbf{x} - \mathbf{x}'|$ is the Green's function. The integral equation 4.38 holds for every point \mathbf{x} within the magnetic body; however, the integration at each discretization point inside the body is computationally expensive. Instead, one can evaluate the expression at the magnetic material's boundary, yielding Dirichlet boundary conditions for the Laplace equation 4.32 within the magnetic volume. Approaching the boundary from inside the volume, one can express U_2 as [125] :

$$U_2(\mathbf{x}) = \frac{1}{4\pi} \int_{\partial S} U_1(\mathbf{x}') \frac{\partial G(\mathbf{x}, \mathbf{x}')}{\partial \mathbf{n}(\mathbf{x}')} \, dS + \left(\frac{\Omega(\mathbf{x})}{4\pi} - 1 \right) U_1(\mathbf{x}) \quad (4.39)$$

Here, $\Omega(\mathbf{x})$ is the solid angle subtended by the surface at the point \mathbf{x} . Thus, one can evaluate the values of U_2 from the values of U_1 through integration over the sample surface. The discretization of the potentials U_1 and U_2 transforms the above integral into a matrix multiplication :

$$U_2^i = D_{ij} U_1^j \quad (4.40)$$

4.2 Temporal discretization - Integration of LLG equation

The analytic integration of the Green's function over a triangular boundary element was performed by Lindholm [174]. The Laplace equation for U_2 is then solved within the sample using the finite-element method.

The matrix D is dense in the sense that it is mostly populated. Therefore, an increase in the number of boundary nodes leads to a quadratic increase in the memory size required to store the matrix. Typically this defines the limiting size of the micromagnetic problems. However, matrix compression methods have been developed, which reduces the size of such dense matrices without noticeable loss of accuracy. A very efficient method involves using \mathcal{H}^2 hierarchical matrices [30] for large scale magnetostatic calculations.

4.2 Temporal discretization - Integration of LLG equation

After one calculates the total effective field due to different interactions at each node of the FEM mesh, the magnetization's time evolution at respective nodes can be computed using the Landau-Lifshitz-Gilbert (LLG) equation. The time integration of the LLG equation, based on a discretized magnetization distribution at a time t thus yields the distribution at a later time $t + \Delta t$. The simplest numeric integration method is the Euler method, where the magnetization at time $t + \Delta t$ is computed based on a single previous value. Generally, however, explicit methods are not stable, and one needs to resort to implicit schemes.

4.3 Simulation software

The simulation studies presented in this thesis have been carried out with our custom-developed micromagnetic finite-element (FEM) software. Our micromagnetic software package, named `tetmag`, has been developed at the IPCMS in Strasbourg by R. Hertel, whose team has a long-standing tradition in designing and optimizing micromagnetic software[27–29]. The purpose of this code development is to have a precise, flexible, and adaptable numerical instrument that allows to perform research studies on the properties of the magnetization on the nanoscale. Although the development of the micromagnetic code was not part of this thesis, we describe here the main ingredients and properties of the codes, in order to provide insight into this software with which the results have been obtained.

4.3.1 General framework

The micromagnetic simulation code that is used in this thesis can be regarded as a significantly modernized and entirely rewritten version of the previous TetraMag code, which was also originally written by R. Hertel, and which was then further developed in the former Micromagnetic Simulations team in Jülich, Germany [29, 175]. Results obtained with the TetraMag code have been published in dozens of publications over the past years, and some of the former team members are still using that code for their research.

4.3.2 Code architecture and basic features

The new `tetmag` software is programmed mainly in C++ [176] in an object-oriented fashion [177, 178]. This modular code design allows for a large flexibility in changing or adding features of the code, since it makes it particularly easy to insert, modify, or optimize dedicated classes treating specific subtasks, without interfering with the overall architecture of the code. The software thereby also becomes orderly structured and easily maintainable. Internally, the code is rather compact, owing also to the use of high-level libraries like Eigen [179] and boost [180].

The code is thread-parallelized with OpenMP [181], which makes it possible to deploy it to large-scale computing facilities for efficient parallel computing. In fact, many results in this work were obtained through calculations performed on the MesoCenter High-Performance Computing Facility of the University of Strasbourg [182]. In addition, the code also provides the option to conduct GPU-based massively parallel computations. This is achieved by implementing CUDA [183] and in particular the Thrust framework [184] for GPU acceleration. The choice on whether the GPU or the CPU version of the code is used depends mainly on the size of the problem. Large problems involving a few million finite elements can often be conducted more efficiently on GPUs.

The interface with the user is based on simple, human-readable ASCII input files in which various simulation parameters and problem specification are stored. The finite-element meshes used for the simulations can be generated with the freely available gmsh [166] or netgen [185] software. For the visualization of the results, we use the immensely powerful ParaView [186] application, which is equally freely available and which, over the past years, has advanced to a de-facto standard solution for the analysis

and representation of FEM results.

4.3.3 Numerical Implementation of the DMI term

A central task of the micromagnetic code is the efficient calculation of the effective field terms and the partial energies. In section 4.1 we already reported on the details of the FEM implementation of various micromagnetic energy terms and their corresponding effective fields [27]. In spite of a few modernizations and strategical changes regarding the architecture of the code, the principles of how to calculate these effective field contributions numerically, in the context of a FEM formulation using linear simplex elements, has essentially remained the same as in the previous TetraMag code.

The only energy term that has been newly implemented is the “bulk” DMI term

$$E^{\text{DMI}} = \int D\mathbf{m} (\nabla \times \mathbf{m}) dV \quad (4.41)$$

alongside the corresponding effective field term

$$\mu_0 \mathbf{H}_{\text{eff}} = -\frac{1}{M_s} \frac{\delta E^{\text{DMI}}[\mathbf{m}]}{\delta \mathbf{m}} = -\frac{2D}{M_s} \cdot (\nabla \times \mathbf{m}) \quad (4.42)$$

By applying the principles described in section 4.1 on how to perform numerical integrations and differentiations with the FEM, implementing this additional term and the effective DMI field is straightforward.

To validate and compare the results obtained with this newly implemented feature, we have collaborated with other colleagues working on this domain. In particular, we performed static simulation studies on the structure of a skyrmion forming in a FeGe disk of a specific size and compared in detail the results that were obtained with various codes [31]. This test yielded a perfect agreement between the skyrmion profiles and energies obtained with our `tetmag` code and those calculated with other well-established micromagnetic software frameworks such as MuMax3 [32] or OOMMF [33]. Performing such comparisons is a well established procedure in computational micromagnetism, where various Standard Problems are commonly used to compare the results obtained from different codes [34]. A successful comparison with results obtained by other teams helps providing a high scientific confidence and credibility of the numerical results obtained with a simulation software.

4.3.4 Improved magnetostatic field calculation

Our micromagnetic software allows for simulations involving a large number of degrees of freedom, which can extend up to several millions. While in finite-difference simulations, which benefit from comparatively low memory requirements due to their regular discretization grid, such large numbers of discretization cells may not be particularly unusual, problems of such size are difficult to handle with FEM micromagnetic simulations. In our new code, extending the problems towards much larger sizes has become possible owing to the use of $\mathcal{H}2$ hierarchical matrices [187]. This matrix compression method substantially reduces the amount of data storage and computation time that is involved in the application of certain linear operators, which in the FEM formulation take the form of dense matrices and vector-matrix multiplications. A dense matrix of this type occurs in the hybrid FEM-BEM formalism [172] that we use for the calculation of the magnetostatic long-range interaction. This is the only dense matrix involved in the code, all the other matrices are very sparse. Therefore, this part of the algorithm can represent a bottleneck or a limiting factor for larger simulations. As the problem size grows, the dense matrix -in its original form- results in huge memory and computation requirements, which typically limit the size of problems that can be treated in terms of both hardware resources and computation time. In our code, these limitations have been largely removed by replacing the dense matrices with $\mathcal{H}2$ -type matrices. A detailed description of the implementation of the $\mathcal{H}2$ matrix compression scheme in our micromagnetic code is given in Ref. [30]. From a practical perspective, the most important result is that we obtain a nearly linear scaling of the memory requirements as a function of the degrees of freedom. This allows us to treat large problems in acceptable time and by using limited computational resources.

4.3.5 Integration in time

As discussed in section 4.2, the evolution in time of a magnetic structure representing a non-equilibrium state is governed by the Landau-Lifshitz-Gilbert (LLG) equation. In numerical simulations, this temporal evolution is performed stepwise, such that the changes in time occur at discrete points in time, separated by a time interval Δt . In a slightly simplified way, one can say that after each time step Δt , the effective field values are updated according to the new magnetic configuration, and the torque distribution acting on the magnetization changes accordingly. In practice, most of the

effective field values are typically also refreshed at intermediate time steps, such that Δt is subdivided into smaller intervals. Moreover, the time step is usually not constant. For the sake of simplicity, we can ignore these aspects in this discussion, as they concern mathematical details that depend on the specific integration scheme that is being used.

Primarily because of the irregular structure of the discretization mesh, the LLG integration typically results in a mathematically stiff problem in FEM formulations, especially when the damping constant is low. This is a particularly challenging situation, since in these cases an accurate integration in time requires very small time steps. Accordingly, we need to use relatively advanced mathematical tools to address this problem. Our standard integration method is an adaptive Dormand-Prince algorithm [188], *i.e.*, a mixed 4th / 5th order Runge-Kutta-type ODE (ordinary differential equation) integration scheme. Importantly, the algorithm uses adaptive time steps, such that a variable step size is used as a function of the error that is involved. In practice, because of this, we can see huge differences in the computation time depending on the magnetic configuration. For instance, simulations involving the propagation of a Bloch point tend to be much slower than simulations on the propagation of spin waves, which only consider small-angle variations around an equilibrium state. In spite of the adaptive time step, the explicit form of the Dormand-Prince scheme does not always allow for a stable integration, especially when low damping constants and high local torques are involved. In these cases, we use (semi-)implicit schemes, either the Adams method or the BDF (backwards-difference formulation) [189]. These non-explicit ODE integration schemes tend to be somewhat slower than the explicit ones, but they provide very high numerical stability, which in our case means that we can simulate, *e.g.*, the current-driven magnetization dynamics of non-trivial magnetic structures at very low damping values.

Troisième partie

Results

CHAPITRE 5

Three-Dimensional Chiral Magnetization
Structures in FeGe Nanospheres

The study of 3D magnetization structure in non-centrosymmetric materials has revealed a variety of new structures like skyrmion tubes, chiral bobbars and Bloch point structures in helimagnets [35, 36]. In these material types, however, the impact of 3D nanoscale confinement and finite-size effects on the magnetization states has not yet been investigated in detail. It is known that helical states and hexagonal skyrmion lattices can develop in two-dimensional, extended thin films [1, 5], and that the additional degree of freedom that is present in thicker films can give rise to complex magnetization configurations such as skyrmion tubes and chiral-bobbers [35, 36, 46]. Moreover, patterned thin-film elements can host a variety of complex chiral structures [45], including isolated skyrmions [190], spin spirals, and “horseshoe”-type structures [191]. Previous studies on finite-size effects in skyrmionic magnetic material have addressed the impact of the film thickness or the lateral size of thin-film elements, but were generally restricted to flat geometries.

To study the influence of nanoscale 3D confinement on the magnetization states forming in a helimagnetic material, we perform finite-element micromagnetic simulations on FeGe nanospheres. In spite of the simplicity of the geometrical shape, we find highly complex magnetic structures in such nanospheres, depending on the particle size and the applied field. This complexity results from the inherently chiral magnetic properties of the non-centrosymmetric material and the constraints imposed by the finite size of the sample.

The general problem addressed in this study, *i.e.*, identifying the size dependence of the magnetic ground state, has a long tradition in micromagnetic theory and simulations [192–195]. The question of how a magnetic structure is affected by the particle size is often related to the concept of the single-domain limit [196–199], *i.e.*, the critical size below which the magnetization in a particle remains homogeneous. This, in turn, is connected to the concept of micromagnetic exchange lengths, which provide material-specific estimates of the characteristic size of fundamental magnetic microstructures, like the width of domain walls or the size of magnetic vortex cores.

In the case of non-centrosymmetric magnetic materials with intrinsic chiral properties, the long-range helical period $l_d = 4\pi A/|D|$ plays a role similar to the exchange length in ferromagnets. It represents the length of magnetization spirals forming as a compromise between the ferromagnetic exchange and the antisymmetric exchange due to the Dzyaloshinsky-Moriya interaction (DMI). The constant D denotes the strength

FeGe material parameters	
Saturation magnetization (M_s)	384 kA m^{-1}
Exchange stiffness (A)	$8.87 \times 10^{-12} \text{ J m}^{-1}$
DMI constant (D)	$1.58 \times 10^{-3} \text{ J m}^{-2}$

TABLE 5.1 – Material parameters for micromagnetic description of FeGe.

of the DMI, *i.e.*, the tendency to form helical structures, and A is the ferromagnetic exchange constant. The functional form of l_d is different from that of the magnetostatic exchange length $l_s = \sqrt{2A/\mu_0 M_s^2}$ (M_s is the saturation magnetization), because it describes a periodic, constant modulation instead of the usual kink-type transition with a tanh-type profile. Nevertheless, it can be expected to have similar implications on the size-dependence of magnetic structures, namely that chiral and skyrmionic structures develop in particles with sizes exceeding l_d by a sufficient amount. For the studies presented in the thesis, the material of choice is FeGe. It is a well studied non-centrosymmetric ferromagnet [45] with material parameter listed in Table. 5.1. Using these material parameters, one obtains the value of $l_s \simeq 9.5 \text{ nm}$ and $l_d \simeq 70 \text{ nm}$.

We consider spherically shaped nanoparticles of FeGe with particle radius between 40 nm and 100 nm, thereby extending previous studies on the formation of magnetic structures in this material in the case of planar geometries [45, 200]. The spherical shape serves as a simple, fundamental example of a 3D geometry that can host different magnetization states. Moreover, such particles traditionally play an important role in determining the size-dependence of magnetic structures [201].

5.1 Magnetic equilibrium states

By varying the radius of the nanospheres and the external magnetic field (applied along the $+z$ -direction) we obtain, for each combination of radius and external field, a minimum energy equilibrium magnetization state. We first describe in detail the different types of states that we observe. Afterwards, in section 5.2, we discuss their distribution as a function of the external field and the particle size. Although, generally speaking, the modifications that the lowest-energy magnetic structures undergo by changing the size and the external field are not continuous, it is to some extent possible

to interpret the appearance of different magnetization states as a gradual evolution occurring as a result of a changing parameter. To describe such an evolution, we discuss the magnetic ground states found at a fixed sphere radius of 80 nm whilst varying the external magnetic field. The resulting magnetization states are arranged in the order of increasing field.

5.1.1 Helical state

The helical state is characterized by a continuous rotation of the magnetization along an axis perpendicular to the applied field. The magnetization helix is the direct outcome of the competition between the symmetric ferromagnetic exchange interaction and the anti-symmetric DMI. Alternatively, the arrangement of the magnetization can be interpreted as a periodic sequence of narrow alternating domains, pointing along and opposite to the direction of the external magnetic field, and separated by Bloch walls with the same sense of rotation. These alternating domains can be visualized with the help of iso-surfaces corresponding to $m_z = 0$, as shown in Fig. 5.1a. In this picture, the $m_z = 0$ isosurfaces can be regarded as *hypothetical* domain walls separating domains aligned parallel and antiparallel to the external field. Since the spatial rotation of the magnetization is rather continuous than localized within domain walls, this interpretation of alternating domains is not strictly correct in micromagnetic terms. Nevertheless, this picture can help to understand the transition towards other states, as described later.

The slice of the magnetization configuration displayed in Fig. 5.1b) shows a right-handed helix extending throughout the sphere, along an axis perpendicular to the external field. One full rotation of this helix occurs on a distance corresponding to the long-range helical period [202] of the material $l_d \simeq 70$ nm. The line scan displayed in Fig. 5.1c) shows that the computed data fits well with the assumption of a perfect spin spiral, with sinusoidal oscillations of the m_z component along the spiral axis. Minor deviations from the ideal value are expected because the analytic calculation of the spin spiral does not consider problem-specific aspects that are included in the simulation, such as the spherical shape, boundary conditions [171], and the magnetostatic interaction. According to our simulations, this helical state is energetically favorable at zero or low external magnetic field, where the exchange energy and DMI dominate.

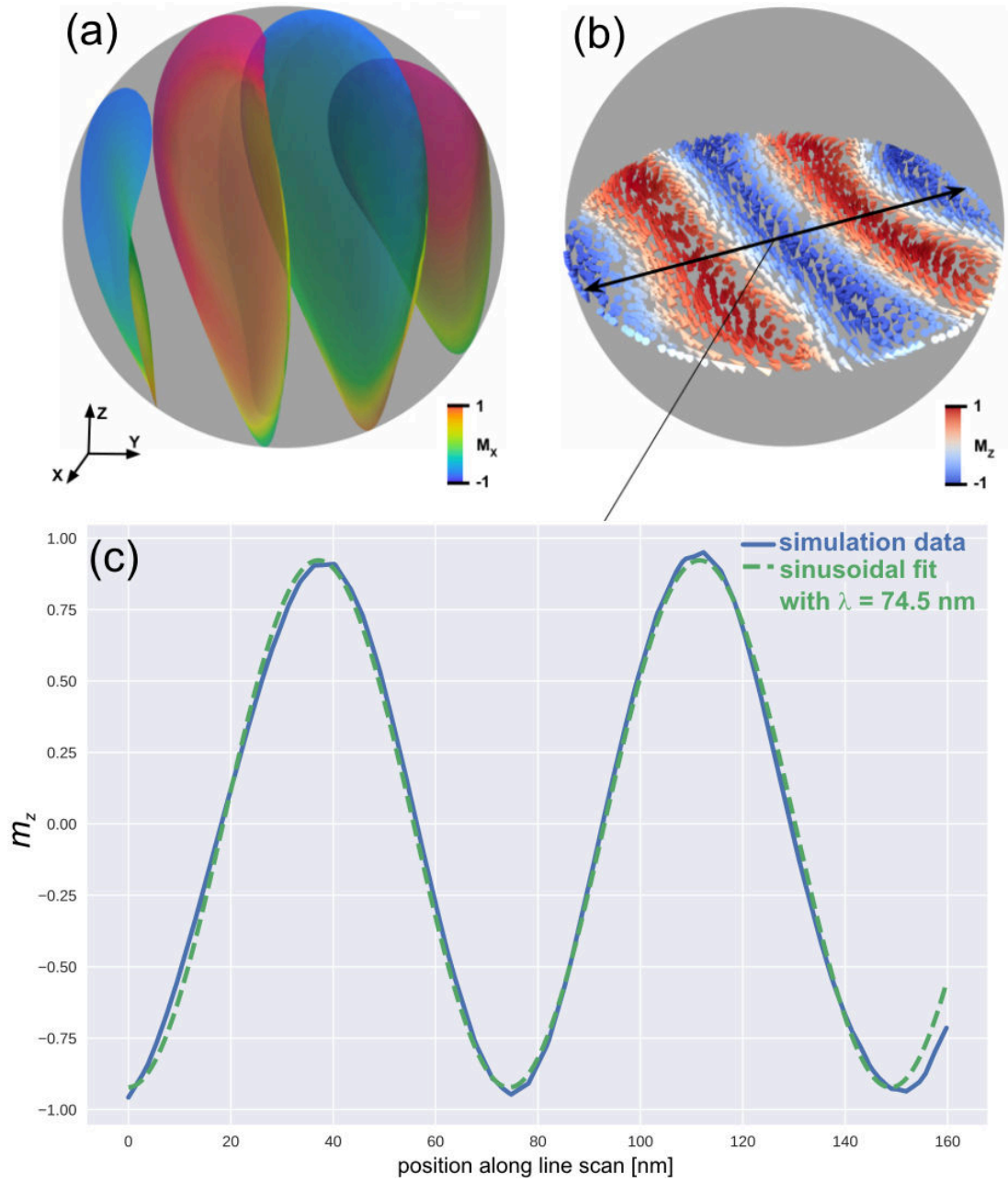


FIGURE 5.1 – Helical state in a $r = 80$ nm FeGe sphere at $H_{\text{ext}} = 10$ mT. The isosurface representation in panel (a) displays the areas where m_z is equal to zero. Panel (b) shows the magnetization configuration on a slice through the equatorial plane, clearly displaying a right-handed magnetization helix. This spin spiral (c) has a wave length of 74.5 nm, which is in good agreement with the analytic long-range helical period of $l_d = 70$ nm of the material.

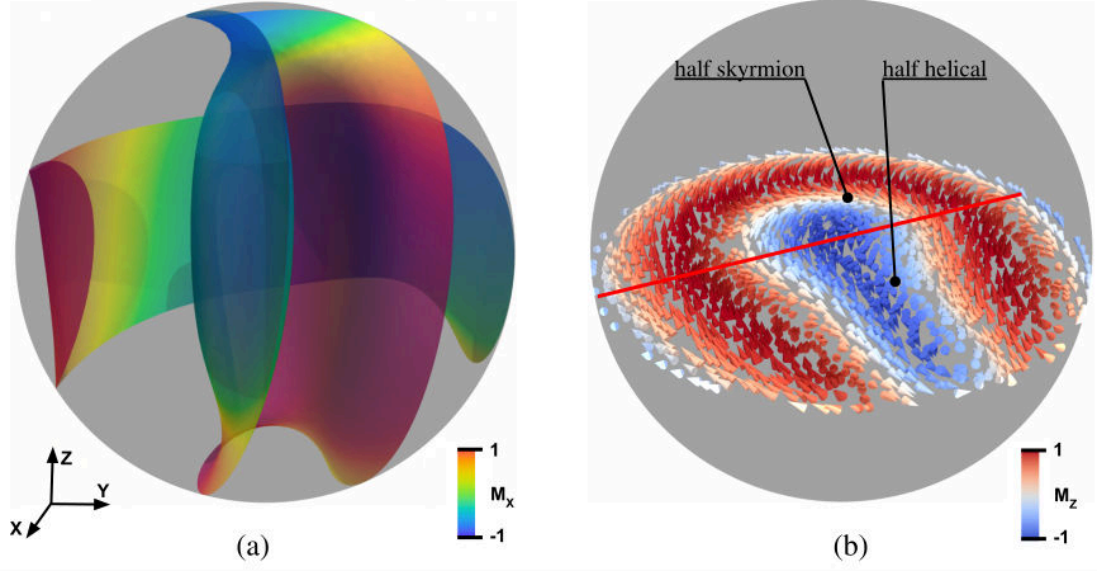


FIGURE 5.2 – Three-dimensional meron structure forming as a magnetic ground state in $r = 70$ nm at $H_{\text{ext}} = 30$ mT. The $m_z = 0$ isosurfaces are shown in (a). When compared with the isosurfaces of the helical state [cf. Fig. 5.1a], one can notice that they display a distinct curvature in the meron state. The magnetization configuration on a central cross-section is shown in panel (b). The state can be interpreted as a combination of a half-helical and half-skyrmion state [cf. Fig. 5.3]

5.1.2 Meron state

Interpreting the helical state as a magnetic structure with narrow, alternating domains is helpful in order to understand the evolution of the structure as the applied field is increased. Magnetic domain structures react to an increase of the external field such that the domains oriented parallel to the field grow in size, at the expense of domains oriented antiparallel to it. The transition from a helical state to a meron state (Fig. 5.2) with increasing external field strength can be interpreted in this sense. The increase of favorably oriented regions is recognizable in the isosurface representation, as the previously almost parallel isosurfaces $m_z = 0$ bend inwards and connect on one side, cf. Fig. 5.4d,e.

This field-induced modification of the ground state structure is consistent with a decrease of the Zeeman energy while allowing the magnetic system to preserve to a

large extent a spiraling magnetic structure on the length scale l_d , as favored by the competition between ferromagnetic exchange and DMI. Note that in ordinary ferromagnets, without DMI, a gradual modification of a periodic domain structure in an increasing external field would occur in a different way, namely by reducing or increasing the distance between neighboring domain walls. Such a domain wall displacement, however, would have a detrimental effect on the periodicity of the spin spirals, and is thus not a viable channel in chiral magnetic materials.

An alternative interpretation of the meron structure consists in considering the magnetization state as a hybrid form of two different chiral structures. More specifically, the magnetization state can be split in two parts (cf. Fig. 5.2b), where one half of the nanosphere appears to preserve the structure of a helical state, while the other part displays the characteristics of a skyrmion, which will be discussed in the following section. In this sense, the meron state can be considered as an intermediate, transitional structure between these two states. Meron structures are known from extended two-dimensional systems. In such thin films, theory predicts that merons are unstable in isolation, and that instead bi-meron states should form [162]. However, here, the finite sample size represents a stabilizing factor. We also note that similar examples of isolated meron states have been reported in rectangular shapes [162] and in disc geometries [191], where the structure was denoted as a “horse-shoe” state, for obvious reasons.

5.1.3 Skyrmion state

Further increasing the external field augments the tendency to expand the regions, or domains, in which the magnetization is aligned along the field direction. This tendency is balanced by the necessity to preserve spin spirals, as required by the interplay of symmetric and antisymmetric exchange. In the isosurface representation, the evolution of a meron state in an increasing external field can be interpreted as a second inwards-bending of the isosurfaces, now connecting the isosurfaces on the opposite side, thereby yielding a circular central core in which the magnetization points opposite to the applied field (Fig. 5.4e,f). The resulting axially symmetric configuration is the skyrmion state.

The isosurface representation allows us to clearly visualize the separation of the central skyrmion core from the bulk (Fig. 5.3a). This central, cylindrical region is sometimes referred to as a *skyrmion tube*, or skyrmion line. The main features of the

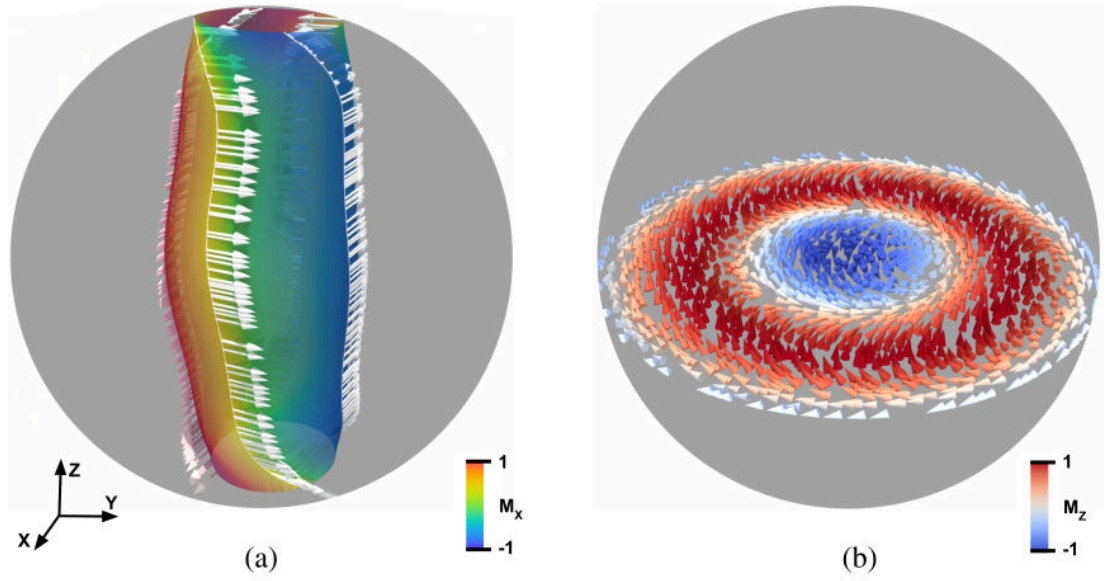


FIGURE 5.3 – A three-dimensional skyrmion structure is the magnetic ground state in $r = 80$ nm at $H_{\text{ext}} = 110$ mT. Panel (a) displays the skyrmion tube in the center, visualized by $m_z = 0$ isosurface. It separates the central core from the surrounding circular structure. The skyrmion tube undergoes a twist at the boundaries. This becomes evident by analyzing the change in the position of the magnetic moments pointing in a particular direction, as we move laterally on the skyrmion tube. The magnetic configuration on a horizontal slice in the middle is shown in panel (b), displaying strong similarities with the well-known magnetization texture of a two-dimensional Bloch skyrmion in thin films.

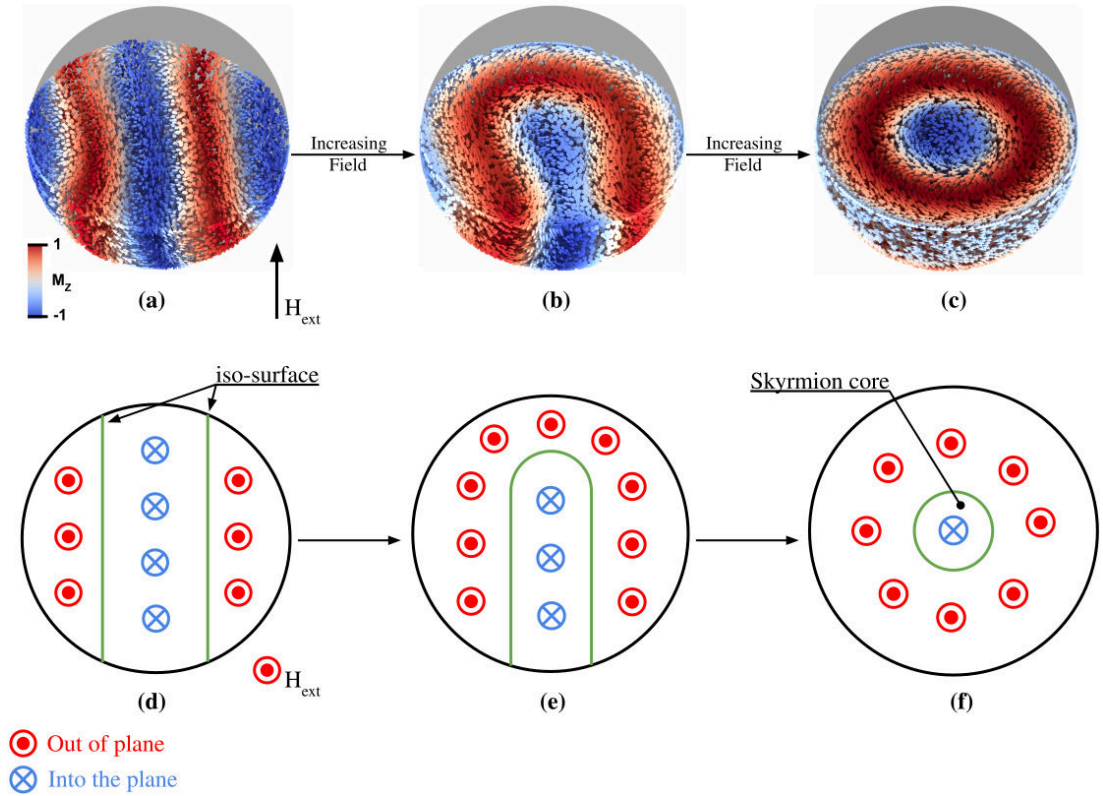


FIGURE 5.4 – Transformation of the magnetic ground state from a helical state (left) into a meron state (middle) towards a skyrmion state (right) as the external field increases. The top row (a), (b), (c) displays simulation results, where the top hemisphere is removed to show the magnetic structure on the central plane. The color code, from blue to red, denotes the magnetization component m_z opposite and along the field direction, respectively. The schematics in the bottom row (d), (e), (f), of the top view, in a simplified way, show the evolution of equilibrium states as the field is increased. The growth of the domains pointing in the direction of the field is not achieved by a reduction of the width of the central domain, but by connecting the iso-surfaces, yielding first the meron state and, at higher fields, the skyrmion state.

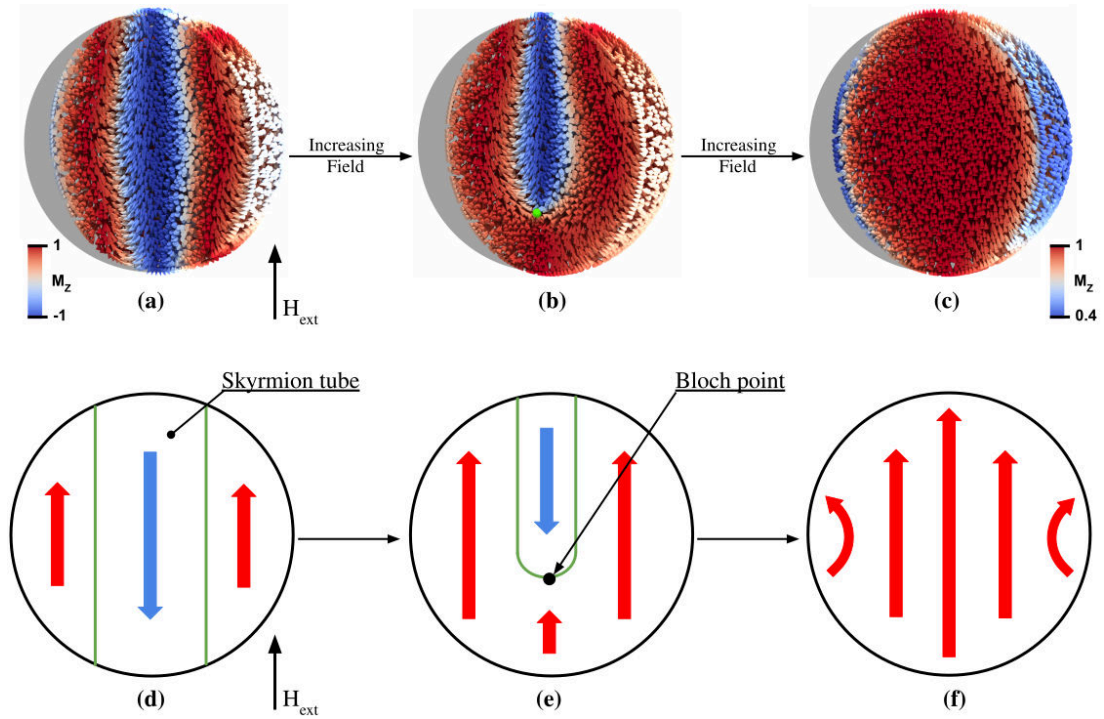


FIGURE 5.5 – With increasing field, the skyrmion state (left) transforms first into the chiral-bobber state (middle), which then further evolves into a quasi-saturation state (right). In the simulated structures (a), (b), (c) half of the sphere has been removed to display the evolution and disappearance of the skyrmion tube in the center of the sample. The red and blue color code refers to the value of the magnetization component m_z along and opposite to the field, respectively. The schematics in the bottom row (d), (e), (f) illustrate how the skyrmion core, representing a nano-domain aligned opposite to the field, shrinks as the external field increases. This central domain first becomes smaller as a Bloch point is injected, yielding the chiral bobber state, then it vanishes completely, resulting in a quasi-saturation state with a DMI-induced twist on the surface.

static configuration are readily recognized by displaying the magnetic configuration on a horizontal slice on the central plane, cf. Fig. 5.3b). The magnetization configuration on the central slice shows obvious similarities with the well-known magnetization texture of a two dimensional Bloch skyrmion in a thin film. However, the 3D structure in the sphere has additional features. For instance, the magnetic structure undergoes a twist along the axial direction, as shown in Fig. 5.3a), to reduce the DMI energy in the nanosphere. A similar behavior was previously reported by Rybakov et al. [46] in the case of thick extended films.

If the external field is further increased, the central core of the skyrmion state pointing in the opposite direction of the field shrinks in size, and the surrounding circular domain oriented along the external field grow. At a certain field, the axially symmetric skyrmion state becomes unstable and transforms into a different magnetization configuration known as a chiral-bobber state [35]. This structure retains to some extent the central skyrmion core, which now however terminates in a Bloch point structure [84, 203] inside the sphere, cf. Fig. 5.5d,e. The chiral-bobber state can thus be regarded as a hybrid state combining skyrmion and Bloch point structure.

5.1.4 Chiral-Bobber state

To further analyze this magnetic configuration, we display in Fig. 5.6b the magnetic structure on two horizontal slices, one above and one below the Bloch point. The configuration on the upper slice resembles that of a skyrmion state, while the one below corresponds to a nearly homogeneous configuration in which the magnetization is largely aligned in the direction of the external field. Chiral-bobber structures have been previously reported, both in theoretical [35] and experimental [37] studies, in thick extended films of non-centrosymmetric ferromagnets. Recently, this magnetization structure has attracted considerable attention as it has been proposed as a candidate for a fundamental unit of information storage, along with the skyrmion state, in future spintronics memory devices [190].

If the external field is further increased, the central core of the chiral-bobber state shrinks in lateral direction until, at a certain field, the Zeeman energy dominates and a quasi-saturated state becomes energetically favorable (Fig. 5.5e,f).

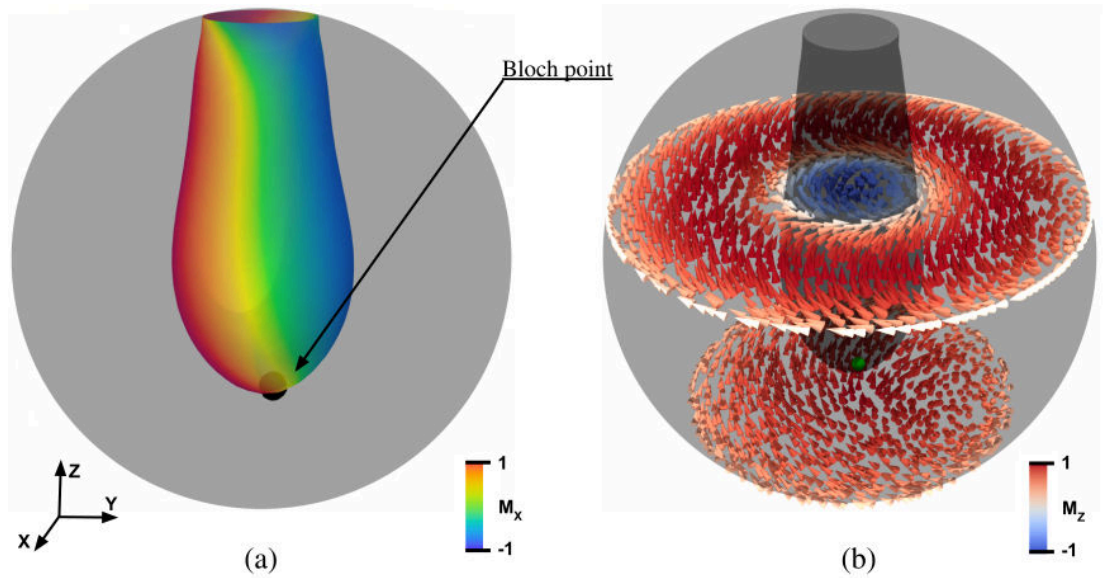


FIGURE 5.6 – The chiral-bobber state shown here at $H_{\text{ext}} = 200$ mT at $r = 80$ nm, is a complex three-dimensional magnetization structure in which a skyrmion tube terminates in a Bloch point. The conical shape of the residual skyrmion core is visualized by the iso-surfaces corresponding to $m_z = 0$, shown in panel (a). The magnetization configuration of two slices, one above and one below the Bloch point is shown in (b). On the slice above the Bloch point the structure is similar to the skyrmion state, while below, the magnetization is almost saturated along the field direction.

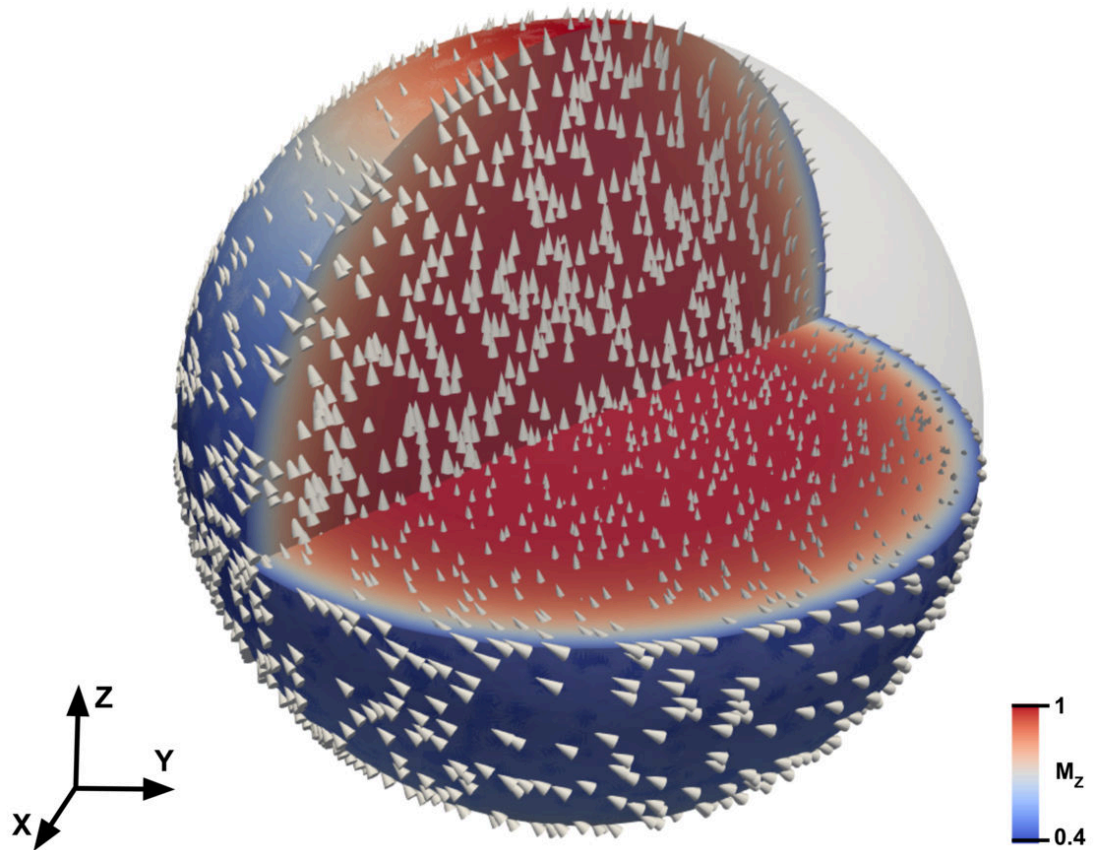


FIGURE 5.7 – Quasi-saturated magnetization state in $r = 80$ nm at $H_{\text{ext}} = 500$ mT. At such high external magnetic field, the Zeeman energy dominates and the bulk of the magnetization is aligned in the direction of the field. However, a rather significant deviation, which is primarily due to the DMI, occurs at the boundary near the equatorial plane.

5.1.5 Saturation state

This relatively simple equilibrium state, which is stable at large fields, is characterized by the bulk of the magnetization pointing along the external magnetic field direction, cf. Fig. 5.7. It resembles an ordinary ferromagnetic saturation state. However, near the surface the magnetization deviates, in particular along the equatorial plane. This deviation is primarily due to the DMI, which tends to preserve a chiral structure as far as possible in the presence of a strong external field. The slight curling of the magnetization induced by the DMI is also favored by magnetostatics as the system thereby reduces the magnetostatic surface charges and forms a weakly developed vortex state. Furthermore, the particle surface plays a particular role in the curling of the magnetization due to specific boundary conditions of the DMI interaction [171],

5.2 Phase diagram

In the previous section, we have identified five principal equilibrium states of the chiral magnetization in a FeGe nanosphere, and described their evolution with increasing external field. The stability of these structures, however, also depends on the particle size. To investigate these dependencies, we have performed numerous additional simulations. The numerical results allow us to determine the stability ranges of the five states, as summarized in the phase diagram shown in Fig. 5.8. The diagram displays the lowest-energy configuration as a function of the external magnetic field and the radius of the nanospheres.

Remarkably, the skyrmion phase does not exist in FeGe nanospheres below the radius of 65 nm. This size is comparable to the long-range helical period l_d (70 nm) of the material, which in turn signifies one full rotation of the magnetization. Although there is no direct connection between the structure a spin spiral and the skyrmion state, it is intuitively clear that the sample cannot host a skyrmion structure if it is too small to accommodate two full rotations of the magnetization across the diameter of the sphere. This trend of disappearing phases continues as we further decrease the radius. Below the radius of 50 nm, the chiral-bobber and meron phase also cease to exist. At this size, the nanosphere diameter approaches l_d , and hence, only the helical phase (at lower external fields) and the saturation phase (at higher external fields) are stable. For radii smaller than 40 nm, only the saturation phase remains as the particle

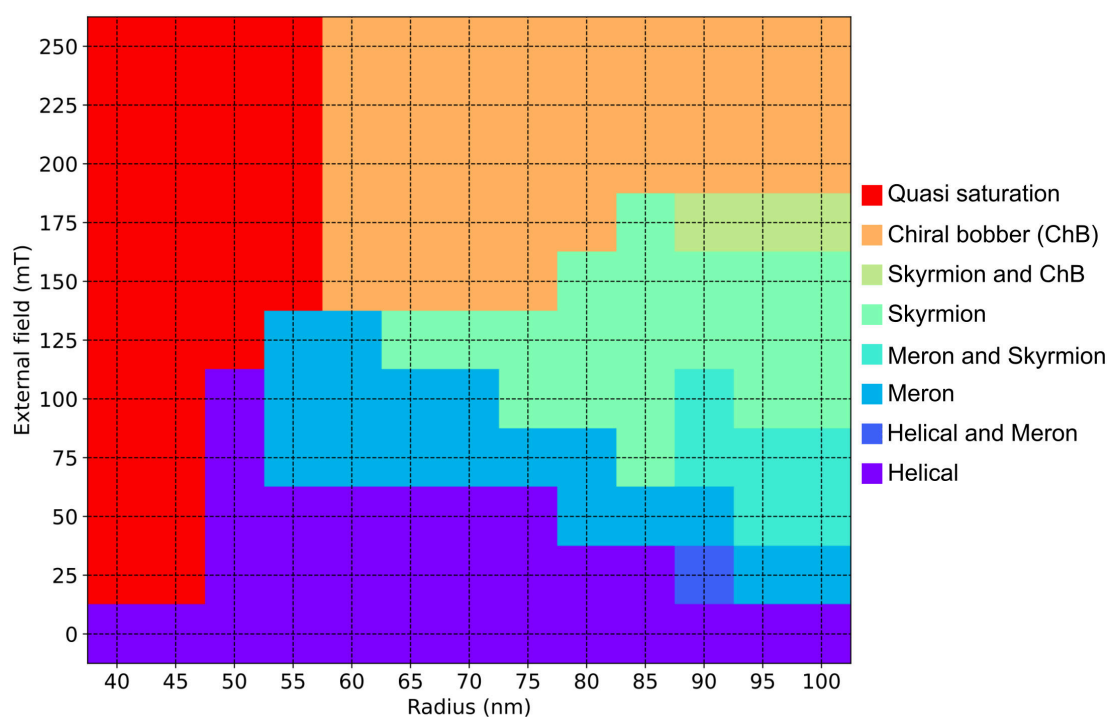


FIGURE 5.8 – Phase diagram of the magnetic ground state of a FeGe nanosphere as a function of the external magnetic field in mT and the radius in nm. The different regions outline the parameter ranges in which respective magnetization states represent the lowest-energy configuration.

5.3 Phase diagram cross-sections : energy densities of stable and meta-stable states

size falls below l_d , leaving no room for even one full rotation of the magnetization.

A clear distinction of the five principal configurations mentioned above is only possible in particle sizes up to a radius of about 90 nm. In larger nanospheres, hybrid structures appear, which can contain, *e.g.*, both a meron and skyrmion structure, or a skyrmion as well as a chiral-bobber. At these larger sizes, the impact of the particle's spherical shape on the magnetic structure diminishes and one observes a gradual transition towards a quasi-continuum of three-dimensional chiral magnetization states, as it would occur in bulk material.

5.3 Phase diagram cross-sections : energy densities of stable and meta-stable states

We plot the total energy densities of the equilibrium states : helical, meron, skyrmion, chiral bobber, and saturation state in a sphere of radius 70 nm with a changing external magnetic field (Fig. 5.9) and at constant external field of strength 125 mT with changing radius (Fig. 5.10). The equilibrium state with the least energy density represents the ground state, as presented in the phase diagram (Fig. 5.8). The total energy density plots help us understand the energy landscape and meta-stability of different equilibrium states with respect to the external magnetic field and nanosphere radius. In general, the energy density of all the states decrease with increasing external field, which points towards a vital role of Zeeman energy. In the case of changing radius at constant external field, the energy densities increase with increasing radius. This points towards the fact that the stability of a particular equilibrium state depends on both external field as well as the material geometry. One can argue that the change in energy density is due to a modification of the equilibrium states' magnetization structure with changing external field and nanosphere radius (even though the salient features remain the same). This phenomenon is well studied for skyrmion crystals [204–206] and geometrically confined skyrmions [47].

First we study the energy density variation of the equilibrium states at constant radius 70 nm. The helical state is the ground state for an external field of 0 mT to 62.5 mT. We interpolate between the two data-points at 50 mT and 75 mT that the helical state is the ground state for the first half and the meron state for the second half. Similarly, the meron state becomes the ground state for the field range from

5.3 Phase diagram cross-sections : energy densities of stable and meta-stable states

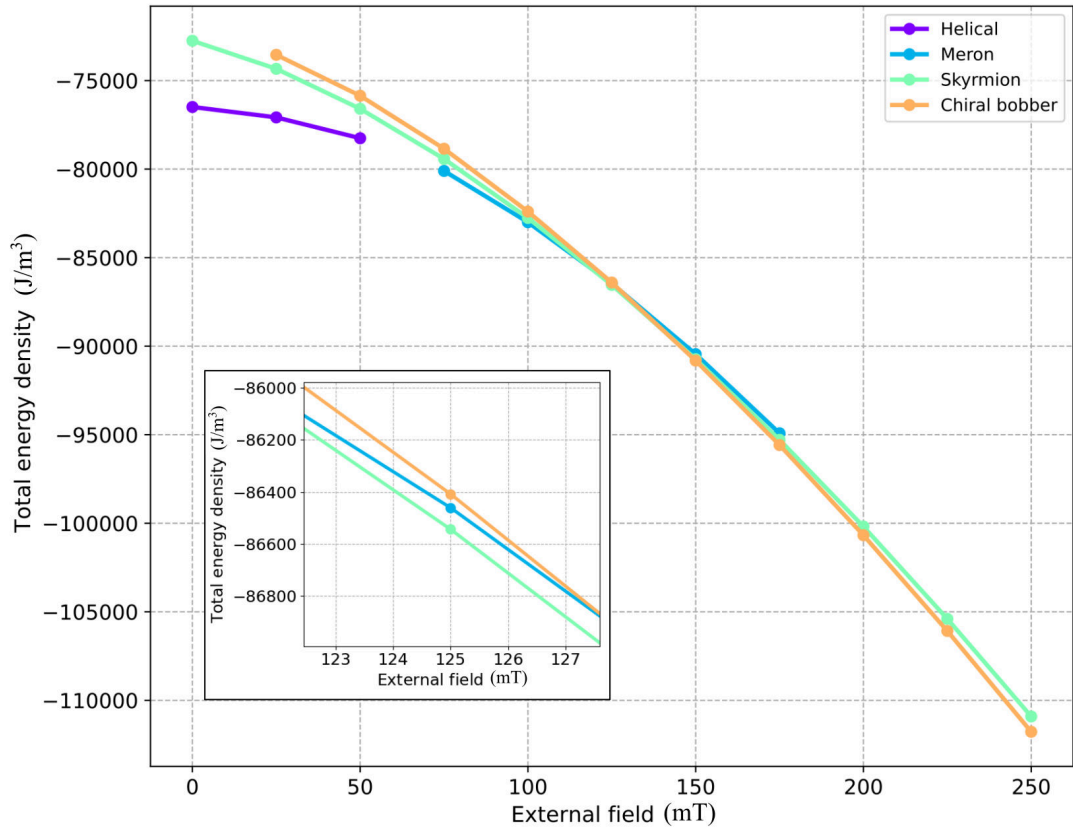


FIGURE 5.9 – Energy density of helical, meron, skymion and chiral bobber states in a sphere of radius 70 nm within a field range from 0 mT to 250 mT. The respective ground states is the configuration with the lowest energy density at a give external field (in accordance to Fig. 5.8). Moreover, it shows the meta-stability of the equilibrium magnetization states with changing field. In particular, we note that the magnetization states with non-trivial topology (skymion, chiral bobber, and meron) show meta-stability with skymion states spanning across the field range.

5.3 Phase diagram cross-sections : energy densities of stable and meta-stable states

62.5 mT to 112.5 mT. The skyrmion state becomes the ground state from 112.5 mT to 137.5 mT, and the chiral bobber state from 137.5 mT to 262.5 mT. Further, to explore the meta-stability of the four equilibrium states, we perform simulations, with each equilibrium state as a starting configuration, to obtain a final stable configuration by systematically changing the external field values from 0 mT to 250 mT. We plot the results of the simulations in Fig. 5.9.

We observe that the skyrmion state and the chiral bobber state can be (meta-)stable over a wide range of external magnetic fields. To be precise, the skyrmion state remains stable for the whole field range. One can ascribe this increased (meta-)stability to the non-trivial topology of the skyrmions. Once formed in the material, a skyrmion can only be removed by pushing it out of the material boundary or with the help of a Bloch point; both of which presents an energy barrier. A similar argument is valid for the chiral bobber state; however, at zero external magnetic field, the chiral bobber state denucleates through the Bloch point, first into a quasi-saturation and finally into a helical state. The meron state is also obtained as a meta-stable state for a field range of 75 mT beyond 112.5 mT. However, it is not stable below the field range, where it is the ground state. It is important to note that the meron state also has a non-trivial topology with a skyrmion number $|Q| = 1/2$. In contrast, the helical state, which has a trivial topology, is only stable as a ground state.

Fig. 5.10 shows the energy densities of the equilibrium states at a constant external field of strength 125 mT with changing radius from 40 nm to 100 nm. The quasi-saturation state is the ground state from radius 40 nm to 52.5 nm, the meron state from 52.5 nm to 60 nm, and the skyrmion state from 60 nm to 100 nm. The chiral bobber state is not a ground state for any radius at 125 mT, however it can form as a meta-stable state over a long range of radius values from 50 nm to 85 nm. For the case of helical state, we find that it is neither a ground state, nor a meta-stable state at 125 mT.

Focusing on the field value of 125 mT (inset Fig. 5.9), we obtain the skyrmion, the chiral bobber, and the meron state with relatively close energy density values, with the skyrmion state being the ground state. Even though the energy densities of the ground and the meta-stable states are close, each state is separated by an energy barrier due to its unique topology. The skyrmion state and the chiral bobber state has the important difference of a Bloch point, while the meron state and the skyrmion state have different skyrmion numbers Q . This can be potentially useful for memory device applications as

5.3 Phase diagram cross-sections : energy densities of stable and meta-stable states

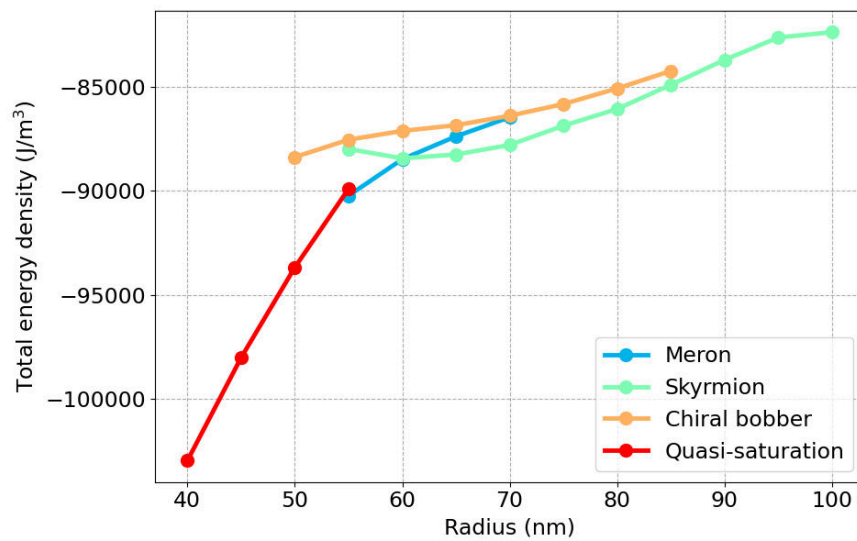


FIGURE 5.10 – The total energy densities of quasi-saturation, meron, skyrmion, and the chiral bobber states at a constant external field of strength 125 mT for nanosphere radius range 40 nm to 100 nm. The energy difference between the equilibrium states shows that several states can be meta-stable. The ground state is defined as the stable state with the lowest energy.

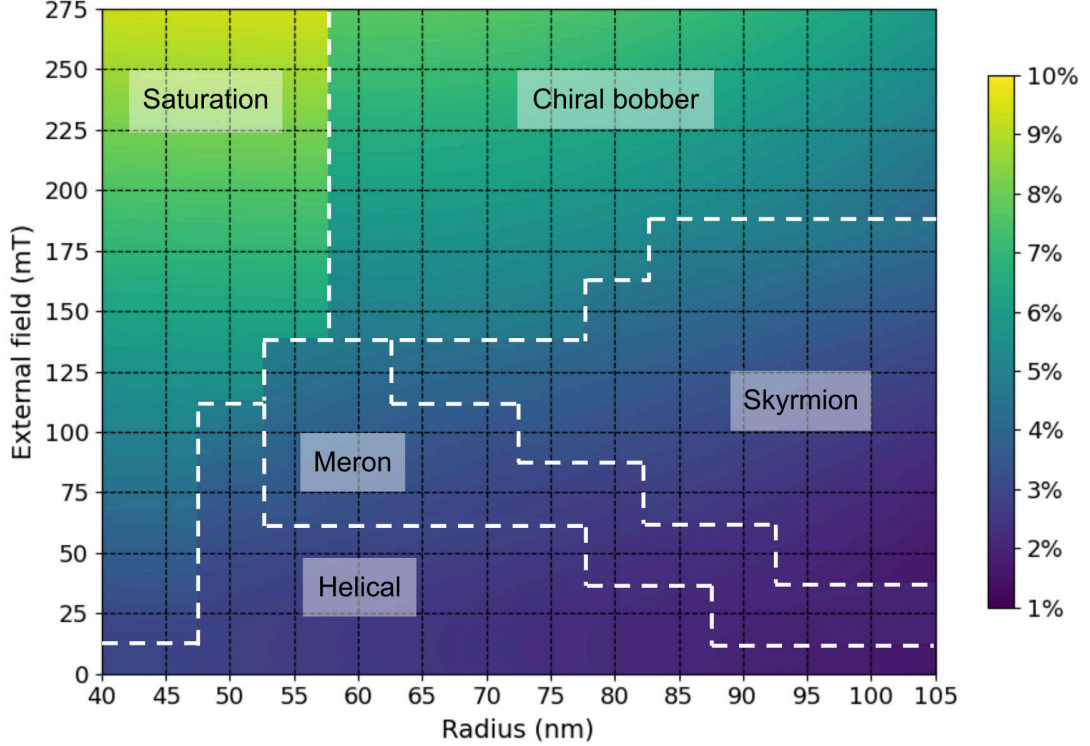


FIGURE 5.11 – Demagnetization energy as a percentage of the total energy for different magnetic ground states in the phase diagram. In all cases the maximum value remains below 10% through out the phases. The percentage increases only slightly towards the regions of small radius and high fields, where the nanosphere are in the saturation phase.

the contemporary magnetic memory devices store information in magnetization states of nanomagnets with comparable energy separated by a sufficiently high energy barrier.

5.4 Impact of magnetostatic interactions

Having described the various magnetic structure and their formation resulting from the competing interactions of Zeeman energy, ferromagnetic exchange and DMI, we now discuss the impact of the dipolar (magnetostatic) field on these configurations and their distribution. To illustrate the quantitative impact of the dipolar magnetic field, Fig. 5.11 displays the demagnetization energy as a percentage of the total energy for

respective equilibrium states.

It is well known that, in the case of ordinary ferromagnets, the magnetostatic interaction has a decisive impact on the formation of inhomogeneous magnetic structures. The size-dependent equilibrium structure in ordinary ferromagnetic nanoparticles is primarily determined by the balance of the competing interaction of the magnetostatic energy favoring flux-closure states and the ferromagnetic exchange that tends to prevent inhomogeneities of the magnetization. The equilibrium structure is also impacted by the strength of an external magnetic field, and thus the field- and size-dependent distribution of magnetic states in nanoparticles is commonly summarized in phase diagrams similar to ours [192]. However, in our case, the competition is primarily driven, on one side, by the tendency to align the magnetization along the external field direction and, on the other side, by the material's tendency to develop spiralling magnetization structures on the length scale l_d , which in turn is the result of a balance between the ferromagnetic and the antisymmetric exchange interaction. In this latter case, the role of the demagnetizing field is not clear, and it is in fact often neglected in simulations of chiral magnetization structures.

To analyze the impact of magnetostatic interactions on these configurations and distribution, we recalculated the phase diagram by excluding the demagnetization field and energy density from the simulation. Remarkably, we found that this does not alter the results appreciably, yielding in fact essentially the same phase diagram (not shown). This is consistent with the observation that relative impact of the demagnetization energy, displayed in Fig. 5.11 as the percentage of total energy, is relatively small for all equilibrium states. The demagnetization energy does not exceed 10 % of the total energy for any of the states. This indicates that, although not strictly negligible, magnetostatic interactions do not play a dominant role in the equilibrium state configuration and distribution. The demagnetization energy becomes only sizable in the upper left part of the plot, *i.e.*, towards small radius sizes and high fields, where the particles are in a quasi-saturation state. In the other equilibrium states, the DMI-induced helical nature of the magnetization structures already reduces the magnetostatic energy by forming states similar to periodically alternating domains, or swirling patterns. The balance between ferromagnetic exchange and DMI thus leads to the formation of magnetic structures which provide a fair amount of magnetic flux closure, so that the demagnetizing energy of the DMI-induced structures remains relatively low. Dipolar

5.4 Impact of magnetostatic interactions

fields therefore do not have a decisive impact on helical or chiral magnetization structures. In conclusion, our results indicate that neglecting the magnetostatic interaction is a perfectly acceptable approximation in the simulation of magnetic materials with strong DMI, at least in the case of three-dimensional nanoparticles. This is not necessarily true for flat and thin geometries, where demagnetizing fields generally play a larger role, and where the magnetic surface charges generated by chiral structures have a stronger impact on the total demagnetizing energy. Moreover, the reduced dimensionality of thin films may lower the degree by which chiral or helical magnetization states can achieve a partial magnetic flux-closure.

CHAPITRE 6

Skyrmion-chiral bobber state switching

In section 5.1, we discussed the different equilibrium magnetization states stabilized in FeGe nanospheres. We argued how different equilibrium states become the ground state with an increasing external magnetic field (Fig. 5.4 and Fig. 5.5). However, the description only explains why a particular equilibrium state is the ground state at a given external magnetic field and the nanosphere radius. It does not provide a mechanism to transition from one state to the other.

Recently, both skyrmion and chiral bobber (ChB) have been proposed to be the fundamental information storage units in a novel non-volatile racetrack memory device. They have been shown to co-exist and have different magnetotransport fingerprints [37], strengthening their case for application in a memory device. Here, we discuss a mechanism to switch between a skyrmion and a ChB state in a FeGe disc geometry by means of an external field pulse.

Based on our FeGe nanosphere study (Section 5), we understand that the total energy of these states depends on the external magnetic field for a particular material geometry. It can be explained better with a phase diagram depicting the distribution of these states with changing geometrical size and constant external magnetic field. By changing the field appropriately, we switch the energetically preferred states (i.e., skyrmion and ChB) and facilitate the transition. We also require an external field pulse and the change in the constant external field to overcome the energy barrier to switch from one state to the other.

The skyrmion to ChB switching is studied in a FeGe disc of radius 80 nm and thickness 70 nm. First, we stabilize the skyrmion state by applying a constant external magnetic field of strength 190 mT in the positive z -direction. The skyrmion state is the ground state at this field value (and ChB state is a meta-stable equilibrium state). We increase the external field to 220 mT from 190 mT, modifying the difference between the total energies of the two states. From section 5.3, we argue that with increasing external field, this difference between the total energies of the states decreases. Although the two states' total energy difference has changed, the actual switching from skyrmion to the ChB state requires overcoming an energy barrier (as the ChB state hosts a Bloch point). We apply a Gaussian field pulse of strength 350 mT and width 235 ps in the positive y -direction to achieve this. The application of an external field pulse nucleates a Bloch Point at the top surface of the skyrmion state, ultimately converging to the ChB state (Fig. 6.1). Similarly, reversing the process returns the system to the

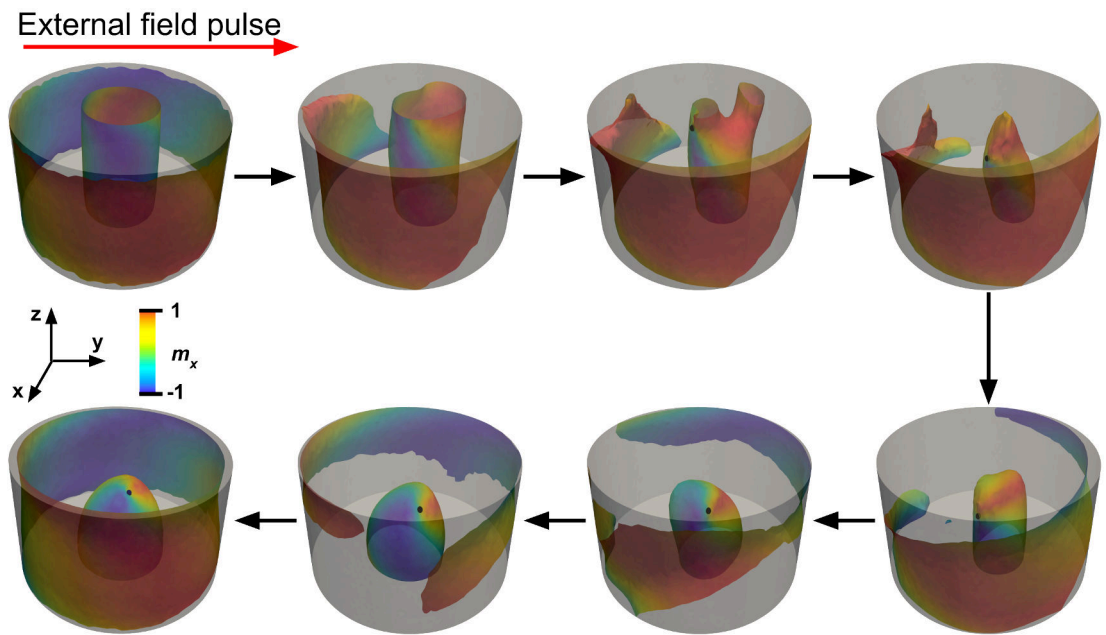


FIGURE 6.1 – The figure shows snapshots in time of skyrmion to ChB switching with a constant external field of strength 220 mT in $+z$ -direction. The first magnetization state, on the top left, shows the skyrmion state. A black dot represents the Bloch point nucleated in the switching process. We apply a Gaussian field pulse of strength 350 mT and width 235 ps in $+y$ -direction. The magnetization state's evolution that follows is shown in the snapshots (following the arrows chronologically).

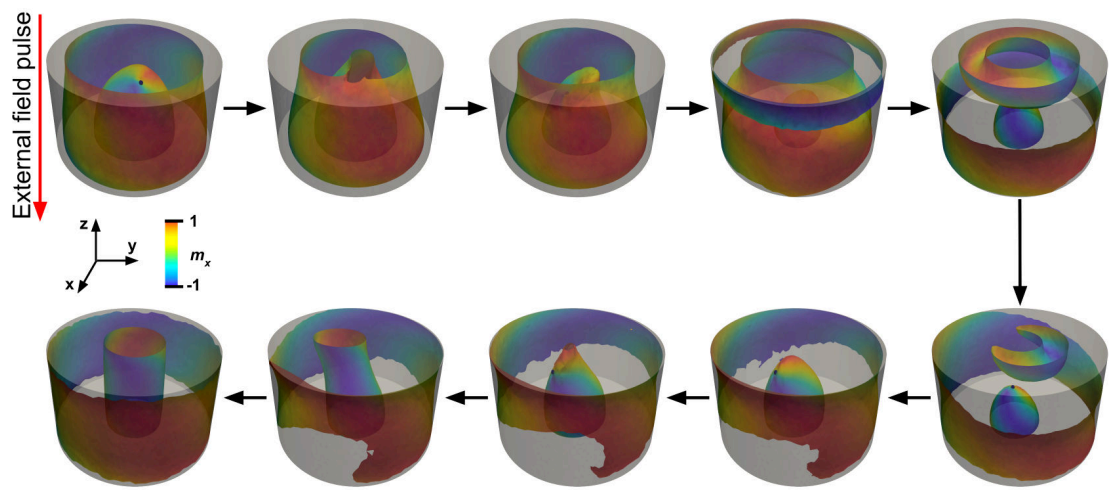


FIGURE 6.2 – The figure shows snapshots in time of ChB to skyrmion state switching with a constant external field of strength 190 mT in $+z$ -direction. The first magnetization state, on the top left, shows the meta-stable ChB state. A black dot represents the corresponding Bloch point. We apply a Gaussian field pulse of strength 350 mT and width 150 ps in $-z$ -direction. The magnetization state's evolution that follows is shown in the snapshots (following the arrows chronologically).

skyrmion state. First, we reduce the external magnetic field to 190 mT from 220 mT. Then, we apply a Gaussian field pulse of strength 350 mT and width 150 ps, in negative z -direction (Fig. 6.2), to overcome the energy barrier. In this way, we can cycle between the skyrmion and the ChB state by first changing the two states' total energy difference with a constant external field and finally overcoming the barrier leading to the switching with an external field pulse. Interestingly, the Bloch Point always nucleates at the top surface of the disc geometry in the ChB state for all the simulations carried out in an above-described manner. Investigating this further, we find two principal reasons for the breaking of symmetry ; first, the direction of the external magnetic field used to stabilize the states, and second, the sign of DMI constant, which determines the handedness of the chiral magnetization structures observed in the material. Reversing the direction of the external magnetic field reverses the direction of the skyrmion core, and indeed we find that the Bloch point now nucleates from the bottom surface. Changing the sign of the DMI constant (i.e., from positive to negative) changes the handedness of the skyrmion and the ChB state from right-handed to left-handed. Interestingly, we find that, here as well, the Bloch point nucleates from the bottom surface. We observe that the two Bloch points that form at the top and the bottom surface have different polarities and similar vorticity. Whether the polarity influences the energetics and, hence, leads to the Bloch point's preferred nucleation remains to be further investigated.

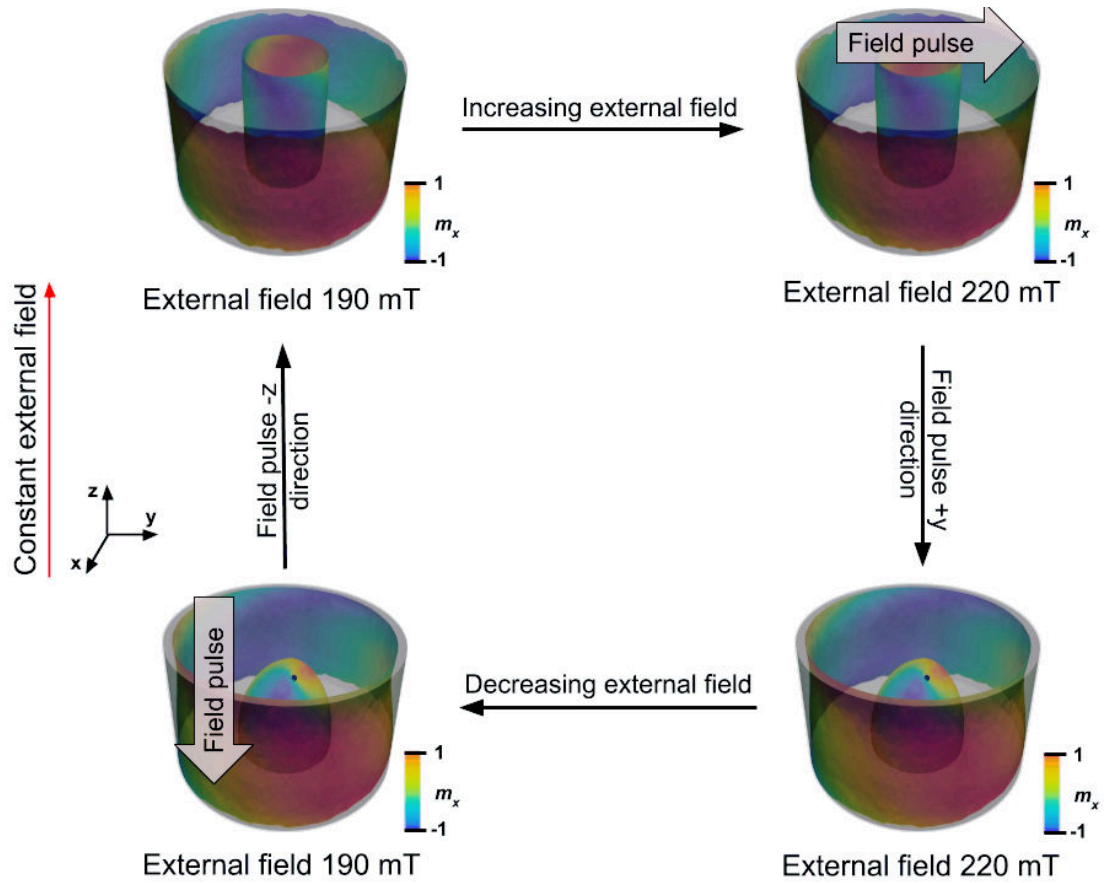


FIGURE 6.3 – The figure shows a graphical representation of the switching cycle between skyrmion and ChB state. Starting from the skyrmion state on the top left, we increase the external field to 220 mT. With the help of a field pulse in $+y$ -direction, we switch to the ChB state (bottom right). Similarly, to return to the skyrmion state, we reverse the process. We decrease the field to 190 mT (bottom left) and apply a field pulse in $-z$ -direction to switch to the skyrmion state (top left).

CHAPITRE 7

Geometric Skyrmion Confinement

The phase diagram for the nanospheres (Section 5.2), as well as, similar studies on the thin-film geometry ferromagnets with broken spatial inversion symmetry [5, 36, 44–47] reveal the dependence of three-dimensional skyrmion state stability on both the external magnetic field and the geometric dimensions of the material (radius in the case of the nanospheres). Thus, one can argue that it is possible to create desired regions of skyrmion stability by modulating the thickness of the material at a given external magnetic field. These regions of stability will act as a potential well for the skyrmions yielding control over their position in both static and dynamic cases.

Skyrmions have been proposed to be a great candidates for device applications like non-volatile racetrack memory [7, 207], RF applications [208, 209], and recently, skyrmion based neuromorphic computing [210]. Much of this interest owes to their unique properties such as topology stability [128], reduced size (sometimes comparable to atomic scale) [3], room temperature availability [4–6], and desirable dynamic properties (small depinning current density) [2]. However, to achieve comprehensive integration of skyrmions in a device, it is imperative to attain control over their position and motion. One can achieve this by constraining skyrmions to a desired region of the material geometry.

Here, we show a way to manipulate the position of the skyrmions by modulating the thickness of the material geometry. We start by simulating rectangular thin films of FeGe with changing thickness and external magnetic field, keeping the lateral dimensions of the films constant. The simulation results help us plot a phase diagram showing the magnetization ground state distribution (similar to the nanosphere study in section 5.2) and the total energy density of the skyrmion and saturation state with changing film thickness at constant external field. The focus of the study is primarily the skyrmion state and the saturation state. The goal is to modulate the thickness of the film in a way such that the skyrmion state is energetically favorable for the desired region of confinement, and the saturation state elsewhere in the geometry, at a fixed external magnetic field. To refine our understanding of skyrmion stability, we also plot DMI as a percentage of total energy. DMI favors the formation of skyrmions and the percentage DMI plot reveals skyrmion stability within the skyrmion phase. Using the results obtained from the above-mentioned plots, we generate preferential sites for skyrmions in the material by introducing dot-like *pockets* of reduced film thickness. We show that these pockets can serve as pinning centers for the skyrmions, thus trapping

or constraining skyrmions. Further, using the same results, we show static skyrmion confinement in three example geometries. The example geometries comprise of films of FeGe with a thin path carved out of them, which is the desired region of skyrmion confinement. We simulate a linear path, an angular, and a curved path to emphasize the fact that skyrmions stay confined irrespective of the complexity of the shape of the desired region. As described earlier, the thickness modulation in the material, at a given external magnetic field, creates a potential well which traps the skyrmions, and hence, they stay confined to a particular region of the geometry. We calculate the energy barrier profile of the potential well at a given external field in the linear path geometry by artificially pinning the magnetization configuration of a skyrmion across the thickness modulation. We calculate the total energy by relaxing the magnetization configuration of the pinned skyrmion at each position (Section 7.3). A similar plot is obtained for the rectangular geometry with uniform thickness, for comparison. Further, we show dynamic skyrmion confinement in a novel *H-shaped* racetrack geometry, inspired from static skyrmion confinement, where thickness barriers at the lateral edges of a thin central track (desired region of skyrmion confinement) counter the unwanted skyrmion Hall effect in the presence of an electric current. Also, we show that the motion of the skyrmion on the H-track can be explained with Thiele equation. Extending the study of dynamic skyrmion confinement, we show how it affects the magnetization modes of an isolated skyrmion in a nanodisc geometry by comparing with already published studies of skyrmion magnetization modes in a confined geometry. Hence, we present a comprehensive study of geometrical skyrmion confinement starting with the skyrmion stabilization in a desired region of the material geometry statically, and calculation of the energy barrier for the skyrmion due to the thickness modulation. Then, we show how it affects the dynamical modes of a confined skyrmions and utilize it to counter skyrmion Hall effect in a modified racetrack geometry.

7.1 Statically constrained skyrmions

The material geometry under investigation is a rectangular FeGe film with lateral dimensions $180 \text{ nm} \times 310 \text{ nm}$. For plotting the phase diagram for ground state distribution, we consider films of uniform thickness, where the thickness varies from 5 nm to 75 nm in an increment of 5 nm. Similarly, the external magnetic field varies from 0 mT to 900 mT in an increment of 50 mT. We also plot the percentage energy contribution of

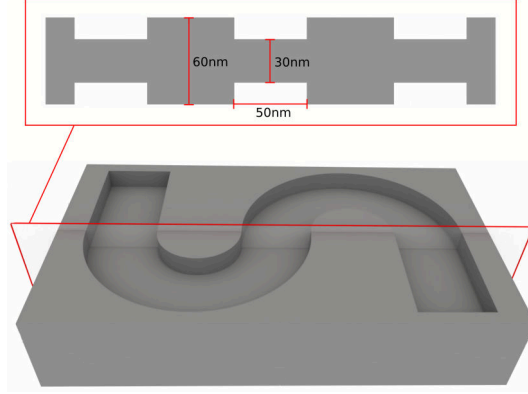


FIGURE 7.1 – The image shows the cross-section of the curved path, one of the three example geometries for skyrmion confinement. The thickness of the path is 30 nm, while the thickness everywhere else is 60 nm. The width of the path is 50 nm. These dimensions stay the same for all the example geometries.

DMI to the total energy for skyrmion and saturation state as obtained from the phase diagram.

For static skyrmion confinement, we first consider different arrangements of circular pockets of reduced thickness in FeGe films. The film thickness corresponding to the pockets is 30 nm, while it is 60 nm everywhere else. Second, we consider three example geometries, each with a different shaped thin path (linear, angular, and curved shaped path) carved out of FeGe films of uniform thickness (curved path as shown in Fig. 7.1). Similar to the pockets, the thickness of the path is 30 nm, while the rest of the film thickness is 60 nm for all three example geometries. The external magnetic field is kept constant at 650 mT to obtain a stable magnetization configuration in all the cases.

7.1.1 Equilibrium magnetization states

We obtain four primary magnetization states : helical, bimeron, skyrmion, and saturation state (not shown), as displayed in Fig. 7.2. The intermediate states, where the magnetization configuration these primary states intermixes to give helical-bimeron, bimeron-skyrmion, and skyrmion-chiral bobber states, are also presented in Fig. 7.2. Hence, one observes a gradual transition of one magnetization ground state to the other with respect to a changing external magnetic field on the phase diagram, presented in section 7.1.2. The external magnetic field points in the negative z -direction. To illus-

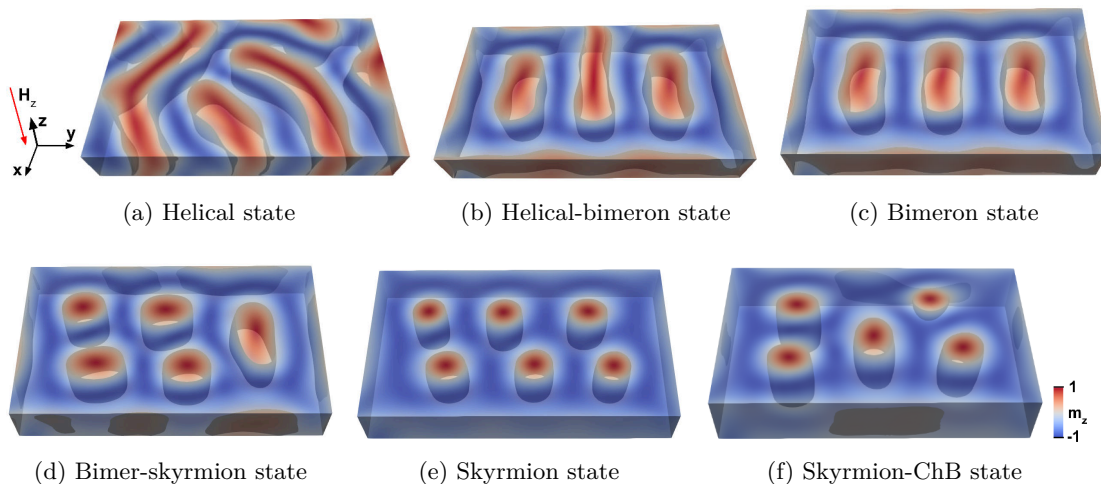


FIGURE 7.2 – The image shows iso-surface ($m_z = 0$) representation of different equilibrium magnetization states obtained in an FeGe film of lateral dimensions $180 \text{ nm} \times 310 \text{ nm}$. The thickness of the film varies from 5 nm to 75 nm and the external magnetic field varies from 0 mT to 900 mT . We plot the corresponding phase diagram of these as the ground states, shown in Fig. 7.3.

trate the magnetization configurations of the equilibrium states, we use a color-coded representation of the z -component of the magnetization (m_z) and the iso-surfaces corresponding to $m_z = 0$ (Fig. 7.2). Crudely, one can argue that the iso-surfaces corresponding to $m_z = 0$ represent a Bloch wall separating the magnetization regions, pointing parallel and anti-parallel to the direction of the external magnetic field, capturing the essence of the chiral magnetization configurations.

We briefly describe the magnetization configurations of the primary equilibrium states, which bear similarities with the ones obtained in the study of FeGe nanosphere presented in section 5.1. The description follows the order of equilibrium states obtained as the ground states with increasing external magnetic field. First, at lower external fields, we obtain the helical state as the ground state. This state comprises of chiral magnetization helices formed due to competing symmetric ferromagnetic exchange and anti-symmetric DMI. The handedness of the helices depends on the DMI present in the material. The propagation vector of the helices in the helical state is always in the plane perpendicular to the external field direction. Fig. 7.2(a) shows the iso-surface representation of the helical state depicting the alternating domains, with respect to

the external field, manifested due to the rotating magnetization of the helices. With an increasing external field, the magnetization regions pointing in the external field's direction expand and stabilize the bimeron state, shown in Fig. 7.2(c). The bimeron state is similar to an elongated skyrmion state, where the two semicircles at the ends represent two halves of a skyrmion while the central strip connecting the halves represents a helical state. We obtained a meron state in the FeGe nanosphere study (section 5.1.2), instead of a bimeron state, as one of the equilibrium states due to the finite size of the nanosphere geometry. In general, for sufficiently large geometries, the bimeron state is more stable [162]. The bimeron has a non-trivial topology with skyrmion number $|Q| = 1$, the same as a skyrmion. Increasing the external field further, one obtains the skyrmion state as the ground state, as shown in Fig. 7.2(e). The skyrmion state forms a triangular/hexagonal lattice arrangement, also known as a skyrmion crystal. In the iso-surface representation, a three-dimensional skyrmion depicts a tubular structure where the iso-surfaces separate the skyrmion cores pointing in the opposite direction of the external field. It is a well-known that the skyrmion magnetization configuration has a non-trivial topology with skyrmion number $|Q| = 1$. Hence, it cannot be continuously unwound into a saturated state, giving it topological stability. Even though we focus on the skyrmion and the saturated ground states for the static skyrmion confinement, the meta-stable skyrmion state may exist for a wide range of external field and film thickness due to topological stability. In films with thickness greater than or equal to 60 nm, another magnetization configuration mixes with the skyrmion state, namely the chiral bobber (ChB) state. ChB state resembles a three-dimensional skyrmion state; however, it terminates in a Bloch point at one end. The skyrmion-ChB state (Fig. 7.2(f)) is the ground state at higher external magnetic fields and film thickness. It has been reported that the stability of the three-dimensional skyrmions decreases with increasing field and film thickness compared to the ChB state [35]. We find similar results in the FeGe nanosphere study presented in section 5.3 and section 5.2. Finally, at critically high external field values, one obtains the saturation state (not shown). This state's magnetization configuration is mainly oriented in field direction, except at the material boundaries due to stray fields and DMI [171].

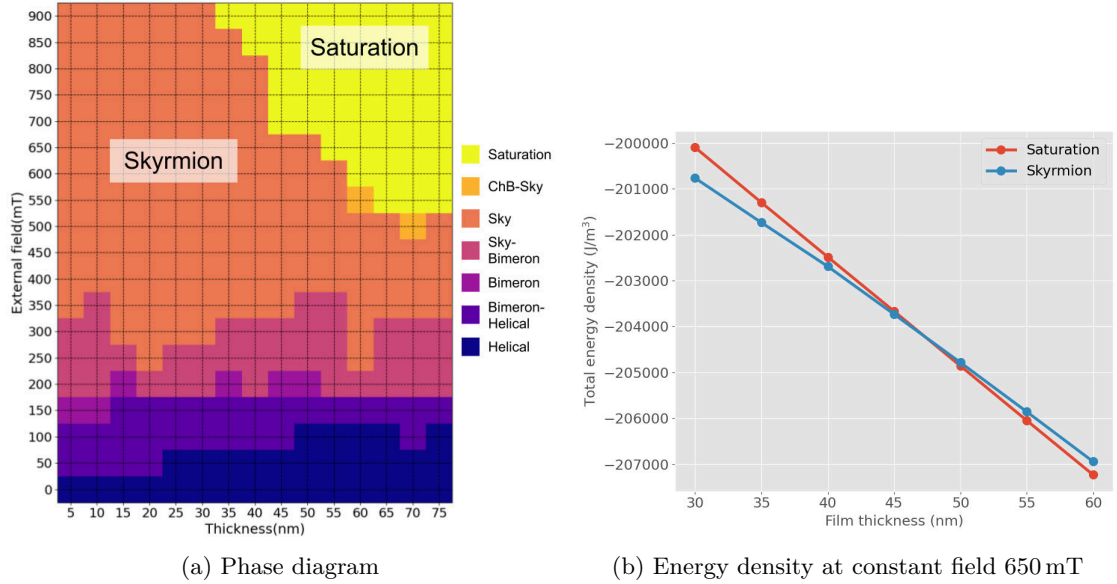


FIGURE 7.3 – (a) The phase diagram of a rectangular FeGe film of lateral dimensions $180 \text{ nm} \times 310 \text{ nm}$ with changing film thickness and external magnetic field. The regions of the diagram represent different equilibrium magnetization states. The primary states obtained are helical, bimeron, skyrmion and saturation state. However, the transition from one state to another is gradual with mixing of the states. We also observe chiral-bobber mixed with skyrmion state at higher film thickness and external field. (b) The plot shows total energy density of the skyrmion and saturation state at 650 mT with changing film thickness from 30 nm to 60 nm . The plot highlights the dependence of skyrmions on the film thickness which is later utilized to constrain and confine them.

7.1.2 Phase diagram

The phase diagram as a function of the external magnetic field and film thickness of an infinitely extended homogeneous FeGe film has been studied theoretically and experimentally, as discussed in the chapter 3. However, Important changes in the phase diagram appear if the dimensions of the material geometry are comparable to the size of a few skyrmions (as in this study). Thus, we plot the phase diagram to identify magnetic ground state distribution for the geometry at hand.

The various magnetic states described in the previous section are possible equilibrium configurations of the magnetization forming in the FeGe films at different values of the external field and the thickness. It is important to note that these magnetic

structures are not uniquely determined by the film thickness and the field strength. Because of this, in order to avoid possible misunderstandings, we did not specify the values of the thickness and the field strength at which the states shown in Fig. 7.2 occur. In fact, several metastable states that can be significantly different from each other are often possible under identical conditions, depending only on the magnetic history of the sample or, in a numerical experiment, on the initial conditions of the simulation. While it is generally not possible to identify a unique magnetization state that develops in the thin-film element, micromagnetic simulations can be used to determine the type of magnetic structure that has the lowest energy. The results of these calculations are summarized in the phase diagram shown in Fig. 7.3(a). The intersections of the grid lines correspond to the simulation data points. We assume that the respective equilibrium magnetization state is stable in an area of $5 \text{ nm} \times 50 \text{ mT}$, on the phase diagram, with a data point at the center.

Although the magnetic structure at a specific thickness and field value is generally not unique, the phase diagram helps identifying the most preferable structure as far as the total energy is concerned. While at lower field values (below about 400 mT) the phase diagram is rather complex, evidencing a multitude of possible magnetic structures showing neither any clearly dominating state nor a significant thickness dependence, the situation becomes simpler at larger field strengths (above about 600 mT). Two main states emerge in these ranges of larger field values : the skyrmion configuration and the quasi-saturated states. Moreover, these states are separated by a clearly defined boundary in the phase diagram, showing a distinct impact of the film thickness. Specifically, if a field of 650 mT is applied, the formation of skyrmion structures will be energetically favorable if the film thickness is below 50 nm , while a quasi-saturated state will be the lowest-energy configuration at larger thickness values, as shown in Fig. 7.3(b). This observation represents the fundamental of the concept of geometrically constrained skyrmions that we present in this chapter. The idea is the following. If the film thickness is *locally* modulated within a region of the geometry such that, at a given field, the skyrmion structure is favorable in that thinner part while in the rest of the sample the thickness is large enough to favor a quasi-homogeneous state, these thickness modulations can be designed to constrain skyrmions. As we will show, this patterning makes it possible to generate preferential sites of skyrmion stability and, to some extent, achieve a geometric control of the skyrmion position within the geometry.

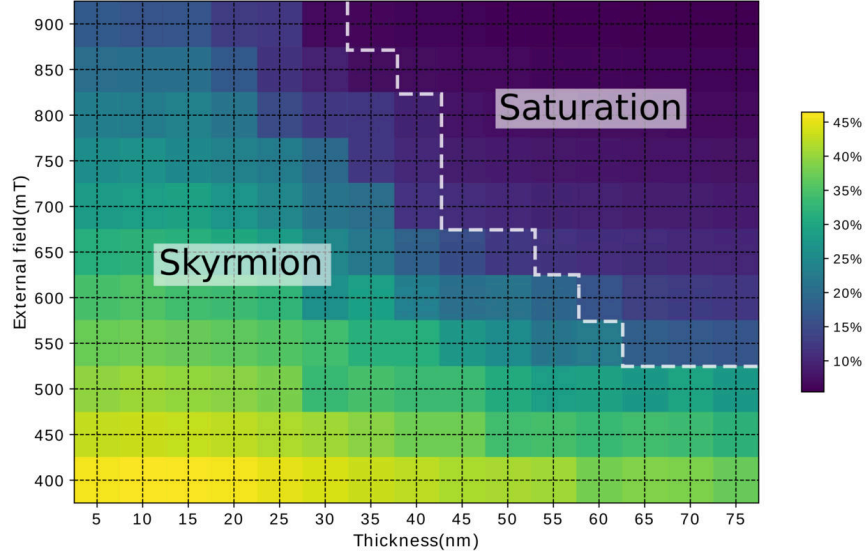


FIGURE 7.4 – Distribution of DMI as a percentage of total energy density, for the skyrmion and the saturation phase, obtained while plotting the phase diagram (Fig. 7.3). One can observe a decreasing percentage of DMI with increasing film thickness and external magnetic field as one transitions towards the saturation phase from the skyrmion phase. The percentage DMI plot also explains the dependence of skyrmion stability on the external magnetic field and thickness of the film.

7.1.3 Percentage energy contribution of DMI

Here, we plot the percentage energy contribution of the DMI to the total energy of the relaxed magnetization states of the skyrmion and the saturation phase (Fig. 7.4). The role of DMI in the stabilization of skyrmions in non-centrosymmetric ferromagnets has been recognized theoretically [19, 211], and experimentally [1]. With increasing external field, the saturation state becomes energetically more stable, compared to the skyrmion state, as the Zeeman energy dominates (discussed in section 5.1). Thus, the percentage DMI contribution to the total energy, as it competes with Zeeman energy, can indicate skyrmion stability with changing external field and film thickness. Even though it is possible to exactly calculate the energy barrier faced by an isolated skyrmion for a particular thickness modulation (as presented in section 7.3), the percentage DMI plot gives a rough idea of the same for a wide range of thickness and external magnetic field.

We find that DMI contributes more than 35% to the total energy at external magnetic fields lower than 550 mT for a film of thickness 40 nm. However, as the thickness is decreased to 10 nm, the DMI dominates till 700 mT. Similarly, if the thickness is increased to 70 nm, the DMI dominates only till 450 mT. Hence, with decreasing thickness and decreasing external magnetic field, the DMI contribution to the total energy increases, which includes the skyrmion phase. In contrast we find the saturation state where DMI no longer dominates the energy contribution and falls below 10% of the total energy. Even though not shown here, the percentage DMI contribution increases further for the bimeron and the helical state as compared to the skyrmion state.

7.1.4 Geometrically constrained skyrmions in circular pockets

We now consider magnetic structures forming in a FeGe platelet of 60 nm thickness containing dot-like cylindrical cavities within which the thickness is locally reduced to 30 nm. According to the phase diagram displayed in Fig. 7.3(a), at external field values of about 650 mT, the insertion of these cavities results in a geometry that generates specific regions where skyrmion structures are locally energetically favorable. This can lead to the formation, or the trapping, of skyrmions that are geometrically constrained to the regions in which the pockets have been introduced. Fig. 7.5 shows such a geometrically constrained skyrmion in a 60 nm thick platelet. The skyrmion remains confined to the small region in which the thickness is reduced by 50% through two cylindrical pockets with depth of 15 nm and radius of $r = 20$ nm, inserted symmetrically on both the top and the bottom surface of the film.

The geometrically constrained skyrmion, shown in Fig. 7.5, is stabilized by the geometry for two reasons. Firstly, as discussed before, in this field range the skyrmion state is generally favored because of the reduced film thickness. Secondly, the vortex-like magnetic configuration forming on the interior cylinder surfaces of the cavity helps pinning the position of the skyrmion to the center of the pocket. This cylindrical flux-closure structure thereby provides boundary conditions, albeit not in a mathematical sense, which constrain the skyrmion to this dot-like geometry. By forming such a cylindrical vortex structure, the magnetization finds a nearly optimal way to adapt to competing micromagnetic interactions. It thereby satisfies both the tendency of the DMI to introduce chiral, swirling patterns as well as the tendency imposed by the magnetostatic interaction to form flux-closure structures with the magnetization aligned along the

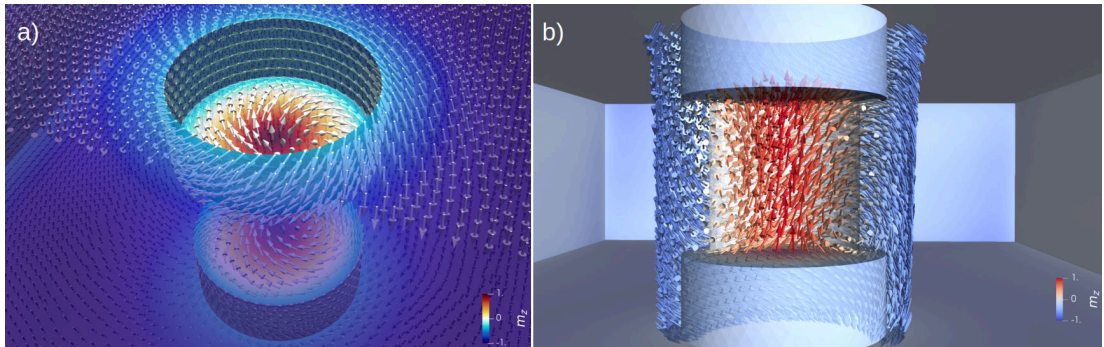


FIGURE 7.5 – (a) A skyrmion is formed at the base of the cylindrical pocket. At the inner cylinder surface of the cavities, the magnetization circulates on closed loops, thereby facilitating the formation of the skyrmion in the center. The semitransparent representation of the surfaces shows the formation of the skyrmion in both pockets, on the top and the bottom surface. The magnetic structure is displayed by arrows on the sample surfaces. Some of the arrows have been removed in order to improve the visibility of the structure. (b) View on the simulated skyrmion structure from inside the film. The skyrmion core connects the bases of the cylindrical pockets in the positive z direction, while the surrounding volume is magnetized in the negative z direction. The core of the skyrmion is delimited by a cylindrical isosurface $m_z = 0$, shown here as a weak, transparent contrast in order to preserve the view on the central magnetic structure. Only a small subset of the computed arrows of the magnetization direction calculated within the volume is displayed.

surfaces. Without the geometric modification in the form of pockets on the surface, the magnetic structure would be in a quasi-homogeneous state. The simulations show that a symmetric insertion of these pockets on both the top and the bottom surfaces is necessary to obtain the desired stability and localization of skyrmions. If the thickness variation is introduced only on one of the surfaces, the pinning of skyrmions appears to be much less effective.

If geometric modifications of the sample surface as described above can stabilize a skyrmion that would otherwise not form, the question arises whether this effect can be used to place skyrmions at specific positions where they might be generated or removed in a controlled way through external manipulation. This could be of interest, *e.g.*, for device concepts in which skyrmions are utilized as binary units of information, in a context similar to that of dot-patterned magnetic media for high-density data storage. In this case, the skyrmion pockets would take the role of the magnetic nanodots in bit-patterned media. While it is beyond the scope of this study to discuss the technical feasibility of such storage media or to explore the ability to write and delete individual skyrmion patterns into the pockets, we can show that, indeed, it is possible to stabilize skyrmions in various geometrically predefined locations that could be addressed individually. Fig. 7.6(a)-(e) shows several examples of simulations in which the position of skyrmions in a thin-film element can be predetermined by introducing several pockets of the type discussed before. As shown in Fig. 7.6(e), our simulations predict the possibility to stabilize six skyrmions at well-defined positions, placed on a regular grid, in our sub-micron FeGe platelet. Although the results shown in Fig. 7.6 may suggest a nearly optimal geometric control of the skyrmion positions, it is important to note that the pockets discussed here merely provide *preferential sites* for skyrmions. The latter may or may not form or remain pinned at those sites. In particular, it is not sufficient to thin-out a part of the sample in a sample to ensure the appearance of geometrically constrained skyrmions. The purpose of such pockets could rather be to capture existing skyrmions and to fix their positions at well-defined positions, similar to the domain-wall pinning role that is played by notches in conventional racetrack-memory devices. It should also be noted that the geometric trapping of skyrmions with such pockets does not always work, in particular when the pockets are too closely packed due to skyrmion-skyrmion repulsion [48, 212]. We also found that skyrmions cannot be stabilized at positions too close to the lateral sample boundaries due to repulsion

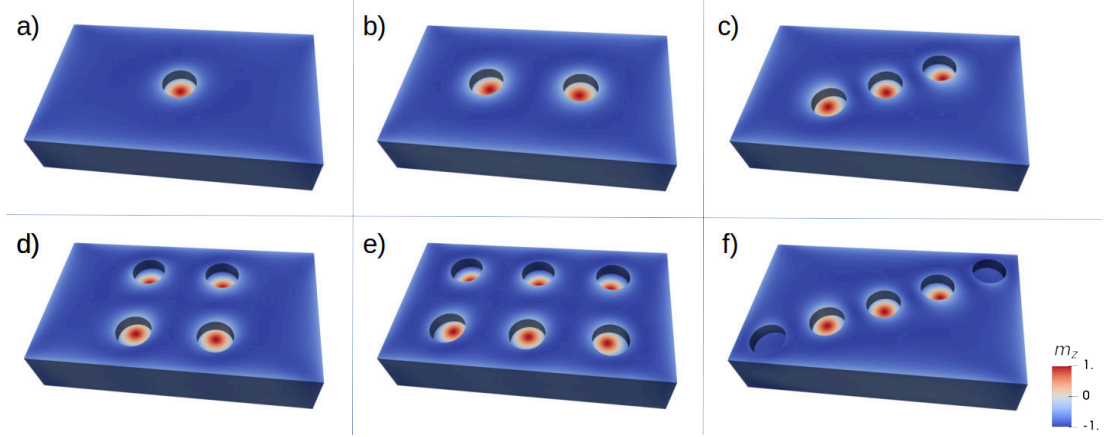


FIGURE 7.6 – Geometrically constrained skyrmions in FeGe platelets. By introducing circular pockets at specific positions, skyrmions can be artificially stabilized at positions that they would otherwise not attain. The geometric control, however, is not unlimited. Attempts to pack skyrmions too closely or to place them too close to the sample boundary can fail. This is shown in panel f), where skyrmions are stabilized only in the three central pockets, while the two outermost pockets remain empty.

[48, 213]. An example of such a failed attempt is shown in Fig. 7.6(f). In spite of these limitations, the ability to geometrically constrain skyrmions provides an attractive way to obtain control over the skyrmion position in thin-film elements, which could have important technological implications.

7.1.5 Geometrically constrained skyrmions on thin paths

With the help of the results obtained in section 7.1.2 and section 7.1.3, we choose the values of film thicknesses of the path and the rest of the film for the example geometries (geometry and dimensions of the curved path as shown in Fig. 7.1), which show static skyrmion confinement at a fixed external field. The thickness of the thin paths in the geometries is 30 nm, while the rest of the film's thickness is 60 nm. The desired regions of skyrmion confinement are the thin paths. By initiating the simulations from random magnetization configurations, The magnetization states obtained in the example geometries, at a uniform external magnetic field of strength 650 mT, are shown in Fig. 7.7(a), 7.7(b), 7.7(c). According to the phase diagram, at 650 mT, the skyrmion state is energetically favorable for the film thickness of 30 nm, and the

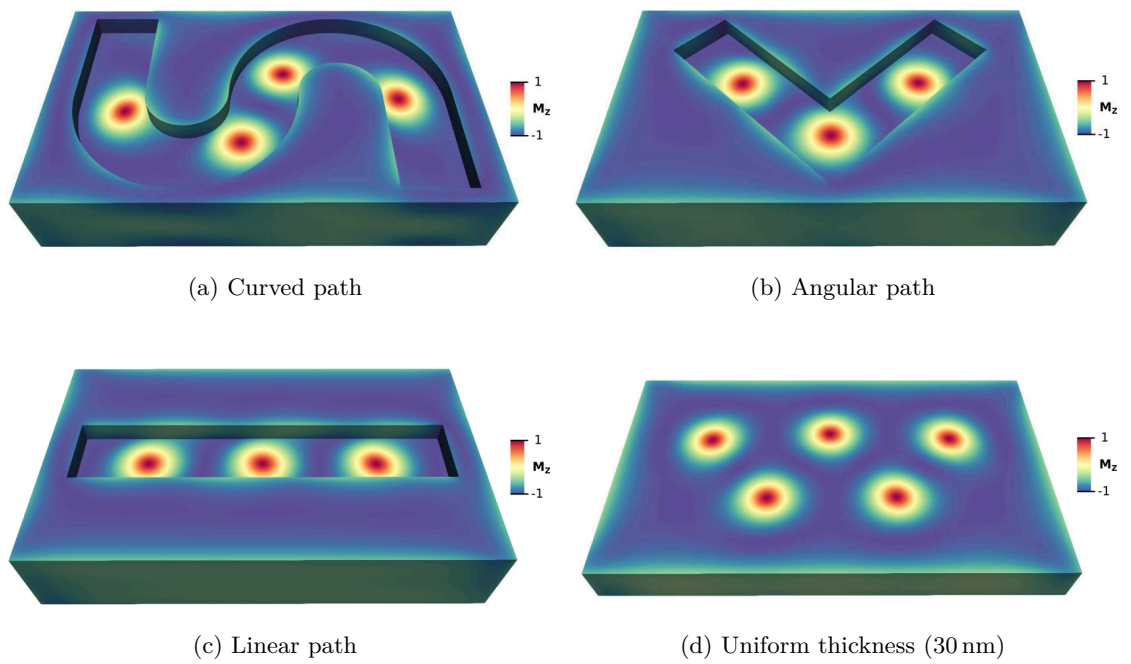


FIGURE 7.7 – (a)-(c) shows the magnetization states stabilized in the example geometries with thin paths at a constant external magnetic field of strength 650 mT in $-z$ direction. One can see how skyrmions stay confined to the desired region of the geometry. For comparison (d) shows hexagonal skyrmion lattice stabilized in the skyrmion phase of a film of uniform thickness 30 nm, at 650 mT in $-z$ direction.

7.2 Modeling skyrmion magnetization configuration

saturation state is energetically favorable for the film thickness of 60 nm. Here, we see that the skyrmions stay confined to the thinner paths even though they form complex shapes compared to the natural triangular/hexagonal lattice arrangement. For comparison, Fig. 7.7(d) shows a triangular/hexagonal skyrmion lattice arrangement stabilized in the film of uniform thickness 30 nm obtained in the skyrmion phase at 650 mT. As mentioned earlier, it is crucial to emphasize that the skyrmion state favors a triangular/hexagonal skyrmions lattice arrangement and not the meta-stable isolated skyrmion configuration. Hence, the skyrmions in the complicated example geometries, confined to the thin paths, are moved from their equilibrium positions compared to a triangular/hexagonal lattice arrangement. To get an idea of this balance of forces, one needs to understand the energy barrier posed by the thickness modulation. Thus, in the next step, we mathematically model the magnetization structure of an isolated skyrmion. Then, we utilize this modeled magnetization configuration to calculate the total energy barrier faced by an isolated skyrmion as it moves across the thickness barrier in the linear path geometry. The modeled isolated skyrmion configuration serves as an initial magnetization configuration, whose core will be pinned at a definite position and the rest of the magnetization relaxed through simulation. We obtain the total energies of thus relaxed magnetization configurations to plot the energy barrier.

In conclusion, we have shown that skyrmions can be confined statically in the desired region of material geometry through film thickness modulation, forming complex shapes. The ability to manipulate the skyrmion position could be quite valuable for skyrmion-based device applications, referred to as skyrmionics [124]. In the following sections, we show that this strategy can be employed to counter the problem of the lateral drift motion due to skyrmion Hall effect in the skyrmion racetrack devices and fine-tune the frequency of isolated skyrmion magnetization modes in nanodot geometries. Further, as discussed in section 7.1.4, such thickness variations can also be employed to create complex skyrmion arrangements in extended thin films compared to the naturally observed triangular/hexagonal lattice arrangement. These new arrangements might show unique dynamic properties such as magnon scattering [145].

7.2 Modeling skyrmion magnetization configuration

To model the magnetization configuration of an isolated skyrmion, we choose the skyrmion state stabilized in a linear path geometry as an example. Later, we will use

7.2 Modeling skyrmion magnetization configuration

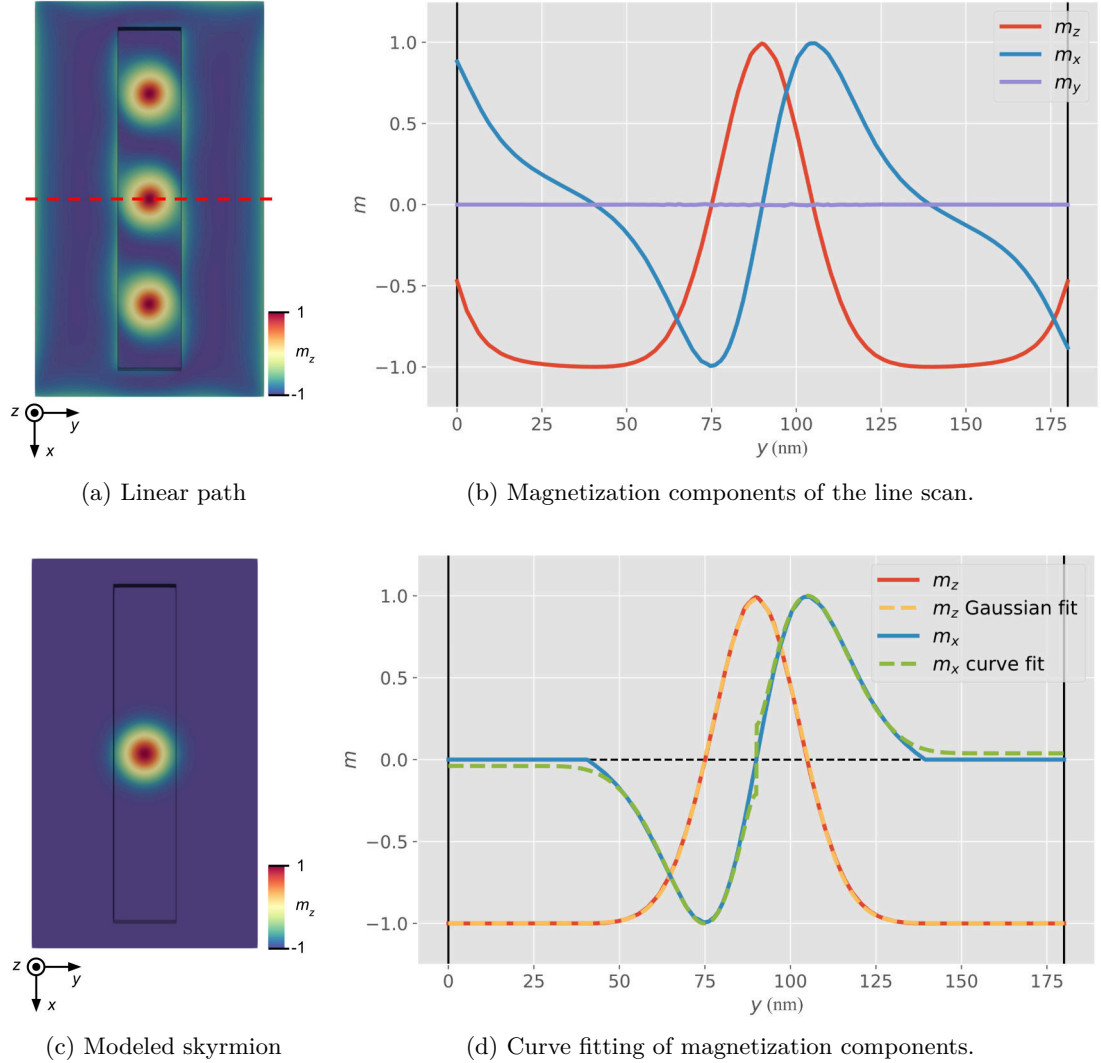


FIGURE 7.8 – The figure describes the steps in modeling the magnetization configuration of a skyrmion. (a)-(b) The red dashed line shows the line used to sample the three magnetization components of a confined skyrmion in the linear path geometry, which is along the y -axis. The graph showing the magnetization components of the line scan is to the right. We note that m_y is virtually zero and m_z resembles a Gaussian. Moreover, m_x and m_z show a deviation from the bulk, near the edges of the geometry, due to the boundary conditions imposed by DMI and magnetostatic interactions. (c)-(d) The graph shows the Gaussian fit to m_z and corresponding $m_x = \sqrt{1 - m_z^2}$, considering m_y to be zero. The magnetization configuration of thus modeled skyrmion is shown to the left.

7.2 Modeling skyrmion magnetization configuration

the same example geometry to calculate the energy barrier faced by the isolated skyrmion as it moves across the thickness barriers. First, we extract the three magnetization components along a line across the skyrmion state, as shown in Fig. 7.8a. The line is parallel to the y-axis of the material geometry. We plot thus obtained magnetization components in Fig. 7.8b. Interestingly, the magnetization component along the line m_y is virtually zero, in the skyrmion state, as the magnetization rotates perpendicular to the radial direction. Secondly, we notice the bend in the remaining two magnetization components (m_x and m_z) as we approach the boundary of the geometry. One can attribute this bending to the boundary conditions imposed by the DMI [171] and the magnetostatic interaction in the material geometries with finite dimensions. It is not unique to the magnetization configuration of a skyrmion. To model the isolated skyrmion, we ignore these boundary conditions and assume that the magnetization of the skyrmion uniformly decays into a fully saturated magnetization state. With this assumption, the values of m_z can be represented as a Gaussian and m_x as $\sqrt{1 - m_z^2}$, since m_y is virtually zero, as shown in Fig. 7.8d. The value of m_z varies from +1 to -1 from the skyrmion center to the uniformly saturated state, respectively. Considering a pure Gaussian, m_z will attain the value -1 at an infinite distance from the center of the skyrmion. Hence, we assume it to be a Gaussian from its values +1 up till -0.999, and the distance between these values will be considered the radius of the skyrmion. To find a curve that fits the data points for m_z obtained through the line scan, we employ a non-linear least squares method. The test function for the fit is as follows.

$$m_z = a \cdot \exp\left(-\frac{(y - b)^2}{c}\right) + d \quad (7.1)$$

The test function represents m_z as a function of y-coordinate (along the line scan shown in Fig. 7.8a), where a, b, c, and d are the constants that we evaluate. Through the non-linear fit for the magnetization configuration of a skyrmion in linear path geometry, we obtain the values of the constants to be 2, 90, 330.74, and -1 respectively. The values of a and d keeps the range of m_z between +1 and -1. The value of b represents the y-coordinate of the center of the skyrmion in the material geometry reference frame and the constant c is a function of the radius of the skyrmion. As mentioned above, if we assume that the Gaussian representation of m_z is valid from +1 up till -0.999, and this range represents the radius of the skyrmion, then we can write

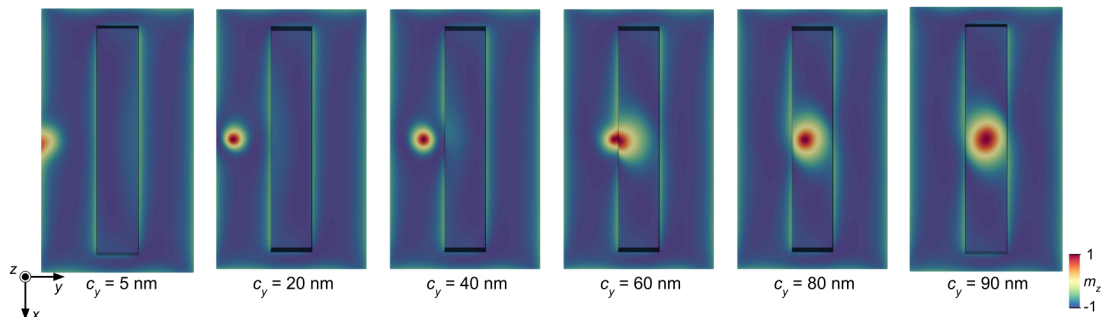


FIGURE 7.9 – Here we show the snapshots of isolated skyrmion with pinned center, in the linear path geometry (Fig. 7.7c), as it moves across the thickness barriers along y -axis (c_y represents the y co-ordinate of the skyrmion center). We calculate the total energy of the system for each of the configuration snapshot and plot it as a function of c_y (Fig. 7.10) to calculate the energy barrier faced by the skyrmion to move from thin path to the thickness barriers. Even though the center of the skyrmion is pinned to the position, the rest of the magnetization distorts to minimize total energy.

$c = r_{sky}^2 / \ln(2000)$. To model the magnetization configuration of the isolated skyrmion in a three-dimensional geometry, we assume it to be circularly symmetric around the direction of the external magnetic field, which is along the z -axis in our case. For the plane perpendicular to the direction of the external field (xy -plane), the orientation of in-plane magnetization moments resemble a magnetic vortex and the magnitude will be $\sqrt{1 - m_z^2}$. Further, the vorticity of the magnetization moments depends on the sign of the DMI constant. Thus, we obtain an artificially created magnetization configuration of an isolated skyrmion shown in Fig. 7.8c.

7.3 Skyrmion potential well

Here, we calculate the energy barrier faced by the skyrmion confined to the thin path of linear path geometry (Fig. 7.7c). To calculate the energy barrier, we need the values of the total energy of individual magnetization configurations, in which an isolated skyrmion moves across the thickness barriers (Fig. 7.9). It requires us to stabilize the skyrmion in regions of the geometry where otherwise it is unstable, such as the thickness barrier. One way to calculate the barrier is to make use of the modeled isolated skyrmion (discussed in Section 7.2) by artificially placing it at a definite length

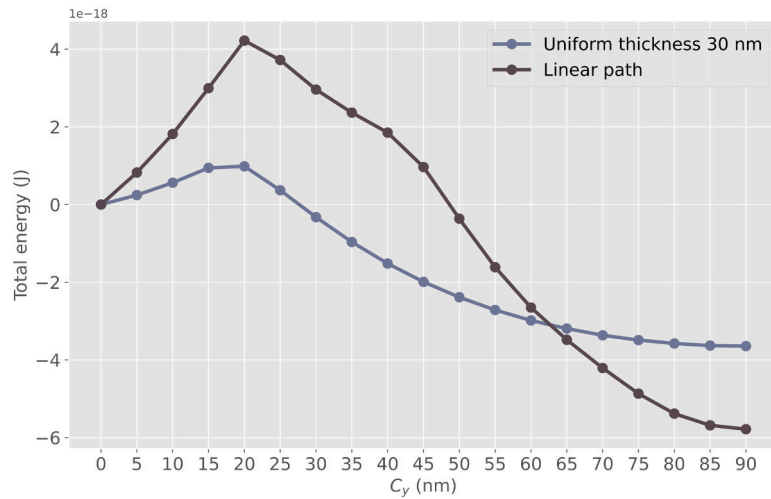


FIGURE 7.10 – Total energy vs. the isolated skyrmion center, in the linear path geometry (Fig. 7.7c) and a uniform film of thickness 30 nm. We consider the total energy of a quasi-saturation state, for both the geometries, as a reference and set its value to zero. We find that the energy barrier posed by the thickness barrier is almost twice compared to the uniform thickness, which explains the skyrmion confinement. The calculation of the energy barriers is performed at a constant external field of strength 650 mT.

intervals across the thickness barrier and calculating the total energy at each position. However, the magnetization configuration of the skyrmion that we obtain from the model (Section 7.2) is relatively rigid. Typically, the magnetization configuration of a three-dimensional skyrmion can distort to minimize energy [46, 214]. Moreover, we had assumed while modeling the isolated skyrmion that the rest of the material, except the skyrmion, is in a fully saturated magnetization state along the direction of the external field. The assumption is not correct for the boundaries of the material due to boundary conditions imposed by the DMI and the demagnetization field.

We take another approach to calculate the energy barrier. To stabilize the isolated skyrmion in a region of the geometry where it is otherwise unstable (e.g., the thickness barriers), we begin the simulation with the magnetization configuration of the modeled isolated skyrmion; however, the magnetization of a small central region of the skyrmion core (radius of 10 nm) is rigidly fixed in the opposite direction of the external field, to pin the skyrmion at the position. Then, we let the magnetization relax to minimize the total energy of the system. In this way, the magnetization of the material has the flexibility to attain a realistic configuration while keeping the skyrmion pinned at the desired region of the geometry. We choose positions to pin the skyrmion center at an interval of 5 nm, in a way as mentioned above, across the thickness barrier of the linear path geometry to calculate the energy barrier profile, as shown in Fig. 7.10. The resulting magnetization configurations are presented in Fig. 7.9.

It is interesting to note that even though we had pinned the centers of the skyrmions to the definite regions of the geometry to calculate the energy barrier, the magnetization configurations of the skyrmions does distort in almost every case to minimize the total energy at the respective positions (Fig. 7.9). This validates our assumption that using the rigid magnetization configuration of the modeled isolated skyrmion, alone, to calculate the skyrmion energy barrier is unrealistic. Further, letting the rest of the geometry's magnetization configuration relax gives the twist at the material boundaries, an effect of the boundary conditions imposed by DMI [171].

The quasi-saturation or quasi-ferromagnetic state represents the magnetization configuration in the absence of an isolated skyrmion. Hence, in calculating the energy barrier posed by the thickness modulation, we take it as a reference and assume it has zero energy. We show the total energy plot as a function of a co-ordinate of the skyrmion center in Fig. 7.10. For comparison, we also show the total energy plot of a uniformly

thick (30 nm) film, of the same lateral dimensions as the linear path geometry. It is clear from the plot that the thickness modulation creates a *potential well* for the isolated skyrmion, which leads to its confinement. The small energy barrier that exists for the skyrmion in the geometry without a thickness modulation can be attributed to the repulsion that an isolated skyrmion experiences from the boundaries [48, 130, 212, 213]. It is important to note that since the stability of the skyrmion state depends on the external field, in addition to the film thickness, the energy barrier profile discussed here will also depend on the same. The external field is kept constant at 650 mT for the calculations presented here.

7.4 Dynamic skyrmion confinement

In this section, we study the confined dynamics of three-dimensional skyrmions due to thickness modulation. We subdivide the study into primarily two parts. Firstly, we study the possibility to counter unwanted skyrmion Hall effect, with thickness barriers, in an *H-shaped* racetrack geometry. The isolated skyrmion is displaced with the help of a spin-polarized current. Secondly, we investigate the impact of skyrmion confinement on the frequency of magnetization modes in a disc geometry with a thickness barrier at the edge.

7.4.1 Dynamic skyrmion confinement in H-track geometry

In recent years, magnetic skyrmions have received considerable attention from the magnetism community due to their topological stability and particle-like nature. This unique property makes them a promising candidate for nanotechnology applications, such as nonvolatile memory devices [7]. Moreover, it is possible to displace skyrmions with very low current densities (of the order of $1 \times 10^6 \text{ A m}^{-2}$) compared to domain walls in confined geometries [2]. The skyrmion Hall effect (SkHE), where a skyrmion drifts perpendicular to the direction of the applied spin-polarized current, is one phenomenon that substantially impedes such progress [215]. On a modified racetrack geometry of material FeGe, our calculations show that it is possible to counter SkHE by adding a thickness barrier on the track edges and, thus, confine the skyrmions. Inspired by the linear path geometry studied in static confinement (Fig. 7.7c), we propose a racetrack geometry with thickness barriers at the lateral edges, as shown in Fig. 7.11.

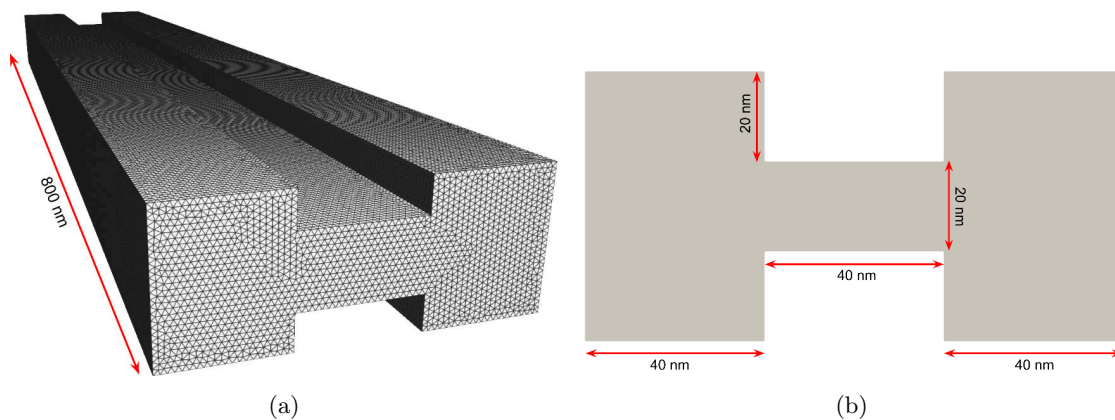


FIGURE 7.11 – The figure shows the dimensions of the proposed H-track geometry. (a) shows the length of the skyrmion which is 800 nm. (b) shows the cross-section of the H-track geometry. The thin central path, where we confine the isolated skyrmion, is of thickness 20 nm. The barrier at the edges have a thickness 60 nm. The width of the thin central path and the barriers is 40 nm.

Henceforth, we will refer to the geometry as an H-track geometry. The goal is to study the motion of an isolated skyrmion in the thin central path. For the study, we consider an H-track of length 800 nm (Fig. 7.11a). We show the cross-section in Fig. 7.11b. The width of the thin path and both the thickness barriers is 40 nm. The thickness of the thin path is 20 nm, while the thickness of the barriers is 60 nm.

First, we stabilize an isolated skyrmion at one of the thin central path's ends at an external field of 700 mT, starting from the modeled isolated skyrmion configuration (Section 7.2) of diameter 40 nm. We chose a high value of the external magnetic field to stabilize an isolated skyrmion, which is meta-stable in the given conditions. To study the dynamics, we apply a current along the direction of the H-track geometry length. We find that, on applying a current density, the isolated skyrmion indeed stays confined to the thin central path (Fig. 7.12). The thickness barriers counter the unwanted SkHE and keeps the isolated skyrmion confined, similar to the static case (section 7.1). Starting from a minimal current density of the order $1 \times 10^6 \text{ A m}^{-2}$, the isolated skyrmion stays confined until an unrealistic high current density of $8 \times 10^{12} \text{ A m}^{-2}$. In a uniformly thick racetrack geometry of the same lateral dimensions as the H-track and a thickness of 20 nm (same as the thin central path), the isolated skyrmion gets expelled by the SkHE at a current density of $2 \times 10^{12} \text{ A m}^{-2}$. The addition of thickness barriers increased the

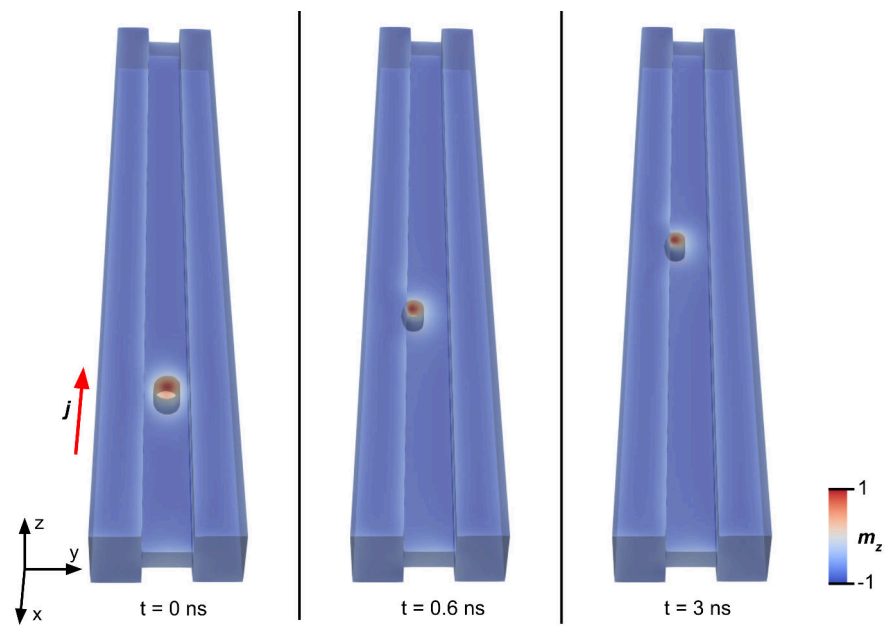


FIGURE 7.12 – The image shows time snapshots of isolated skyrmion motion in H-track geometry. The applied current density is $4 \times 10^{12} \text{ A m}^{-2}$. One can see that even at high current densities, the skyrmion stays confined to the thin central path.

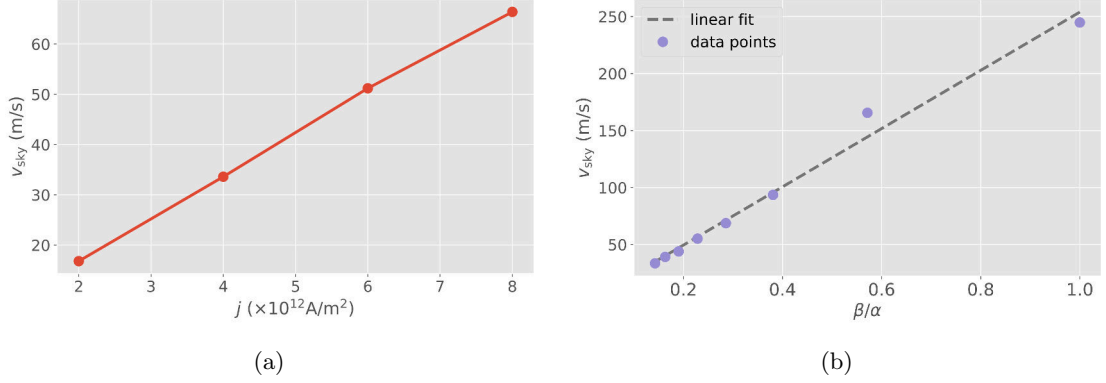


FIGURE 7.13 – Dependence of skyrmion velocity on current density (j) and α/β ratio in the H-track geometry. (a) For the plot between skyrmion velocity and current density, we fix the values of $\alpha = 0.28$ and $\beta = 0.04$. Similarly, (b) for the dependence of the same on β/α , we fix the value of current density at $4 \times 10^{12} \text{A m}^{-2}$. In both the cases, we find linear dependence of skyrmion velocity. One can explain this analytically with the help of Thiele equation.

maximum current density tolerance by a factor of four. We also study the current-velocity relationship of the isolated skyrmion in the geometry. Fig. 7.13a shows the skyrmion velocity plot with increasing current density. It reveals a linear relationship of the skyrmion velocity with the current density. To investigate how the skyrmion velocity depends on the current density, we kept the the value of Gilbert damping (α) = 0.28 and coefficient of non-adiabaticity (β) = 0.04. Further, we study the dependence of skyrmion velocity on the ratio β/α by keeping the current density constant at $4 \times 10^{12} \text{A m}^{-2}$. We keep the value of the β constant at 0.04 while changing the α value from 0.04 to 0.28. In Fig. 7.13b, we plot the data points of skyrmion velocity corresponding to the β/α values. Similar to the current-velocity plot, the plot shows a linear relationship. We study two more H-track geometry with a barrier thickness of 100 nm and 130 nm, keeping the thin central path's thickness the same (20 nm). However, the previously discussed results of the skyrmion velocity dependence on current density and β/α ratio remain unchanged.

It is possible to analytically obtain an expression for the isolated skyrmion velocity, in a confining potential, based on the approach pioneered by A. Thiele [26]. Even though the confining potential of thickness barriers distorts the skyrmion's shape, the

overall motion can be considered a steady-state motion. Hence, the following equation of motion for the skyrmion is obtained, based on equation 2.30 [130, 216] :

$$\mathbf{G} \times (\mathbf{v}^e - \mathbf{v}^{\text{sky}}) + \mathcal{D}(\beta\mathbf{v}^e - \alpha\mathbf{v}^{\text{sky}}) + \mathbf{F} = 0 \quad (7.2)$$

Here \mathbf{v}^e is the velocity of the electron (in the opposite direction and directly proportional to the current density), and \mathbf{v}^{sky} typically represents the velocity of magnetization configuration ; however, as we study an isolated skyrmion, we assign it to the skyrmion velocity. \mathbf{G} is the gyromagnetic coupling vector, which represents the Magnus force (SkHE). For the magnetization configuration of a skyrmion, which is in the $x - y$ plane in our case, $\mathbf{G} = 4\pi Q\mathbf{e}_z$, where $Q = -1$ (skyrmion number) and \mathbf{e}_z is a unit vector in the z -direction. \mathcal{D} is the dissipative force tensor. The components of the tensor are $\mathcal{D}_{xx} = \mathcal{D}_{yy} = \mathcal{D}$ and otherwise zero. The final term \mathbf{F} represents a force on the magnetization configuration from the surroundings, excluding the spin-polarized current. One may simplify equation 7.2 by assuming no force along the H-track (x -axis), which is also the current direction, as there is no thickness barrier. Further, one may assume that the skyrmion velocity across the thickness barrier (y -axis) is zero due to the confining potential. Hence, we obtain the following expression for the skyrmion velocity in x -direction :

$$\mathbf{v}_x^{\text{sky}} = \frac{\beta}{\alpha}\mathbf{v}_x^e \quad (7.3)$$

Where the velocity of electrons is proportional and opposite to the direction of current density. Hence, we obtain a linear relationship of skyrmion velocity with both current density and β/α , which is in agreement with the simulation data.

7.4.2 Magnetization modes of confined skyrmion

The study of dynamical modes of a magnetization configuration has been of great interest from both fundamental physics and application point of view. Not only does it reveal the magnetic properties of the material, but also the interaction of the magnetization configuration with electromagnetic waves (EMW), its stability, and possible phase transitions.

The interaction of an incident EMW with the magnetization configuration occurs through its oscillating magnetic field, which exerts a periodic torque on the components

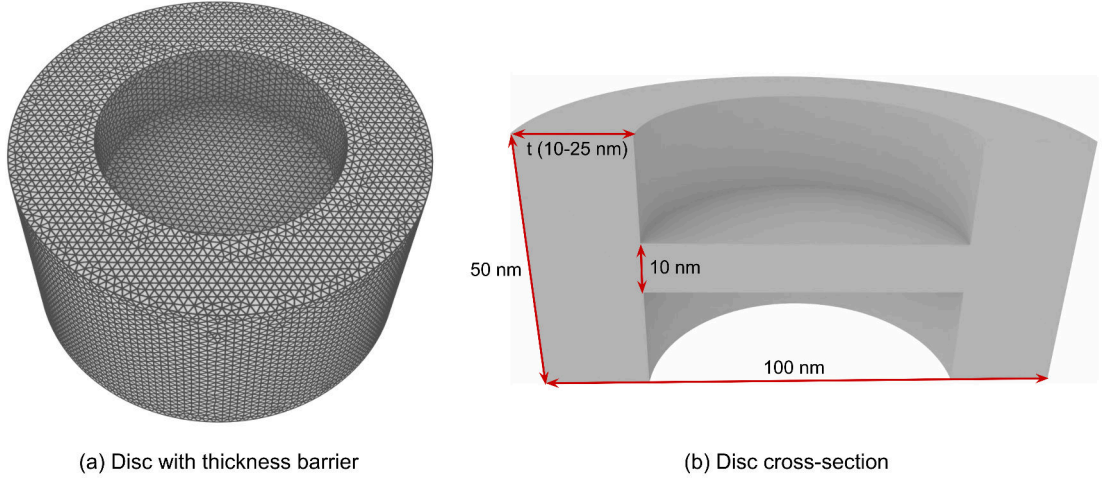


FIGURE 7.14 – The geometry of the disc with thickness barrier at the edge. (a) The FEM mesh used to properly model the curvatures in the barrier disc geometry. (b) The cross-section of the barrier disc geometry showing the central thin disc part with thickness 10 nm and thickness barrier with thickness 50 nm. The width of the thickness barrier is varied from 10 nm to 25 nm keeping the total diameter of the geometry constant at 100 nm.

of the magnetization that are perpendicular to the field. Hence, the magnetization configuration's dynamical modes can affect the reflection and absorption of EMW. It is possible to tune these properties by changing the material parameters such as the magnetic anisotropy or the constant external magnetic field or the material geometry (like the study presented here).

As mentioned above, the study of dynamical modes is also essential for detecting magnetization phase transitions. In particular, the low-frequency dynamical modes can be used as an indicator of the onset of a phase transition, where the frequency is driven to zero as a function of applied field or other parameters.

Here, our aim is to study the impact of geometric confinement on the magnetization modes of a confined isolated skyrmion. The skyrmion is stabilized in an FeGe disc geometry with a thickness barrier of variable widths, at the edge (geometry is shown in Fig. 7.14). To understand the impact of confinement the study is divided as :

1. We identify the different dynamical modes of confined skyrmion present in disc geometry with thickness barrier at the edge.

2. We analyze how the skyrmion confinement affects the frequencies and power of the dynamical modes.
3. We compare the obtained modes of the confined skyrmion with an isolated skyrmion in a disc of uniform thickness, i.e., without a thickness barrier.

In the disc geometry, the barrier's thickness is 50 nm, while the thin central region's thickness is 10 nm. The equilibrium position of the skyrmion is at the center of the disc. The total width of the disc, i.e., the diameter, remains constant at 100 nm. However, to understand the barrier's impact on the dynamical modes of the confined skyrmion, we vary its width from 10 nm to 25 nm in an increment of 5 nm. To stabilize the equilibrium skyrmion states, we start the simulations from the modeled isolated skyrmion configuration (Section 7.2) at the center of the discs and relax it in an external magnetic field of 400 mT in the negative z -direction. We observe that the barrier's width affects the skyrmion core radius, where the skyrmion core shrinks with the increasing barrier width. Thus, the changing magnetization configuration of the isolated skyrmion due to geometrical confinement affects the modes' frequency and power.

To obtain the magnetization modes, we first perturb the stabilized isolated skyrmion configuration by a small external field. Once the skyrmion has achieved a new equilibrium in the presence of the perturbation, we remove it and let the skyrmion relax to the original equilibrium position. This process of perturbing the skyrmion from its equilibrium position and letting it relax back to the original equilibrium leads to a magnetization configuration excitation, a superposition of the magnetization modes. To obtain individual magnetization modes, we perform spatially resolved Fourier analysis. The magnetization dynamics of the isolated skyrmion due to the external field perturbation is captured for 12 000 ps, at fixed intervals of 10 ps, at individual spatial discretization points. Further, we subtract the original skyrmion equilibrium state's magnetization, which essentially acts as a static background, from the dynamic calculations to refine the magnetization excitation. The Fourier transform of the excitation yields peaks in the power spectrum plot corresponding to different magnetization modes. We perform a windowed Fourier back-transform for the modes' frequency window to obtain the individual modes' time-domain dynamics. For the Fourier analysis presented in this study, a python code developed by our group member Rajgowrav Cheenikundil has been used.

The lateral modes are obtained by applying the small field in the x -direction, per-

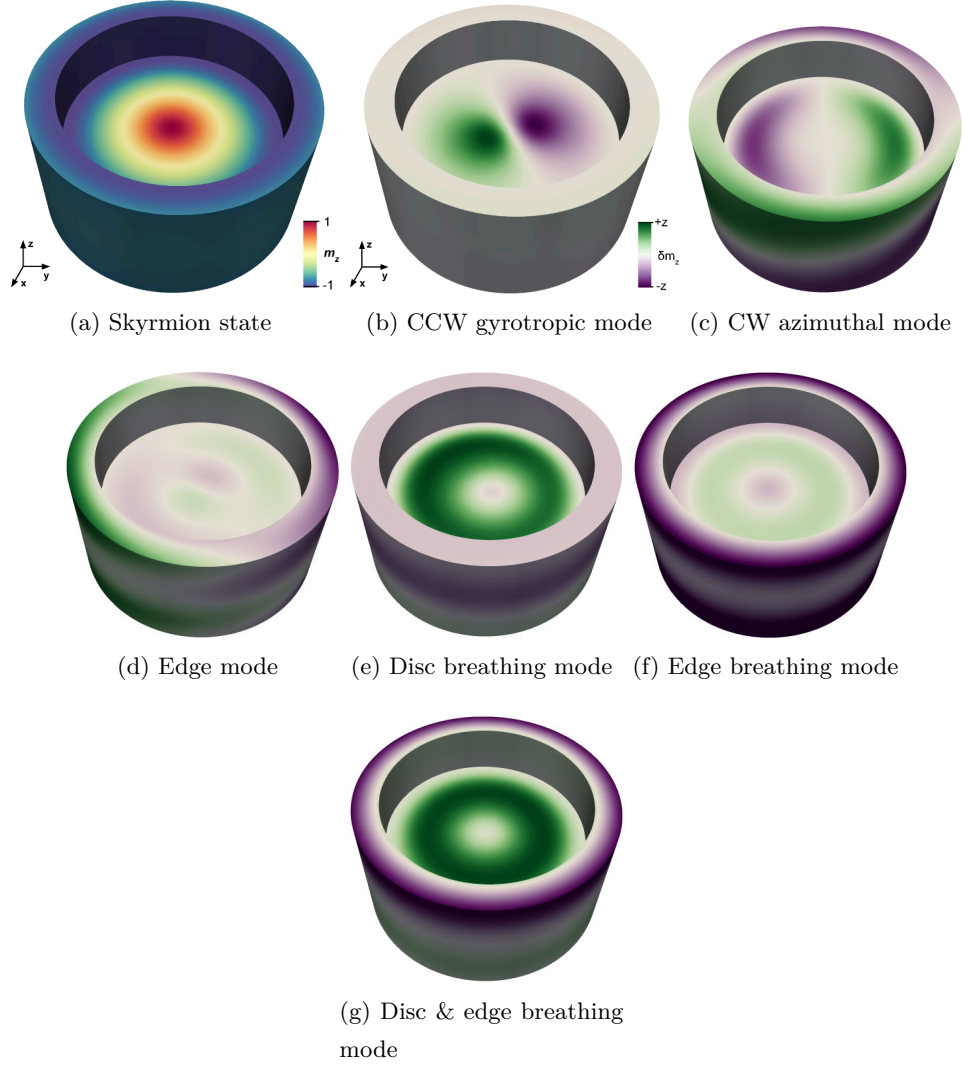


FIGURE 7.15 – Fourier amplitude in the form of δm_z for all the dynamical magnetization modes obtained in the barrier disc geometry. For coherence, the width of the thickness barrier is chosen to be 10 nm for the representation of the modes. (a) Isolated skyrmion state stabilized in the geometry at 400 mT in negative z -direction. The color-map represents the magnetization in z -direction for the skyrmion state. The image serves as a reference for the amplitude of the magnetization modes shown in the following images. (b)-(g) The Fourier amplitude of the six principal magnetization modes shown with the help of δm_z .

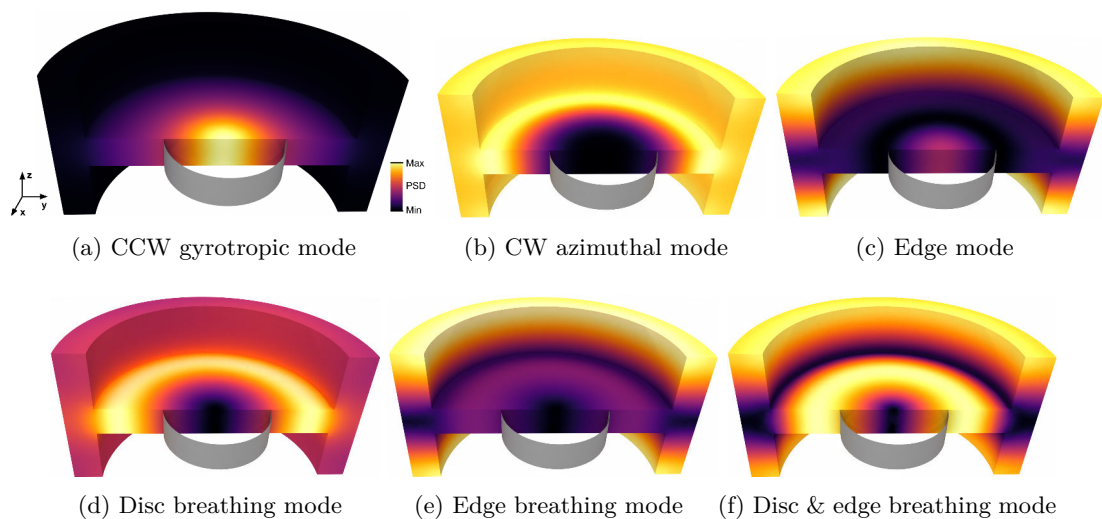


FIGURE 7.16 – Distribution of power in the geometry for the six magnetization modes of the barrier disc with the help of PSD. The gray iso-surface (corresponding to $m_z = 0$) represents the core of the skyrmion state stabilized in the geometry; shown in order to identify the regions of activity with respect to the skyrmion core.

pendicular to the constant external field in the negative z -direction. Similarly, the breathing modes are obtained by applying the small field in the negative z -direction, parallel to the constant external field. We choose the value of perturbation small enough (50 mT compared to the constant external field 400 mT) so that the magnetization excitation of the skyrmion stays in the linear regime. We also apply small field pulses of a Gaussian profile in x and z -direction to study the possibility to excite the respective modes with a field pulse.

We obtain six (three lateral and three breathing) principal dynamical modes of the confined skyrmion : gyrotropic, asymmetric azimuthal, edge, breathing disc, breathing edge, and breathing disc & edge modes. Note that in the following description of the dynamical modes, we consider the magnetization dynamics with respect to the skyrmion core polarity. As previously mentioned, the external magnetic field points in the negative z -direction. Thus, the stabilized skyrmion core points in the positive z -direction, and we evaluate the dynamics of the skyrmion from the bottom view.

The gyrotropic mode (Fig. 7.15(b)) represents the skyrmion center’s counter-clockwise rotation. The Fourier amplitude of the corresponding magnetization dynamics is presented in Fig. 7.16(a), from which one may argue that the magnetization dynamics is li-

mited to the skyrmion core, i.e., $m_z > 0$. The asymmetric azimuthal mode (Fig. 7.15(c)) corresponds to a clockwise magnetization rotation, excluding the skyrmion core, i.e., $m_z < 0$. The Fourier amplitude of the dynamics (Fig. 7.16(b)) shows that the skyrmion core remains inactive. The mode is referred to as asymmetric as it breaks the axial symmetry along the z -axis. We find that the mode can not be excited with a field pulse perpendicular to the skyrmion plane for a spatially uniform profile. Hence, a spatially asymmetric pulse is required in order to excite the mode in such a case. Such modes have been well studied in magnetic vortices, where the magnetization's temporal evolution was resolved experimentally [217]. The lateral edge mode (Fig. 7.15(d)) resembles the asymmetric azimuthal mode at a higher frequency with little skyrmion core activity. From the Fourier amplitude of the mode (Fig. 7.16(c)), one can see that the mode is confined to the protruding thickness barrier edges and has a spatial node at the center along the width. It is interesting to note that, with increasing barrier width, the activity at the skyrmion core further diminishes, however, the total Fourier amplitude increases. The breathing disc mode (Fig. 7.15(e)) represents the compression and expansion of magnetization configuration of the inner thin disc represented by axially symmetric oscillation of change in m_z , i.e., δm_z . The magnetization dynamic is primarily spread around $m_z < 0$, as shown in Fig. 7.16(d) Fourier amplitude. Typically, one may excite the breathing modes with an out of plane field pulse, which is valid for all the geometries and all the breathing modes in our case. The edge breathing mode, similar to the edge mode, shows a predominant activity in the thickness barrier edges (Fig. 7.16(e)), with a node at the center. The value of δm_z oscillates coherently at both the edges and it is out of phase by π with the small oscillation at the thinner disc (Fig. 7.15(f)). Finally, the edge & disc breathing mode shows activity at both the central thin disc and barrier edges (Fig. 7.16(f)). It is interesting to note that, at the edges, the δm_z oscillations are out of phase by π and, in turn, both the edges are out of phase by $\frac{\pi}{2}$ with the thinner disc (Fig. 7.15(g)).

To understand the impact of skyrmion confinement on dynamical modes, we plot their frequencies and Fourier amplitude with changing thickness barrier width (Fig. 7.19). Also, we compare the corresponding modes with the ones obtained in a disc with the same lateral dimensions as the barrier disc, but with uniform thickness 10 nm (Fig. 7.17 and Fig. 7.18), where the thickness is related to the thinner disc part of the barrier disc geometry (Fig. 7.14(b)). The external magnetic field remains constant at 400 mT for

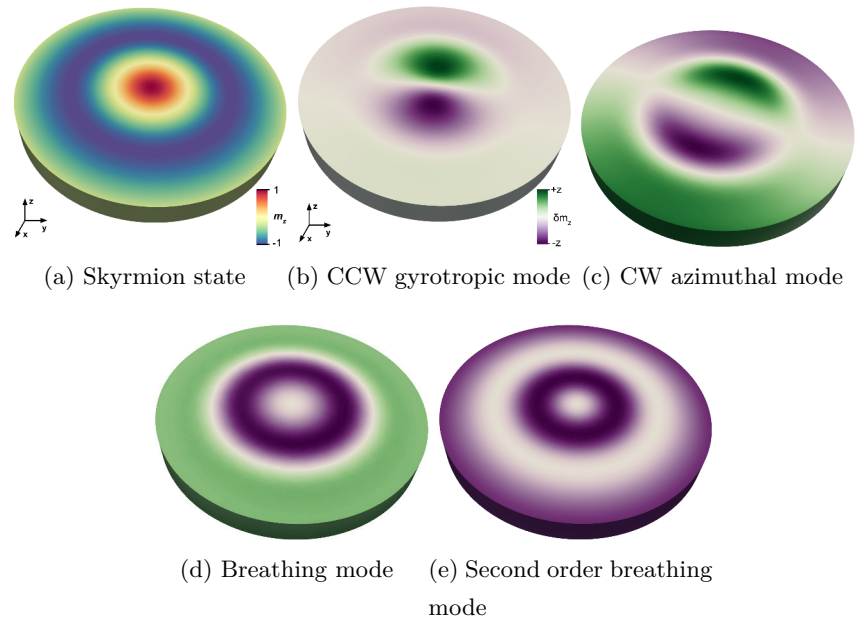


FIGURE 7.17 – Fourier amplitude of four magnetization modes obtained in a disc geometry of thickness 10 nm, at a constant external field 400 mT in negative z direction, without thickness barrier at the edge. (a) The isolated skyrmion state stabilized at the given external field in the disc geometry shown with the help of a color-map with respect to m_z . (b)-(e) The four magnetization modes of the skyrmion state represented with amplitude of δm_z . The CCW gyrotropic mode has frequency 1 GHz, the CW azimuthal mode has frequency 5.58 GHz, and the breathing as well as the second order breathing mode has frequencies 5.67 GHz and 22.91 GHz respectively.

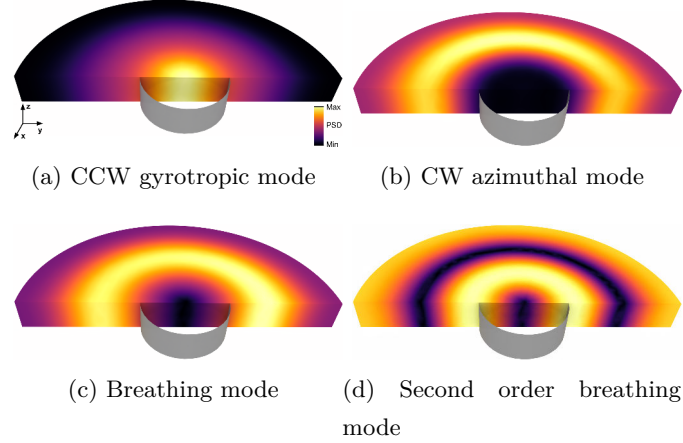


FIGURE 7.18 – Geometric distribution of power in the disc geometry of uniform thickness for the magnetization modes of the skyrmion state. The gray iso-surface corresponds to $m_z = 0$. With the help of the iso-surface, one may identify regions of activity compared to the skyrmion core.

all the cases.

For the barrier disc geometry, in the case of CCW gyrotropic mode, the frequency increases, and the amplitude decreases nonlinearly with increasing barrier width. The amplitude is maximum and frequency is minimum at 1 GHz in the case of uniformly thick disc. We have already discussed how the thickness barrier can create a potential well for an isolated skyrmion in section 7.3. Hence, we assume that the increasing width of the thickness barrier leads to a steeper potential well, ultimately resulting in a smaller amplitude and higher frequency of the gyrotropic mode with an identical excitation. One can roughly compare it to an object's harmonic motion obeying Hook's law with an increasing spring constant. However, it is crucial to keep in mind that a rigid skyrmion's particle treatment follows the Thiele equation [26], and hence, it is non-Newtonian. For the CW asymmetric azimuthal mode, the frequency decreases with increasing barrier width. On an average, the mode's Fourier amplitude is 18 times higher in the case of a uniformly thick disc compared to the disc with a thickness barrier. In the barrier's presence, it stays constant till width 20 nm and then becomes 1.5 times for width 25 nm, which could be due to the change in region of maximum activity from thinner disc region to the thicker barrier region with increasing barrier width. Obviously, the barrier mode disappears as the barrier thickness is reduced to zero. It

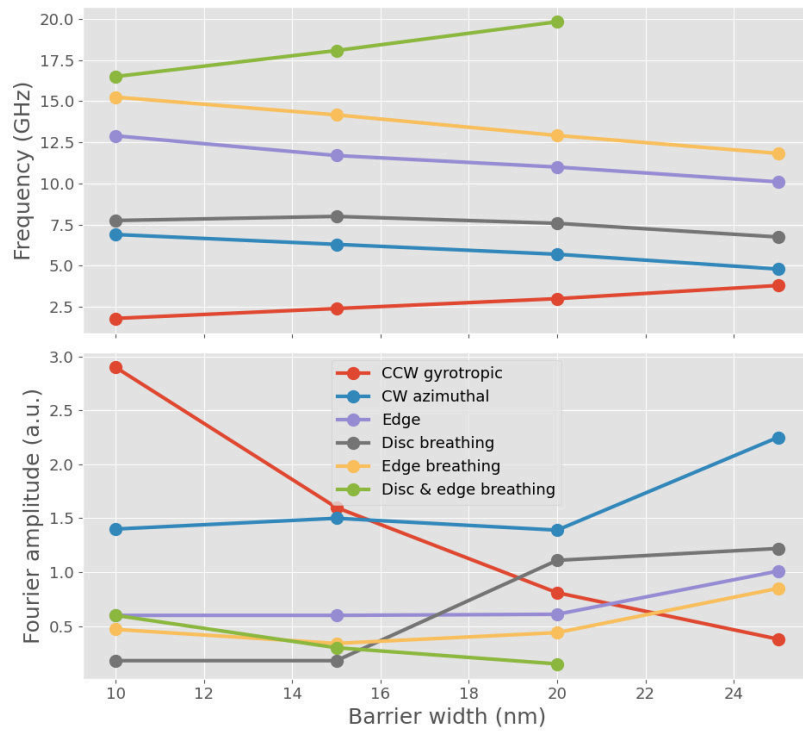


FIGURE 7.19 – The plot shows the trends in the frequency and Fourier amplitude of the six magnetization modes of the skyrmion state in the barrier disc geometry with changing barrier width. The plot confirms that the width of the barrier affects both frequency and amplitude of the confined skyrmion modes. The possibility to tune the skyrmion modes through material geometry can prove to be significant for communication and signal processing devices based on spintronics.

follows a similar frequency and amplitude trend as the CW azimuthal mode with a thickness barrier, where its frequency is always higher and the amplitude always lower than the later. The disc breathing mode is observed in both the disc with and without the thickness barrier. The frequency of the mode is always higher in the presence of the barrier, however, the amplitude is lower up till the barrier width 15 nm and then becomes higher compared to the disc without barrier. Although not shown explicitly, we observe, with increasing barrier width, the region of maximum activity (Fourier amplitude) of the disc breathing mode is no longer limited to the thinner disc region (Fig. 7.16(d)); instead it is shared by the disc and the barrier region. We observe this change going from 15 nm to 20 nm barrier width, which could be the reason for the increase in the amplitude. Similarly, the initial increase and subsequent decrease in the frequency of the mode can be attributed to this effect. As expected, the edge breathing mode follows a similar trend for the amplitude and frequency as the edge mode given the similar region of activity. The main difference is lower amplitude and higher frequency. Also, the edge breathing mode is not observed in the disc without the thickness barrier. Instead, in the case of the disc with uniform thickness, we observe a higher order breathing mode with two spatial nodes in the radial direction with an in-phase oscillation of the magnetization (Fig. 7.17(e) & Fig. 7.18(d)). Finally, the disc & edge breathing mode shows an increasing frequency and a decreasing amplitude trend with increasing thickness barrier up till barrier width 20 nm; after which the mode is not observed.

Hence, we see that the geometric confinement affects the frequency and amplitude of different dynamical modes of the isolated skyrmion. Not only do we observe the novel barrier modes, but the confinement also affects the frequency and the Fourier amplitude of the previously known dynamical modes in a disc geometry of uniform thickness. One may attribute this to the changing isolated skyrmion structure with changing thickness barrier width (not shown). From a signal processing and communication device application point of view, the possibility to tune the frequency of the modes by varying the barrier width can be significant. Further, the CCW gyrotropic mode has been shown to act as a soft mode for skyrmion core switching in confined geometry [138] or melting of the skyrmion crystal phase in extended geometry [132]. One can drive down the mode's Fourier amplitude by introducing the thickness barrier, as discussed above. Hence, one may argue that a thickness barrier enhances the skyrmion's stability against an

7.4 Dynamic skyrmion confinement

external perturbation, which is relevant to magnetic recording devices.

CHAPITRE 8

Conclusion

With the increasing possibility to stabilize and study three-dimensional geometries of magnetic materials due to substantial progress in fabrication, characterization, imaging, and simulation techniques, in this thesis, our aim was to study the stabilization and dynamic properties of three-dimensional skyrmions in confined geometries through FEM/BEM micromagnetic simulations. The materials with bulk Dzyaloshinskii-Moriya interaction (DMI) host three-dimensional skyrmions due to inherent spatial inversion symmetry breaking (FeGe for our study, a B20 type non-centrosymmetric ferromagnet). We found that the skyrmion state stability depends primarily on the external magnetic field strength (in the absence of magnetocrystalline anisotropy) and the material geometry dimensions. Utilizing this fact, we propose a way to constrain the skyrmions statically through geometry modulation and study their constrained state dynamics. Further, due to competing symmetric exchange interaction and anti-symmetric DMI, we found other chiral magnetization structures such as helical, (bi)meron, and chiral bobber states in the 3D geometries of FeGe. Hence, in addition to studying the static and dynamic properties of the skyrmions, we also present the study of (meta-)stability and evolution of these states with varying external field and geometric dimensions.

The synopsis of the study presented in the thesis is as follows :

1. The study of chiral magnetization states, including skyrmion state, in FeGe nanospheres ;
2. The study of skyrmion and chiral bobber state switching, two proposed fundamental units of information storage, in nanodisc geometry ;
3. The study of the static and dynamic properties of geometrically constrained skyrmions, guided or pinned by means of film thickness modulation.

Three-dimensional chiral magnetization states in FeGe nanosphere are presented in chapter 5. We found five principal equilibrium magnetization states : helical, meron, skyrmion, chiral bobber, and quasi-saturation state, in FeGe nanosphere geometry. The change in the magnetization structure of the ground state is described with increasing external field, and a phase diagram of the equilibrium states as ground states is presented with changing external field values and the nanosphere radius. We further look at a cross-section of the phase diagram, where we found that the chiral equilibrium states with non-trivial topology (i.e., skyrmion, chiral bobber, and meron state) are stabilized as meta-stable states over an extended range of external field and radius values. Finally, we study the impact of magnetostatic interactions on the sta-

tes' stability, where we found that it does not impact the phase diagram appreciably. However, the impact of magnetostatic interactions cannot be ignored for flat confined geometries. The study highlights the impact of the external field and material geometry on the skyrmion state's stability and others. We showed with the help of FeGe nanospheres that it is possible to obtain five principle equilibrium states, including the 3D skyrmion state, in isolation due to the finite size of the geometry. This opens an avenue for the further study of the fundamental magnetic properties of individual equilibrium states, for example, the magnetization modes.

Skyrmion and chiral bobber state switching is presented in chapter 6. Chapter 5 discusses how the external magnetic field impacts the magnetization structures of the skyrmion and chiral bobber states and the phase diagram regions where they are the ground states. However, due to non-trivial topology and a Bloch point in the chiral bobber state, one needs to overcome an energy barrier to switch between the states. We found that it is possible to achieve this switching with magnetic field pulses in a FeGe nanodisc geometry. First, we modulate the external field to adjust the total energies of the skyrmion and chiral bobber state such that one becomes energetically favorable over the other and then overcome the topological barrier with an additional Gaussian field pulse. We found that the direction of the gaussian field pulse required for the transition from skyrmion to chiral bobber state is perpendicular to the skyrmion axis, while the chiral bobber to skyrmion state is parallel to the skyrmion axis. The control over the switching of the two states with a field pulse may have technological implications. The switching process discussed here involves complex Bloch point (BP) dynamics. We find that the BP is injected from a fixed surface with regards to the external field direction and the sign of the DMI constant. This points towards the fact that both top and bottom surfaces of the 3D skyrmion have different contributions to the total energy of the system, i.e., one surface has lower energy than the other. Such asymmetry in the total energy contribution of a 3D magnetization structure of a skyrmion has not yet been discussed in the literature and can be important from both fundamental physics as well as application points of view.

The study of geometrically constrained skyrmions is presented in chapter 7. This chapter proposes a method to constrain the skyrmions to the desired region of the material geometry utilizing thickness modulations and the study of thus constrained skyrmion dynamics. We begin the study with a phase diagram showing magnetization

ground state distribution for a rectangular FeGe film with changing external field and thickness; the film's lateral dimensions stay constant. We primarily focus on whether the skyrmion or the saturation state is energetically favorable depending on the film thickness at a constant external field. Above a specific external field value, the skyrmion state is energetically favorable in thinner films than the thicker ones. Hence, we introduce local regions of reduced thickness in a relatively thick film, in the form of circular pockets and narrow paths, as the desired regions of skyrmion stability. Once these regions capture the skyrmions, they stay confined to them. First, we present the study of cylindrical pockets of reduced thickness in the film. The pockets can be arranged in various ways on a rectangular film to create a complex skyrmion arrangement compared to the natural hexagonal skyrmion crystal—for example, a square lattice or diagonal arrangement. Subsequently, we present the study of three example geometries where a thin and narrow path is carved out of the thick films as the desired regions of skyrmion stability. Again, we found that once the skyrmions are captured on the path, they stay confined to it. The three path geometries mentioned above are linear, angled, and curved path geometries, which again deviate from the natural hexagonal skyrmion crystal arrangement. Further, we plot the energy barrier faced by the skyrmion due to the thickness modulations in the linear path geometry at a fixed external field and compare it with a film without thickness modulation. We found that the skyrmions indeed face a substantially higher energy barrier in the former case. The study presented here is especially useful where the control over the positions of the skyrmions is required to form definite skyrmion arrangements. Two of such cases where the skyrmion arrangement may be of interest are magnonics, where a particular skyrmion arrangement can form a magnonics crystal whose magnon dispersion relation depends on the skyrmion arrangement, and the emerging field of skyrmion based physical reservoir computing where the nonlinear current-voltage relationship of the device due to anisotropic magnetoresistance (AMR) [218] depends on the arrangement and position of the skyrmions in the physical reservoir.

To study the constrained skyrmions dynamics, we take inspiration from the linear path geometry and propose a new H-shaped skyrmion racetrack where the skyrmions stay confined to the thin central path when displaced with spin-polarized currents. The thickness barriers at the lateral edges counter the unwanted skyrmion Hall effect (SkHE), which typically pushes out skyrmions from the edges. In the presence of the

thickness barrier, we found that it requires four times higher current density to expel skyrmions from the edges due to SkHE. We plot the skyrmion velocity with current density and beta/alpha ratio, and in both cases, we found that the velocity scales linearly. We further show this relationship can be analytically derived from Thiele's equation for an isolated skyrmion motion in the track. With our preliminary calculations (not presented in the thesis), we find that it is also possible to pin the position of skyrmions on the thin central track with the help of shallow circular pockets with an equidistant linear arrangement. The pinning of the skyrmions is essential to counter the undesirable skyrmion thermal diffusion and form an ordered (and thus readable) pattern of skyrmions on the track. With a finite square current pulse, the skyrmions can be moved between the pockets preserving the pattern. Moreover, our preliminary calculations show that it is possible to nucleate skyrmions in the H-track geometry from cylindrical notches in the track by decreasing the total external field. In this way, one can present a coherent skyrmion-based racetrack device concept where the thickness modulations can be used to counter the unwanted skyrmion Hall effect and thermal diffusion to form an ordered and readable skyrmion pattern on the track. The width of the thin central track, the depth of the pinning pockets, the strength and profile of the square current pulse, and different non-centrosymmetric ferromagnets as a material of choice for the device are a few parameters that still needs to be studied comprehensively to obtain a practical racetrack device. Finally, we study the constrained skyrmion's magnetization modes in a nanodisc geometry with the thickness barrier at the edge. The geometry resembles the nano pockets discussed earlier ; however, we study an isolated constrained skyrmion in the present case. We identify six modes, three lateral and three breathing, two of which can only be observed in the thickness barrier's presence. Further, we found that one can tune the frequency of the modes and response to an external perturbation by changing the thickness barrier's width. This study can be extended to obtain a geometry with multiple constrained skyrmions in pockets of varying radii where the Fourier spectrum of the collective modes may show multiple peaks corresponding to the distribution of the pockets' radii. One can further opt to create a fractal-based geometry, for example, where the thin pockets form an Apollonian gasket, which has a large distribution of the radii for finite dimensions of the device and hence obtain a large distribution of the eigenmode frequencies.

In conclusion, we present a comprehensive study of three-dimensional skyrmions

in confined geometries. Besides, we also identify various equilibrium states like the helical, (bi)meron, and chiral bobber state, that are stabilized in materials hosting three-dimensional helimagnetic structures. We utilize the external field dependence of the total energy of the skyrmion state to achieve controlled switching of the skyrmion state to the chiral bobber state. Further, we utilize the geometry dependence of the total energy to constrain skyrmions to the desired regions. This possibility to manipulate the position of the skyrmions can be quite useful for device applications. The statically constrained skyrmions in different arrangements of the pockets and the narrow paths have the potential to form magnonic crystals and physical RC, as well as the dynamics of the constrained skyrmions in the H-shaped racetrack geometry to counter SkHE and the possibility to tune the frequency of the skyrmion magnetization modes in barrier disc geometry may find application in magnetic storage and RF devices.

REFERENCES

- [1] Muhlbauer, S. *et al.* Skyrmion Lattice in a Chiral Magnet. *Science* **323**, 915–919 (2009).
- [2] Yu, X. *et al.* Skyrmion flow near room temperature in an ultralow current density. *Nat Commun* **3**, 988 (2012).
- [3] Heinze, S. *et al.* Spontaneous atomic-scale magnetic skyrmion lattice in two dimensions. *Nature Phys* **7**, 713–718 (2011).
- [4] Budhathoki, S. *et al.* Room-temperature skyrmions in strain-engineered FeGe thin films. *Phys. Rev. B* **101**, 220405 (2020).
- [5] Yu, X. Z. *et al.* Near room-temperature formation of a skyrmion crystal in thin-films of the helimagnet FeGe. *Nature Materials* **10**, 106–109 (2011).
- [6] Zhang, S. L. *et al.* Room-temperature helimagnetism in FeGe thin films. *Sci Rep* **7**, 123 (2017).
- [7] Fert, A., Cros, V. & Sampaio, J. Skyrmions on the track. *Nature Nanotechnology* **8**, 152–156 (2013).
- [8] Garcia-Sanchez, F., Sampaio, J., Reyren, N., Cros, V. & Kim, J. A skyrmion-based spin-torque nano-oscillator. *New Journal of Physics* **18**, 075011 (2016).
- [9] Guslienko, K. Y. Magnetic skyrmion spin-torque nano-oscillators. *physica status solidi (RRL)–Rapid Research Letters* **14**, 2000032 (2020).
- [10] Zhang, X., Ezawa, M. & Zhou, Y. Magnetic skyrmion logic gates : conversion, duplication and merging of skyrmions. *Scientific reports* **5**, 1–8 (2015).

-
- [11] Zhang, X., Zhou, Y., Ezawa, M., Zhao, G. & Zhao, W. Magnetic skyrmion transistor : skyrmion motion in a voltage-gated nanotrack. *Scientific reports* **5**, 11369 (2015).
- [12] Zhou, Y. & Ezawa, M. A reversible conversion between a skyrmion and a domain-wall pair in a junction geometry. *Nature communications* **5**, 1–8 (2014).
- [13] Li, S. *et al.* Magnetic skyrmions for unconventional computing. *Materials Horizons* (2020).
- [14] Fernández-Pacheco, A. *et al.* Three-dimensional nanomagnetism. *Nature Communications* **8**, 1–14 (2017).
- [15] Sanz-Hernández, D. *et al.* Artificial double-helix for geometrical control of magnetic chirality. *ACS nano* **14**, 8084–8092 (2020).
- [16] Brown, W. f. *Micromagnetics, by w.f. brown* (Interscience, 1963).
- [17] Gilbert, T. Classics in Magnetism A Phenomenological Theory of Damping in Ferromagnetic Materials. *IEEE Trans. Magn.* **40**, 3443–3449 (2004).
- [18] Bogdanov, A. N. & Yablonskii, D. A. Thermodynamically stable "vortices" in magnetically ordered crystals. The mixed state of magnets. *Sov. Phys. JETP* **68**, 101–103 (1989).
- [19] Bogdanov, A. N. & Röbber, U. K. Chiral Symmetry Breaking in Magnetic Thin Films and Multilayers. *Physical Review Letters* **87** (2001).
- [20] Bogdanov, A. & Hubert, A. The stability of vortex-like structures in uniaxial ferromagnets. *Journal of Magnetism and Magnetic Materials* **195**, 182–192 (1999).
- [21] Bogdanov, A. & Hubert, A. Thermodynamically stable magnetic vortex states in magnetic crystals. *Journal of Magnetism and Magnetic Materials* **138**, 255–269 (1994).
- [22] Leonov, A. O. *et al.* The properties of isolated chiral skyrmions in thin magnetic films. *New J. Phys.* **18**, 065003 (2016).
- [23] Yu, X. Z. *et al.* Real-space observation of a two-dimensional skyrmion crystal. *Nature* **465**, 901–904 (2010).

-
- [24] Seki, S., Yu, X. Z., Ishiwata, S. & Tokura, Y. Observation of Skyrmions in a Multiferroic Material. *Science* **336**, 198–201 (2012).
- [25] Berry, M. V. Quantal phase factors accompanying adiabatic changes. *Proc. R. Soc. Lond. A* **392**, 45–57 (1984).
- [26] Thiele, A. A. Steady-State Motion of Magnetic Domains. *Phys. Rev. Lett.* **30**, 230–233 (1973).
- [27] Hertel, R. *Statische und dynamische Magnetisierung in Nanostrukturen*. Habilitation thesis, Halle (Saale), Univ. (2005). URL <http://d-nb.info/984223096>.
- [28] Hertel, R. Micromagnetic simulations of magnetostatically coupled Nickel nanowires. *Journal of Applied Physics* **90**, 5752 (2001). URL <http://link.aip.org/link/JAPIAU/v90/i11/p5752/s1&Agg=doi>.
- [29] Hertel, R. Guided Spin Waves. In *Handbook of Magnetism and Advanced Magnetic Materials* (John Wiley & Sons, Ltd, 2007). URL <http://onlinelibrary.wiley.com/doi/10.1002/9780470022184.hmm212/abstract>.
- [30] Hertel, R., Christophersen, S. & Börm, S. Large-scale magnetostatic field calculation in finite element micromagnetics with H²-matrices. *Journal of Magnetism and Magnetic Materials* **477**, 118–123 (2019).
- [31] Cortés-Ortuño, D. I. *et al.* Proposal for a micromagnetic standard problem for materials with Dzyaloshinskii-Moriya interaction. *New Journal of Physics* (2018).
- [32] Vansteenkiste, A. *et al.* The design and verification of MuMax3. *AIP Advances* **4**, 107133 (2014). URL <http://aip.scitation.org/doi/full/10.1063/1.4899186>.
- [33] M Donahue & Porter, D. OOMMF User’s Guide, Version 1.0 (1999). URL <http://math.nist.gov/oommf/>.
- [34] muMAG Micromagnetics Website. URL <https://www.ctcms.nist.gov/~rdm/mumag.org.html>.
- [35] Rybakov, F. N., Borisov, A. B., Blügel, S. & Kiselev, N. S. New Type of Stable Particlelike States in Chiral Magnets. *Physical Review Letters* **115** (2015).

-
- [36] Rybakov, F. N., Borisov, A. B., Blügel, S. & Kiselev, N. S. New spiral state and skyrmion lattice in 3D model of chiral magnets. *New Journal of Physics* **18**, 045002 (2016).
- [37] Zheng, F. *et al.* Experimental observation of chiral magnetic bobbbers in B20-type FeGe. *Nature Nanotechnology* **13**, 451–455 (2018).
- [38] Redies, M. *et al.* Distinct magnetotransport and orbital fingerprints of chiral bobbbers. *Physical Review B* **99**, 140407 (2019).
- [39] Everschor-Sitte, K. & Sitte, M. Real-space berry phases : Skyrmion soccer. *Journal of Applied Physics* **115**, 172602 (2014).
- [40] Song, C. *et al.* Commensurability between element symmetry and the number of skyrmions governing skyrmion diffusion in confined geometries. *Advanced Functional Materials* 2010739 (2021).
- [41] Suess, D., Vogler, C., Bruckner, F., Heistracher, P. & Slanovc, F. Spin torque efficiency and analytic error rate estimates of skyrmion racetrack memory. *Scientific reports* **9**, 1–17 (2019).
- [42] Legrand, W. *et al.* Room-temperature stabilization of antiferromagnetic skyrmions in synthetic antiferromagnets. *Nature materials* **19**, 34–42 (2020).
- [43] Pathak, S. A. & Hertel, R. Three-dimensional chiral magnetization structures in fege nanospheres. *Physical Review B* **103**, 104414 (2021).
- [44] Juge, R. *et al.* Magnetic skyrmions in confined geometries : Effect of the magnetic field and the disorder. *Journal of Magnetism and Magnetic Materials* **455**, 3–8 (2018).
- [45] Beg, M. *et al.* Ground state search, hysteretic behaviour, and reversal mechanism of skyrmionic textures in confined helimagnetic nanostructures. *Scientific Reports* **5** (2015).
- [46] Rybakov, F. N., Borisov, A. B. & Bogdanov, A. N. Three-dimensional skyrmion states in thin films of cubic helimagnets. *Physical Review B* **87** (2013).
- [47] Jin, C. *et al.* Control of morphology and formation of highly geometrically confined magnetic skyrmions. *Nature communications* **8**, 1–9 (2017).

-
- [48] Zhang, X. *et al.* Skyrmion-skyrmion and skyrmion-edge repulsions in skyrmion-based racetrack memory. *Scientific reports* **5**, 1–6 (2015).
- [49] Coey, J. M. *Magnetism and magnetic materials* (Cambridge university press, 2010).
- [50] Guimarães, A. P. & Guimaraes, A. P. *Principles of nanomagnetism*, vol. 7 (Springer, 2009).
- [51] Cullity, B. D. & Graham, C. D. *Introduction to magnetic materials* (John Wiley & Sons, 2011).
- [52] Stöhr, J. & Siegmann, H. C. Magnetism. *Solid-State Sciences. Springer, Berlin, Heidelberg* **5** (2006).
- [53] Abeed, M. A., Sahoo, S., Winters, D., Barman, A. & Bandyopadhyay, S. The effect of material defects on resonant spin wave modes in a nanomagnet. *Scientific reports* **9**, 1–10 (2019).
- [54] Apolonio, F., Moura-Melo, W., Crisafuli, F., Pereira, A. & Silva, R. A model for structural defects in nanomagnets. *Journal of Applied Physics* **106**, 084320 (2009).
- [55] Jorzick, J. *et al.* Spin wave quantization in laterally confined magnetic structures. *Journal of Applied Physics* **89**, 7091–7095 (2001).
- [56] Néel, L. Théorie du traînage magnétique des ferromagnétiques en grains fins avec applications aux terres cuites. *Ann. géophys.* **5**, 99–136 (1949).
- [57] Brown Jr, W. F. Thermal fluctuations of a single-domain particle. *Physical review* **130**, 1677 (1963).
- [58] Sellmyer, D. J. & Skomski, R. *Advanced magnetic nanostructures* (Springer Science & Business Media, 2006).
- [59] Bader, S. & Parkin, S. Spintronics. *Annual Review of Condensed Matter Physics* **1**, 71–88 (2010).
- [60] Moodera, J. S., Kinder, L. R., Wong, T. M. & Meservey, R. Large magnetoresistance at room temperature in ferromagnetic thin film tunnel junctions. *Physical Review Letters* **74**, 3273 (1995).

-
- [61] Miyazaki, T. & Tezuka, N. Giant magnetic tunneling effect in Fe/Al₂O₃/Fe junction. *Journal of magnetism and magnetic materials* **139**, L231–L234 (1995).
- [62] Butler, W., Zhang, X.-G., Schulthess, T. & MacLaren, J. Spin-dependent tunneling conductance of Fe/MgO/Fe sandwiches. *Physical Review B* **63**, 054416 (2001).
- [63] Mathon, J. & Umerski, A. Theory of tunneling magnetoresistance of an epitaxial Fe/MgO/Fe (001) junction. *Physical Review B* **63**, 220403 (2001).
- [64] Ikeda, S. *et al.* Tunnel magnetoresistance of 604% at 300 K by suppression of ta diffusion in CoFeB/MgO/CoFeB pseudo-spin-valves annealed at high temperature. *Applied Physics Letters* **93**, 082508 (2008).
- [65] Jiang, L., Naganuma, H., Oogane, M. & Ando, Y. Large tunnel magnetoresistance of 1056% at room temperature in mgo based double barrier magnetic tunnel junction. *Applied physics express* **2**, 083002 (2009).
- [66] Berger, L. Emission of spin waves by a magnetic multilayer traversed by a current. *Phys. Rev. B* **54**, 9353–9358 (1996).
- [67] Slonczewski, J. Current-driven excitation of magnetic multilayers. *Journal of Magnetism and Magnetic Materials* **159**, L1–L7 (1996).
- [68] Parkin, S. S., Hayashi, M. & Thomas, L. Magnetic domain-wall racetrack memory. *Science* **320**, 190–194 (2008).
- [69] Sampaio, J., Cros, V., Rohart, S., Thiaville, A. & Fert, A. Nucleation, stability and current-induced motion of isolated magnetic skyrmions in nanostructures. *Nature nanotechnology* **8**, 839–844 (2013).
- [70] Wiesendanger, R. Nanoscale magnetic skyrmions in metallic films and multilayers : a new twist for spintronics. *Nature Reviews Materials* **1**, 1–11 (2016).
- [71] Heinze, S. *et al.* Spontaneous atomic-scale magnetic skyrmion lattice in two dimensions. *Nature Physics* **7**, 713–718 (2011).
- [72] Boulle, O. *et al.* Room-temperature chiral magnetic skyrmions in ultrathin magnetic nanostructures. *Nature nanotechnology* **11**, 449 (2016).

-
- [73] Jiang, W. *et al.* Mobile néel skyrmions at room temperature : status and future. *AIP Advances* **6**, 055602 (2016).
- [74] Utke, I., Hoffmann, P. & Melngailis, J. Gas-assisted focused electron beam and ion beam processing and fabrication. *Journal of Vacuum Science & Technology B : Microelectronics and Nanometer Structures Processing, Measurement, and Phenomena* **26**, 1197–1276 (2008).
- [75] Donnelly, C. *et al.* Element-specific x-ray phase tomography of 3d structures at the nanoscale. *Physical Review Letters* **114**, 115501 (2015).
- [76] Liakakos, N. *et al.* Solution epitaxial growth of cobalt nanowires on crystalline substrates for data storage densities beyond 1 tbit/in². *Nano letters* **14**, 3481–3486 (2014).
- [77] Mistonov, A. *et al.* Three-dimensional artificial spin ice in nanostructured co on an inverse opal-like lattice. *Physical Review B* **87**, 220408 (2013).
- [78] Wernsdorfer, W. *et al.* Nucleation of magnetization reversal in individual nano-sized nickel wires. *Physical Review Letters* **77**, 1873 (1996).
- [79] Fernández-Pacheco, A. *et al.* Three dimensional magnetic nanowires grown by focused electron-beam induced deposition. *Scientific reports* **3**, 1492 (2013).
- [80] Midgley, P. A. & Dunin-Borkowski, R. E. Electron tomography and holography in materials science. *Nature materials* **8**, 271–280 (2009).
- [81] Streubel, R. *et al.* Equilibrium magnetic states in individual hemispherical permalloy caps. *Applied Physics Letters* **101**, 132419 (2012).
- [82] Kimling, J. *et al.* Photoemission electron microscopy of three-dimensional magnetization configurations in core-shell nanostructures. *Physical Review B* **84**, 174406 (2011).
- [83] Streubel, R. *et al.* Retrieving spin textures on curved magnetic thin films with full-field soft x-ray microscopies. *Nature communications* **6**, 1–11 (2015).
- [84] Andreas, C., Kákay, A. & Hertel, R. Multiscale and multimodel simulation of Bloch-point dynamics. *Phys. Rev. B* **89**, 134403 (2014).

-
- [85] Landau, L. On the theory of the dispersion of magnetic permeability in ferromagnetic bodies. *Perspectives in Theoretical Physics* 15.
- [86] Griffiths, D. J. *Introduction to Quantum Mechanics* (Cambridge University Press, 2017).
- [87] Abert, C. Micromagnetics and spintronics : models and numerical methods. *The European Physical Journal B* **92**, 1–45 (2019).
- [88] Hubert, A. & Schäfer, R. *Magnetic Domains : The Analysis of Magnetic Microstructures* (Springer Science & Business Media, 2008).
- [89] Dzyaloshinsky, I. A thermodynamic theory of weak ferromagnetism of antiferromagnetics. *Journal of Physics and Chemistry of Solids* **4**, 241–255 (1958).
- [90] Moriya, T. Anisotropic superexchange interaction and weak ferromagnetism. *Physical Review* **120**, 91 (1960).
- [91] Yu, X. *et al.* Magnetic stripes and skyrmions with helicity reversals. *Proceedings of the National Academy of Sciences* **109**, 8856–8860 (2012).
- [92] Landau, L. & Lifshitz, E. *Statistical physics 3rd ed* (Pergamon : Oxford, 1980).
- [93] Bogdanov, A. N., Röbner, U. K., Wolf, M. & Müller, K. H. Magnetic structures and reorientation transitions in noncentrosymmetric uniaxial antiferromagnets. *Phys. Rev. B* **66**, 214410 (2002).
- [94] Brown, W. F. *Magnetostatic Principles in Ferromagnetism* (North-Holland Publishing Company, 1962).
- [95] Brown, W. F. Criterion for Uniform Micromagnetization. *Phys. Rev.* **105**, 1479–1482 (1957).
- [96] Forman, P. Alfred Landé and the Anomalous Zeeman Effect, 1919-1921. *Historical Studies in the Physical Sciences* 153–261 (1970).
- [97] Bland, A. & Heinrich, B. (eds.) *Ultrathin magnetic structures* (Springer, Berlin ; New York, 1994).
- [98] Zhang, S. & Li, Z. Roles of Nonequilibrium Conduction Electrons on the Magnetization Dynamics of Ferromagnets. *Phys. Rev. Lett.* **93**, 127204 (2004).

-
- [99] Najafi, M. *et al.* Proposal for a standard problem for micromagnetic simulations including spin-transfer torque. *Journal of Applied Physics* **105**, 113914 (2009).
- [100] Wilhelm, H. *et al.* Confinement of chiral magnetic modulations in the precursor region of FeGe. *Journal of Physics : Condensed Matter* **24**, 294204 (2012).
- [101] Weiss, P. La variation du ferromagnetisme du temperature. *Comptes Rendus* **143**, 1136 (1906).
- [102] Bloch, F. Zur theorie des austauschproblems und der remanenzerscheinung der ferromagnetika. *Zeitschrift für Physik* **74**, 295 (1932).
- [103] Néel, L. L'anisotropie superficielle des substances ferromagnétiques. *CR Acad. Sci. Paris* **237**, 1468 (1953).
- [104] Thiaville, A. & Garc, J. M. Domain wall dynamics in nanowires. *Journal of Magnetism and Magnetic Materials* **3** (2002).
- [105] Aharoni, A. *Introduction to the Theory of Ferromagnetism* (Clarendon Press, 2000).
- [106] Lilley, B. Energies and widths of domain boundaries in ferromagnetics. *Philosophical Magazine Series 7* **41**, 792 (1950).
- [107] Skyrme, T. A unified field theory of mesons and baryons. *Nuclear Physics* **31**, 556–569 (1962).
- [108] Skyrme, T. A non-linear field theory. *Proc. R. Soc. Lond. A* **260**, 127–138 (1961).
- [109] Wright, D. C. & Mermin, N. D. Crystalline liquids : the blue phases. *Rev. Mod. Phys.* **61**, 385–432 (1989).
- [110] Ho, T.-L. Spinor Bose Condensates in Optical Traps. *Physical Review Letters* **81**, 4 (1998).
- [111] Sondhi, S. L., Karlhede, A., Kivelson, S. A. & Rezayi, E. H. Skyrmions and the crossover from the integer to fractional quantum Hall effect at small Zeeman energies. *Phys. Rev. B* **47**, 16419–16426 (1993).

-
- [112] Abolfath, M., Palacios, J. J., Fertig, H. A., Girvin, S. M. & MacDonald, A. H. Critical comparison of classical field theory and microscopic wave functions for skyrmions in quantum Hall ferromagnets. *Phys. Rev. B* **56**, 6795–6804 (1997).
- [113] Remoissenet, M. *Waves Called Solitons : Concepts and Experiments* (Springer Science & Business Media, 2013).
- [114] Derrick, G. H. Comments on Nonlinear Wave Equations as Models for Elementary Particles. *Journal of Mathematical Physics* **5**, 1252–1254 (1964).
- [115] Bak, P. & Jensen, M. H. Theory of helical magnetic structures and phase transitions in mnsi and fege. *Journal of Physics C : Solid State Physics* **13**, L881 (1980).
- [116] Rybakov, F. N. & Kiselev, N. S. Chiral magnetic skyrmions with arbitrary topological charge. *Phys. Rev. B* **99**, 064437 (2019).
- [117] Kézsmárki, I. *et al.* Néel-type skyrmion lattice with confined orientation in the polar magnetic semiconductor GaV4S8. *Nature Mater* **14**, 1116–1122 (2015).
- [118] Nayak, A. K. *et al.* Magnetic antiskyrmions above room temperature in tetragonal Heusler materials. *Nature* **548**, 561–566 (2017).
- [119] Schulz, T. *et al.* Emergent electrodynamics of skyrmions in a chiral magnet. *Nature Phys* **8**, 301–304 (2012).
- [120] Iwasaki, J., Mochizuki, M. & Nagaosa, N. Universal current-velocity relation of skyrmion motion in chiral magnets. *Nat Commun* **4**, 1463 (2013).
- [121] Leonov, A. & Mostovoy, M. Multiply periodic states and isolated skyrmions in an anisotropic frustrated magnet. *Nature communications* **6**, 1–8 (2015).
- [122] Batista, C. D., Lin, S.-Z., Hayami, S. & Kamiya, Y. Frustration and chiral orderings in correlated electron systems. *Reports on Progress in Physics* **79**, 084504 (2016).
- [123] Ozawa, R., Hayami, S. & Motome, Y. Zero-field skyrmions with a high topological number in itinerant magnets. *Physical Review Letters* **118**, 147205 (2017).

-
- [124] Kang, W., Huang, Y., Zhang, X., Zhou, Y. & Zhao, W. Skyrmion-electronics : An overview and outlook. *Proceedings of the IEEE* **104**, 2040–2061 (2016).
- [125] Rybakov, F. N. *et al.* Magnetic hopfions in solids. *arXiv :1904.00250 [cond-mat, physics :nlin]* (2019). ArXiv : 1904.00250.
- [126] Bauer, A. & Pfleiderer, C. Generic aspects of skyrmion lattices in chiral magnets. In *Topological Structures in Ferroic Materials*, 1–28 (Springer, 2016).
- [127] Karube, K. *et al.* Robust metastable skyrmions and their triangular–square lattice structural transition in a high-temperature chiral magnet. *Nature materials* **15**, 1237–1242 (2016).
- [128] Oike, H. *et al.* Interplay between topological and thermodynamic stability in a metastable magnetic skyrmion lattice. *Nature Phys* **12**, 62–66 (2016).
- [129] Chacon, A. *et al.* Observation of two independent skyrmion phases in a chiral magnetic material. *Nature Physics* **14**, 936–941 (2018).
- [130] Iwasaki, J., Mochizuki, M. & Nagaosa, N. Current-induced skyrmion dynamics in constricted geometries. *Nature Nanotech* **8**, 742–747 (2013).
- [131] Neubauer, A. *et al.* Topological hall effect in the a phase of mnsi. *Physical Review Letters* **102**, 186602 (2009).
- [132] Mochizuki, M. Spin-wave modes and their intense excitation effects in skyrmion crystals. *Physical Review Letters* **108**, 017601 (2012).
- [133] Kim, J.-V. *et al.* Breathing modes of confined skyrmions in ultrathin magnetic dots. *Physical Review B* **90**, 064410 (2014).
- [134] Mochizuki, M. & Seki, S. Dynamical magnetoelectric phenomena of multiferroic skyrmions. *Journal of Physics : Condensed Matter* **27**, 503001 (2015).
- [135] Onose, Y., Okamura, Y., Seki, S., Ishiwata, S. & Tokura, Y. Observation of magnetic excitations of skyrmion crystal in a helimagnetic insulator cu 2 oseo 3. *Physical Review Letters* **109**, 037603 (2012).
- [136] Okamura, Y. *et al.* Microwave magnetoelectric effect via skyrmion resonance modes in a helimagnetic multiferroic. *Nature Communications* **4**, 1–6 (2013).

-
- [137] Schwarze, T. *et al.* Universal helimagnon and skyrmion excitations in metallic, semiconducting and insulating chiral magnets. *Nature materials* **14**, 478–483 (2015).
- [138] Beg, M. *et al.* Dynamics of skyrmionic states in confined helimagnetic nanostructures. *Physical Review B* **95**, 014433 (2017).
- [139] Guslienko, K. Y. & Gareeva, Z. V. Gyrotropic skyrmion modes in ultrathin magnetic circular dots. *IEEE Magnetics Letters* **8**, 1–5 (2016).
- [140] Xuan, S. & Liu, Y. Nonuniform gyrotropic oscillation of skyrmion in a nanodisk. *AIP Advances* **8**, 045312 (2018).
- [141] Moon, K.-W., Chun, B. S., Kim, W., Qiu, Z. & Hwang, C. Control of skyrmion magnetic bubble gyration. *Physical Review B* **89**, 064413 (2014).
- [142] Makhfudz, I., Krüger, B. & Tchernyshyov, O. Inertia and chiral edge modes of a skyrmion magnetic bubble. *Physical Review Letters* **109**, 217201 (2012).
- [143] Moutafis, C., Komineas, S. & Bland, J. Dynamics and switching processes for magnetic bubbles in nanoelements. *Physical Review B* **79**, 224429 (2009).
- [144] Büttner, F. *et al.* Dynamics and inertia of skyrmionic spin structures. *Nature Physics* **11**, 225–228 (2015).
- [145] Garst, M., Waizner, J. & Grundler, D. Collective spin excitations of helices and magnetic skyrmions : review and perspectives of magnonics in non-centrosymmetric magnets. *Journal of Physics D : Applied Physics* **50**, 293002 (2017).
- [146] Seki, S. *et al.* Propagation dynamics of spin excitations along skyrmion strings. *Nature communications* **11**, 1–7 (2020).
- [147] Xing, X., Zhou, Y. & Braun, H. Magnetic skyrmion tubes as nonplanar magnonic waveguides. *Physical Review Applied* **13**, 034051 (2020).
- [148] Lin, S.-Z., Zhu, J.-X. & Saxena, A. Kelvin modes of a skyrmion line in chiral magnets and the associated magnon transport. *Physical Review B* **99**, 140408 (2019).

-
- [149] Dhital, C. *et al.* Exploring the origins of the Dzyaloshinskii-Moriya interaction in MnSi. *Phys. Rev. B* **96**, 214425 (2017).
- [150] Usov, N. & Peschany, S. Magnetization curling in a fine cylindrical particle. *Journal of Magnetism and Magnetic Materials* **118**, L290–L294 (1993).
- [151] Feldtkeller, E. Mikromagnetisch stetige und unstetige magnetisierungskonfigurationen. *Zeitschrift für angewandte Physik* **19**, 530 (1965).
- [152] Döring, W. Point Singularities in Micromagnetism. *Journal of Applied Physics* **39**, 1006–1007 (1968).
- [153] Arrott, A., Heinrich, B. & Aharoni, A. Point singularities and magnetization reversal in ideally soft ferromagnetic cylinders. *IEEE Transactions on Magnetics* **15**, 1228–1235 (1979).
- [154] Hertel, R. Computational micromagnetism of magnetization processes in nickel nanowires. *Journal of Magnetism and Magnetic Materials* **249**, 251–256 (2002).
- [155] Nielsch, K. *et al.* Switching behavior of single nanowires inside dense nickel nanowire arrays. *IEEE Transactions on Magnetics* **38**, 2571–2573 (2002).
- [156] Da Col, S. *et al.* Observation of bloch-point domain walls in cylindrical magnetic nanowires. *Physical Review B* **89**, 180405 (2014).
- [157] Hubert, A. Mikromagnetisch singuläre punkte in bubbles. *Journal of Magnetism and Magnetic Materials* **2**, 25 (1975).
- [158] Galkina, E., Ivanov, B. & Stephanovich, V. Phenomenological theory of Bloch point relaxation. *Journal of Magnetism and Magnetic Materials* **118**, 373–378 (1993).
- [159] Malozemoff, A. & Slonczewski, J. *Magnetic domain walls in bubble materials : advances in materials and device research*, vol. 1 (Academic press, 2016).
- [160] Müller, G. P., Rybakov, F. N., Jónsson, H., Blügel, S. & Kiselev, N. S. Coupled quasimonopoles in chiral magnets. *Phys. Rev. B* **101**, 184405 (2020).
- [161] Milde, P. *et al.* Unwinding of a Skyrmion Lattice by Magnetic Monopoles. *Science* **340**, 1076–1080 (2013).

-
- [162] Ezawa, M. Compact merons and skyrmions in thin chiral magnetic films. *Phys. Rev. B* **83**, 100408 (2011).
- [163] Berkov, D. V., Ramstöck, K. & Hubert, A. Solving Micromagnetic Problems. Towards an Optimal Numerical Method. *Phys. Stat. Sol. (a)* **137**, 207–225 (1993).
- [164] Seberino, C. & Bertram, H. Concise, efficient three-dimensional fast multipole method for micromagnetics. *IEEE Trans. Magn.* **37**, 1078–1086 (2001).
- [165] Zienkiewicz, O. C. & Taylor, R. L. *Finite Element Method* (Butterworth-Heinemann, 2000).
- [166] Geuzaine, C. & Remacle, J.-F. Gmsh : A 3-D finite element mesh generator with built-in pre- and post-processing facilities : THE GMSH PAPER. *Int. J. Numer. Meth. Engng.* **79**, 1309–1331 (2009).
- [167] Delaunay, B. Sur la sphere vide. *Izv. Akad. Nauk SSSR, Otdelenie Matematicheskii i Estestvennyka Nauk* **7**, 793–800 (1934).
- [168] Chen, W., Fredkin, D. & Koehler, T. A new finite element method in micromagnetics. *IEEE Trans. Magn.* **29**, 2124–2128 (1993).
- [169] Rado, G. T. & Webrtman, J. R. Resonance in a ferromagnetic metal. *J. Phys. Chem. Sol.* **11(3-4)**, 315 (1959).
- [170] Hertel, R. Statische und dynamische magnetisierung in nanostrukturen. *Habilitationsschrift* (2005).
- [171] Rohart, S. & Thiaville, A. Skyrmion confinement in ultrathin film nanostructures in the presence of Dzyaloshinskii-Moriya interaction. *Physical Review B* **88** (2013).
- [172] Fredkin, D. & Koehler, T. Hybrid method for computing demagnetizing fields. *IEEE Trans. Magn.* **26**, 415–417 (1990).
- [173] Koehler, T. & Fredkin, D. Finite element methods for micromagnetics. *IEEE Trans. Magn.* **28**, 1239–1244 (1992).
- [174] Lindholm, D. Three-dimensional magnetostatic fields from point-matched integral equations with linearly varying scalar sources. *IEEE Trans. Magn.* **20**, 2025–2032 (1984).

-
- [175] Kakay, A., Westphal, E. & Hertel, R. Speedup of FEM Micromagnetic Simulations With Graphical Processing Units. *IEEE Transactions on Magnetics* **46**, 2303–2306 (2010). URL <http://ieeexplore.ieee.org/lpdocs/epic03/wrapper.htm?arnumber=5467640>.
- [176] Stroustrup, B. *The C++ Programming Language* (Addison-Wesley Professional, 2013), 4th edn.
- [177] Alexandrescu, A. *Modern C++ design : generic programming and design patterns applied* (Addison-Wesley Longman Publishing Co., Inc., USA, 2001).
- [178] Gamma, E., Helm, R., Johnson, R. & Vlissides, J. *Design patterns : elements of reusable object-oriented software* (Addison-Wesley Longman Publishing Co., Inc., USA, 1995).
- [179] Guennebaud, G., Jacob, B. *et al.* Eigen v3. <http://eigen.tuxfamily.org> (2010).
- [180] Schling, B. *The Boost C++ Libraries* (XML Press, 2011).
- [181] Chapman, B., Jost, G. & Pas, R. v. d. *Using OpenMP : Portable Shared Memory Parallel Programming (Scientific and Engineering Computation)* (The MIT Press, 2007).
- [182] Centre de Calcul de l'Université de Strasbourg (CCUS). URL <https://hpc.pages.unistra.fr/>.
- [183] Nickolls, J., Buck, I., Garland, M. & Skadron, K. Scalable Parallel Programming with CUDA : Is CUDA the parallel programming model that application developers have been waiting for? *Queue* **6**, 40–53 (2008). URL <https://doi.org/10.1145/1365490.1365500>.
- [184] Hwu, W.-m. W. *GPU Computing Gems Jade Edition* (Morgan Kaufmann Publishers Inc., San Francisco, CA, USA, 2011), 1st edn.
- [185] Schöberl, J. Netgen an advancing front 2d/3d-mesh generator based on abstract rules. *Computing and visualization in science* **1**, 41–52 (1997).
- [186] Ayachit, U. *The ParaView Guide : A Parallel Visualization Application* (Kitware, 2015). URL <https://www.paraview.org/>.

-
- [187] BÄ¶rm, S. *Efficient Numerical Methods for Non-local Operators* (2010). URL https://www.ems-ph.org/books/book.php?proj_nr=125.
- [188] Ahnert, K. & Mulansky, M. Odeint â€“ Solving Ordinary Differential Equations in C++. *AIP Conference Proceedings* **1389**, 1586–1589 (2011). URL <https://aip-scitation-org.scd-rproxy.u-strasbg.fr/doi/abs/10.1063/1.3637934>. Publisher : American Institute of Physics.
- [189] Hindmarsh, A. C. *et al.* SUNDIALS : Suite of nonlinear and differential/algebraic equation solvers. *ACM Transactions on Mathematical Software* **31**, 363–396 (2005). URL <https://doi.org/10.1145/1089014.1089020>.
- [190] Zheng, F. *et al.* Direct Imaging of a Zero-Field Target Skyrmion and Its Polarity Switch in a Chiral Magnetic Nanodisk. *Phys. Rev. Lett.* **119**, 197205 (2017).
- [191] Karakas, V. *et al.* Observation of Magnetic Radial Vortex Nucleation in a Multilayer Stack with Tunable Anisotropy. *Sci Rep* **8**, 7180 (2018).
- [192] Rave, W., Fabian, K. & Hubert, A. Magnetic states of small cubic particles with uniaxial anisotropy. *Journal of Magnetism and Magnetic Materials* **190**, 332–348 (1998).
- [193] Rave, W. & Hubert, A. Magnetic ground state of a thin-film element. *IEEE Trans. Magn.* **36**, 3886–3899 (2000).
- [194] Usov, N. A., Chang, C.-R. & Wei, Z.-H. Nonuniform magnetization structures in thin soft type ferromagnetic elements of elliptical shape. *Journal of Applied Physics* **89**, 7591–7593 (2001).
- [195] Hertel, R. & Kronmu, H. Finite element calculations on the single-domain limit of a ferromagnetic cubeFa solution to mMAG Standard Problem No. 3. *Journal of Magnetism and Magnetic Materials* **15** (2002).
- [196] Frenkel, J. & Doefman, J. Spontaneous and Induced Magnetisation in Ferromagnetic Bodies. *Nature* **126**, 274–275 (1930).
- [197] Kittel, C. Theory of the Structure of Ferromagnetic Domains in Films and Small Particles. *Phys. Rev.* **70**, 965–971 (1946).

-
- [198] Brown, W. F. The Fundamental Theorem of Fine-Ferromagnetic-Particle Theory. *Journal of Applied Physics* **39**, 993–994 (1968).
- [199] Yamasaki, A., Wulfhekel, W., Hertel, R., Suga, S. & Kirschner, J. Direct Observation of the Single-Domain Limit of Fe Nanomagnets by Spin-Polarized Scanning Tunneling Spectroscopy. *Physical Review Letters* **91** (2003).
- [200] Zhao, X. *et al.* Direct imaging of magnetic field-driven transitions of skyrmion cluster states in FeGe nanodisks. *Proceedings of the National Academy of Sciences* **113**, 4918–4923 (2016).
- [201] Kittel, C. Physical Theory of Ferromagnetic Domains. *Rev. Mod. Phys.* **21**, 541–583 (1949).
- [202] Lebech, B., Bernhard, J. & Freltoft, T. Magnetic structures of cubic FeGe studied by small-angle neutron scattering. *Journal of Physics : Condensed Matter* **1**, 6105–6122 (1989).
- [203] Pylypovskiy, O. V., Sheka, D. D. & Gaididei, Y. Bloch point structure in a magnetic nanosphere. *Phys. Rev. B* **85**, 224401 (2012).
- [204] Takagi, R. *et al.* Particle-size dependent structural transformation of skyrmion lattice. *Nature Communications* **11**, 1–7 (2020).
- [205] Shibata, K. *et al.* Temperature and magnetic field dependence of the internal and lattice structures of skyrmions by off-axis electron holography. *Physical Review Letters* **118**, 087202 (2017).
- [206] McGrouther, D. *et al.* Internal structure of hexagonal skyrmion lattices in cubic helimagnets. *New Journal of Physics* **18**, 095004 (2016).
- [207] Kang, W. *et al.* Magnetic Skyrmions for Future Potential Memory and Logic Applications : Alternative Information Carriers 6 (2018).
- [208] Zhang, S. Current-induced magnetic skyrmions oscillator. *New J. Phys.* 14 (2015).
- [209] Garcia-Sanchez, F. A skyrmion-based spin-torque nano-oscillator. *New J. Phys.* 11 (2016).

-
- [210] Song, K. M. *et al.* Skyrmion-based artificial synapses for neuromorphic computing. *Nat Electron* **3**, 148–155 (2020).
- [211] Rößler, U. K., Bogdanov, A. N. & Pfeleiderer, C. Spontaneous skyrmion ground states in magnetic metals. *Nature* **442**, 797–801 (2006).
- [212] Lin, S.-Z., Reichhardt, C., Batista, C. D. & Saxena, A. Particle model for skyrmions in metallic chiral magnets : Dynamics, pinning, and creep. *Physical Review B* **87**, 214419 (2013).
- [213] Brearton, R., van der Laan, G. & Hesjedal, T. Magnetic skyrmion interactions in the micromagnetic framework. *Physical Review B* **101**, 134422 (2020).
- [214] Zhang, S., van der Laan, G., Wang, W., Haghighirad, A. & Hesjedal, T. Direct Observation of Twisted Surface skyrmions in Bulk Crystals. *Phys. Rev. Lett.* **120**, 227202 (2018).
- [215] Purnama, I., Gan, W. L., Wong, D. W. & Lew, W. S. Guided current-induced skyrmion motion in 1D potential well. *Sci Rep* **5**, 10620 (2015).
- [216] Thiaville, A., Nakatani, Y., Miltat, J. & Suzuki, Y. Micromagnetic understanding of current-driven domain wall motion in patterned nanowires. *Europhys. Lett.* **69**, 990–996 (2005).
- [217] Buess, M. *et al.* Fourier transform imaging of spin vortex eigenmodes. *Physical Review Letters* **93**, 077207 (2004).
- [218] Prychynenko, D. *et al.* Magnetic skyrmion as a nonlinear resistive element : a potential building block for reservoir computing. *Physical Review Applied* **9**, 014034 (2018).

Swapneel Amit PATHAK

Simulation of Three-Dimensional Skyrmions in Confined Geometries

Résumé

Dans les matériaux magnétiques non centrosymétriques, l'interaction Dzyaloshinskii-Moriya favorise les structures d'aimantation chirales telles que les états hélicoïdaux et les skyrmions. Cette thèse étudie l'effet du confinement géométrique tridimensionnel (3D) sur de telles structures en utilisant des simulations micromagnétiques par éléments finis. Une étude exhaustive examine les états d'aimantation se formant dans les nanosphères de FeGe en fonction de leur taille et du champ appliqué. On trouve une grande multiplicité d'états d'aimantation, ce qui pourrait être utile pour les dispositifs de mémoire multi-états. Il est ensuite démontré que des poches circulaires dans des couches étendues peuvent, grâce à l'effet du confinement 3D, agir comme sites de piégeage pour les skyrmions. Enfin, il est montré que des effets de confinement peuvent guider des skyrmions déplacés électriquement dans des dispositifs de type registre à décalage, évitant ainsi des déflexions indésirables.

Résumé en anglais

In non-centrosymmetric magnetic material, the Dzyaloshinskii-Moriya Interaction favors the formation of chiral magnetization structures such as helical states and skyrmions. In this thesis, the effect of three-dimensional (3D) geometric confinement on such chiral structures is investigated with finite-element micromagnetic simulations. As a first example, an exhaustive study discusses the magnetization states forming in FeGe nanospheres as a function of the particle size and the applied field. A surprisingly large multiplicity of possible magnetization states is found, which could be a useful feature for multi-state memory devices. The effect of 3D confinement is then studied in a different context, demonstrating that circular pockets in extended films can act as pinning sites for skyrmions. Finally, it is shown that geometric confinement effects can also be used to guide electrically driven skyrmions in shift-register type devices, thereby preventing unwanted lateral deflections.